University of California
Santa Barbara

Quantum Dot Lasers as Comb Sources

A dissertation submitted in partial satisfaction
of the requirements for the degree

Doctor of Philosophy
in
Electrical and Computer Engineering

by

Mario James Dumont

Committee in charge:

Professor John Bowers, Chair
Professor Chris Palmstrøm
Professor Jonathan Klamkin
Professor Frédéric Grillot, Télécom Paris

July 2024

The Dissertation of Mario James Dumont is approved.

Professor Chris Palmstrøm

Professor Jonathan Klamkin

Professor Frédéric Grillot, Télécom Paris

Professor John Bowers, Committee Chair

July 2024

Quantum Dot Lasers as Comb Sources

Copyright © 2024

by

Mario James Dumont

This dissertation is dedicated to Steffi Dumont, Andy Netherton, and Paolo Pintus. Without their help I could not have accomplished my Ph.D.

Acknowledgements

I am grateful and honored to have received my Ph.D. from the department of Electrical and Computer Engineering at the University of California, Santa Barbara. There were many fortunate opportunities that have allowed me to achieve my doctorate throughout the six years as a Ph.D. student and the two years as a Masters student. It has been a long and difficult journey, and countless people along the way have helped me to complete my degree, and it is not possible to mention all of them here.

Firstly I would like to thank my advisor, Professor John Bowers, for his support and guidance throughout the entire process. Without him allowing me to join his research group in 2016, non of this would have been possible. While in his group I had many great opportunities to learn about all the aspects of GaAs based quantum dot lasers. I was very fortunate to learn how to grow III-V materials by MBE. I was also exposed to microfabrication in the amazing Nanofab cleanroom at UCSB. Lastly, I was able to gain valuable testing experience in a laboratory with almost every piece of lab equipment that I could ever need. I was additionally part of laser packaging effort, which helped me understand the entire laser production process. While learning these skills, I was able to be part of many great projects that spanned different topics and had great opportunities. It was a great honor to work under Professor Bowers and contribute to his research efforts.

I would like to thank all the members of the quantum dot effort that I had the pleasure of working with in Professor Bowers' group, some of which are listed here: Deahwan, Justin, Yating, Chen, Kaiyin, Rosalyn, Robert, Eamonn, Jenny, Songtao, and Alan. They all helped my studies in different ways throughout my time at UCSB. Deahwan, Justin, and Chen taught me how to grow, for which I was very grateful for the opportunity. Yating and Kaiyin were kind enough to teach me laser fabrication, and Justin and Kaiyin helped me understand how we could improve the design of the

lasers. Robert helped with teaching me how to start testing quantum dot lasers along with Songtao and they helped grow my understanding of them. Songtao was the first member of the group to make quantum dot mode locked lasers, which my entire thesis is on. He pioneered the work on harmonic mode locked lasers in Professor Bowers' group, and helped start the work on the PIPES project. Eamonn and Jenny were both valuable members of the team, using the most advanced materials characterization techniques such as TEM to investigate our material and how aging affected its structure. Lastly, I would like to thank Alan for beginning the research efforts on quantum dot lasers after a 15 year break. I am grateful to have been part of such a productive and successful research team.

I must thank all the members of the PIPES research project, which motivated the research in this dissertation. There was a large and qualified team at Analog Photonics that made the PIC that was used in PIPES, which was a huge undertaking that took many hours to complete. Without their efforts, the mode locked lasers in this project would never have been designed. I am equally grateful for the UCSB team members. Theogarajan's group designed the electical IC that was made to test the PIC in the project, and led the electronics-photonics co-integration effort. Although the ultimate integration effort was not successful, I am thankful for their efforts in the team. Lastly I would like to thank the UCSB team members that tested the demonstrators in phase one and also phase two, particularly Andy and Mark. We spent countless nights in the lab, essentially seven days a week, during the last several months of phase one. The team camaraderie was all that got me through some nights. We worked together, through the pandemic, in the lab testing until we were completely exhausted.

I would like to thank Andy Netherton specifically. We both struggled at times to find the energy to continue working on PIPES and pushing other teammates to complete their tasks to try to have the entire system work in harmony. It was an extremely challenging

project, with metrics that seemed unattainable at times, but we never gave up and gave every once of energy to complete that project. It was great to become friends with Andy over the years, having met in our first semester at UCSB and working together until our last days in the research group. I am very happy that we were able to go backpacking together in Sierras; that was an amazing trip, with memories to fill a lifetime.

Without Paolo Pintus' help and guidance, I don't know if I would have finish my doctorate. Paolo was extremely helpful and motivating throughout my time here. There were countless times where he helped me see the novelty and value of my research. He always was able to see the positive aspects in the work I was doing, and focus my efforts on the important aspects. It was very helpful, for me as a researcher, to have the huge amount of guidance from Paolo with my research. He was always willing to listen and offer advice. Thank you for all the walks to get an afternoon espresso and talk things over.

I cannot finish the acknowledgments without thanking my family and my wife, Steffi. She spent eight years with me as I completed my masters and doctorate. Completing a Ph.D. is extremely stressful on a partner, and I am so grateful that she was always there to support me and show kindness and patience. There were countless nights in the lab that lasted later than planned and canceled weekend activities during my time as a grad student, and I want to thank her for the understanding and kindness she offered in return. Additionally, she gave me a lot of practical help and advice throughout my time as a grad student that I am very grateful for. Additionally, I would like to thank my parents for supporting me and my aspirations throughout my life and supporting me through my undergraduate degree. They did many things to foster my love of science, and without that I never would have pursued my career as a scientist and engineer.

Curriculum Vitæ

Mario James Dumont

Education

2024	Ph.D. in Electrical and Computer Engineering, University of California, Santa Barbara.
2018	M.S. in Electrical and Computer Engineering, University of California, Santa Barbara.
2014	B.S. in Physics, Mathematics, and German, University of Colorado, Boulder.

Journal Publications

1. Dumont, M., Liu, S., Kennedy, M. J., & Bowers, J. (2022). High-efficiency quantum dot lasers as comb sources for DWDM applications. *Applied Sciences*, 12(4), 1836.
2. Dong, B., Dumont, M.*, Terra, O., Wang, H., Netherton, A., & Bowers, J. E. (2023). Broadband quantum-dot frequency-modulated comb laser. *Light: Science & Applications*, 12(1), 182. *equally contributing
3. Razumov, A., Heebøll, H. R., Dummont, M., Terra, O., Dong, B., Riebesehl, J., ... & Zibar, D. (2023). Subspace tracking for phase noise source separation in frequency combs. *Optics Express*, 31(21), 34325-34347.
4. Shang, C., Hughes, E., Wan, Y., Dumont, M., Koscica, R., Selvidge, J., ... & Bowers, J. E. (2021). High-temperature reliable quantum-dot lasers on Si with misfit and threading dislocation filters. *Optica*, 8(5), 749-754.
5. Hughes, E. T., Dumont, M., Hu, Y., Liang, D., Beausoleil, R. G., Bowers, J. E., & Mukherjee, K. (2022). Dislocation Formation and Filtering in III–V Regrowth on GaAs Bonded on Si. *Crystal Growth & Design*, 22(10), 5852-5860.
6. Liu, S., Norman, J., Dumont, M., Jung, D., Torres, A., Gossard, A. C., ... & Jung, D. (2019). High-performance O-band quantum-dot semiconductor optical amplifiers directly grown on a CMOS compatible silicon substrate. *ACS Photonics*, 6(10), 2523-2529.
7. Dong, B., de Labriolle, X. C., Liu, S., Dumont, M., Huang, H., Duan, J., ... & Grillot, F. (2020). 1.3-μm passively mode-locked quantum dot lasers epitaxially grown on silicon: gain properties and optical feedback stabilization. *Journal of Physics: Photonics*, 2(4), 045006.
8. Wan, Y., Norman, J. C., Tong, Y., Kennedy, M. J., He, W., Selvidge, J., ... & Bowers, J. E. (2020). 1.3 μm quantum dot-distributed feedback lasers directly grown on (001) Si. *Laser & Photonics Reviews*, 14(7), 2000037.

9. Wan, Y., Jung, D., Shang, C., Collins, N., MacFarlane, I., Norman, J., ... & Bowers, J. E. (2018). Low-threshold continuous-wave operation of electrically pumped 1.55 μm InAs quantum dash microring lasers. *ACS Photonics*, 6(2), 279-285.
10. Norman, J. C., Zhang, Z., Jung, D., Shang, C., Kennedy, M. J., Dumont, M., ... & Bowers, J. E. (2019). The importance of p-doping for quantum dot laser on silicon performance. *IEEE Journal of Quantum Electronics*, 55(6), 1-11.
11. Selvidge, J., Hughes, E. T., Norman, J. C., Shang, C., Kennedy, M. J., Dumont, M., ... & Mukherjee, K. (2021). Reduced dislocation growth leads to long lifetime InAs quantum dot lasers on silicon at high temperatures. *Applied Physics Letters*, 118(19).
12. Wan, Y., Shang, C., Norman, J., Shi, B., Li, Q., Collins, N., ... & Bowers, J. E. (2020). Low threshold quantum dot lasers directly grown on unpatterned quasi-nominal (001) Si. *IEEE Journal of Selected Topics in Quantum Electronics*, 26(2), 1-9.

Conference Publications

1. Netherton, A., Dumont, M., Nelson, Z., Jhonsa, J., Mo, A., Koo, J., ... & Bowers, J. (2024, February). 25.1 Short-Reach Silicon Photonic Interconnects with Quantum Dot Mode Locked Laser Comb Sources. In *2024 IEEE International Solid-State Circuits Conference (ISSCC)* (Vol. 67, pp. 422-424). IEEE.
2. Bernal, S., Dumont, M., Berikaa, E., St-Arnault, C., Hu, Y., Castrejon, R. G., ... & Plant, D. V. (2024, March). 8.5 Tbps Net SiP O-band Coherent Transmission over 10 km Using a Quantum-Dot Mode-Locked Comb Laser. In *2024 Optical Fiber Communications Conference and Exhibition (OFC)* (pp. 1-3). IEEE.
3. Liu, S., Wu, X., Norman, J., Jung, D., Dumont, M., Shang, C., ... & Bowers, J. (2020, March). High-performance mode-locked lasers on silicon. In *Physics and Simulation of Optoelectronic Devices XXVIII* (Vol. 11274, pp. 195-202). SPIE.
4. Liu, S., Norman, J., Dumont, M., Pintus, P., Tran, M., Jung, D., ... & Bowers, J. (2019, September). O-Band Quantum Dot Semiconductor Optical Amplifier Directly Grown on CMOS Compatible Si Substrate. In *2019 IEEE Photonics Conference (IPC)* (pp. 1-2). IEEE.
5. Shang, C., Hughes, E., Wan, Y., Dumont, M., Koscica, R., Selvidge, J., ... & Bowers, J. E. (2021, May). High temperature reliable epitaxially grown quantum dot lasers on (001) Si with record performance. In *2021 Conference on Lasers and Electro-Optics (CLEO)* (pp. 1-2). IEEE.
6. Norman, J. C., Liu, S., Wan, Y., Zhang, Z., Shang, C., Selvidge, J. G., ... & Bowers, J. E. (2020, February). Epitaxial integration of high-performance quantum-dot lasers on silicon. In *Silicon Photonics XV* (Vol. 11285, pp. 20-27). SPIE.

7. Liu, S., Tong, Y., Norman, J., Dumont, M., Gossard, A., Tsang, H. K., & Bowers, J. (2020, March). High efficiency, high gain and high saturation output power quantum dot SOAs grown on Si and applications. In *Optical Fiber Communication Conference* (pp. T4H-3). Optica Publishing Group.

8. Estrella, S., Renner, D., Hirokawa, T., Maharry, A., Dumont, M., Schow, C., & Freedom Photonics LLC Santa Barbara United States. (2019). High-Speed Optical Interconnect for Cryogenically Cooled Focal Plane Arrays. in *GOMACTech*, 18(2).

Abstract

Quantum Dot Lasers as Comb Sources

by

Mario James Dumont

Abstract text.

Contents

Acronyms

2-D two-dimensional

20-λ twenty-wavelength

3-D three-dimensional

AC autocorrelator

AFM atomic force microscope

AlGaAs Aluminum Gallium Arsenide

AM amplitude-modulated

ASE amplified spontaneous emission

BER bit error ratio

CPM colliding pulse mode locking

CPMLL colliding pulse mode locked laser

CW continuous-wave

DBR distributed Bragg reflector

DeMux demultiplexer

DFB distributed feedback

DWDM Dense Wavelength Division Multiplexing

DWELL dots in a well

ECL external cavity laser

ES excited state

ESA electrical spectrum analyzer

FEC forward error correction

FFT fast fourier transform

FM frequency-modulated

FP Fabry-Perot

FSR free-spectral-range

FWHM full width at half maximum

FWM Four Wave Mixing

GaAs Gallium Arsenide

GS ground state

GVD group velocity dispersion

HPD holes per QD

I/O input/output

IC integrated circuit

InAs Indium Arsenide

InGaAs Indium Gallium Arsenide

InP Indium Phosphide

LEF linewidth enhancement factor

LI light-current

LiNb lithium niobate

LIV light-current-voltage

LO local oscillator

MBE molecular beam epitaxy

MLL mode locked laser

MRM micro-ring modulator

Mux multiplexer

MZI Mach-Zehnder Interferometer

NOFC nonlinear optical frequency comb

OFC Optical Frequency Comb

OSA optical spectrum analyzer

PAM partial amplitude modulation

PD photodetector

PDFA praseodymium-doped fiber amplifier

PIC photonic integrated circuit

PL photoluminescence

PM polarization-maintaining

pMD p-modulation doped

PoLL power of the lowest line

QCL quantum cascade laser

QD quantum dot

QD-MLL quantum dot mode locked laser

QDash quantum dash

QW quantum well

RBW resolution bandwidth

RF radio frequency

RHEED Reflection High Energy Electron Diffraction

RTA rapid thermal annealed

SA saturable absorber

SEM Scanning Electron Microscope

SERDES serializer/deserializer

SESAM semiconductor saturable absorber mirror

SK Stranski–Krastanow

SMSR side mode suppression ratio

SMU source meter unit

SNR signal to noise ratio

SOA semiconductor optical amplifier

SpaHB spatial hole burning

SSMF standard single mode fiber

TBF tunable bandpass filter

TLS tunable laser source

UID unintentionally doped

VBW video bandwidth

WDM Wavelength Division Multiplexing

WPE wall plug efficiency

WPE/C wall plug efficiency per channel

WPE20 wall plug efficiency of the 20^{th} line

Chapter 1

Next Generation Light Sources in Data Center Interconnects

1.1 Introduction

With the explosion in demand for artificial intelligence and machine learning, Internet Protocol traffic, particularly intra-datacenter traffic, has thrust hyperscale datacenters into the "Zeta-byte era" [1]. Current trends in artificial intelligence are demanding increased model size, which is seriously constraining current datacenter architectures. Particularly, the complexity of chips has continued to exponentially increase, requiring the net input/output (I/O) data rate to also exponentially grow. In order to address this issue for high performance chips, power-hungry and large serializer/deserializer (SERDES) blocks have filled the gap[2]. This, however, has led to a 25× increase in the power allocated to SERDES[3], which cannot be sustained forever.

Currently, it is still more power efficient to transmit data on and off the chip with copper wirelines. However, as individual lane rates increase, the loss through copper wirelines continues to increase, which requires higher order modulation formats, such as

partial amplitude modulation (PAM), at the cost of higher signal to noise ratio (SNR) needs. In contrast, optical fiber loss is measured in dB/km, offering the possibility of inter-datacenter links without the need for optical amplification. Thus, the energy cost of scaling the data rate of optical links can outscale electrical links[2], but the initial creation of the optical data-signal currently costs too much energy per bit (J/bit) for it to out compete electrical links over short distances.

To reduce power spent on input-output (IO), increase chip lane rates, and eliminate the IO bottleneck at the front panel of server rack units [4], datacenter links will see the photonics move into the electronics package in the near future [2, 5]. This seriously constrains the power consumption, footprint and spectral efficiency of next generation links. Significant breakthroughs in silicon photonics have led to compact, power efficient transceivers, which benefit from the high volume production capability of silicon [6].

One technology in particular, micro-ring modulators (MRMs) has allowed silicon photonic transceivers to produce optical links with extremely high IO bandwidth per mm^2 [7]. MRMs benefit from a compact footprint and are resonant structures, allowing them to modulate a single wavelength in a Dense Wavelength Division Multiplexing (DWDM) signal, potentially eliminating optical multiplexers (MuxMuxes)[8]. This capability has dramatically increased the need for a monolithic light source that can deliver all DWDM channels. The three approaches typically considered to meet this need are distributed feedback (DFB) arrays, nonlinear optical frequency combs (NOFCs), and semiconductor mode locked lasers (MLLs) [9].

1.1.1 DFB Arrays

The archetype Wavelength Division Multiplexing (WDM) light source, DFB arrays are implemented in long-haul, metro, and datacenter applications [10]. DFBs are com-

mercially available across the entire telecom range, with wavelengths available anywhere between 760-14000 nm [11]. The WDM source is formed by combining the optical output of many individual lasers. DFB arrays have two aspects that NOFCs and MLLs do not; namely the ability to scale the power in each channel independently to the desired level and no reduction in efficiency as the number of channels increases. They do, however, have the largest footprint, and require a Mux to combine individual channels into one fiber. Additionally, the large temperature variation inside data center racks requires control electronics to keep each individual laser aligned to the DWDM grid / MUX, increasing their energy cost per bit [12].

1.1.2 Nonlinear Optical Frequency Combs

As an alternative to DFB arrays, NOFC offer the ability to generate a spectrum of discrete optical frequencies separated by a fixed channel spacing. NOFCs typically employ micro-disk or micro-ring resonators, but a straight waveguide can be used in combination with a MLL [9]. They can offer extremely large bandwidth [13], the channel spacing can be adjusted over an extremely large range [14, 15], and individual comb lines can offer superior optical linewidths making them suitable for coherent communication [16]. Anomalous Group-Velocity-Dispersion (GVD) Kerr solitons suffer from an inherently low efficiency [17]. Recently, normal GVD dark soliton combs have reached 41% on-chip pump-to-comb efficiency [18]. Their biggest drawback is the large power variation of channels across the comb (10-20 dB). They also suffer from an inherently low efficiency when considering net wall plug efficiency (WPE) of the entire source. Often neglected from the calculation, the WPE of the pump laser itself must be considered. Additionally, optical coupling losses between the laser and the NOFC further decrease the efficiency, however integration will alleviate this [19]. Excluding pump generation

and coupling, conversion efficiencies can be as high as 40-60% [18, 20].

1.1.3 Semiconductor MLLs

Semiconductor MLLs output a high frequency pulsetrain with a fixed frequency spacing between the longitudinal cavity modes in a compact, efficient, reliable, and robust device, making them a natural candidate for optical sampling [21], clock distribution [22], and as DWDM sources [23]. Additionally, these devices do not require initiation routines or feedback loops and only use voltage and current sources. quantum well (QW) MLLs have been investigated for more than three decades, however the introduction of Indium Arsenide (InAs)/Gallium Arsenide (GaAs) quantum dot (QD) active region has improved their performance. QDs have been shown to have lower threshold [24], smaller linewidth enhancement factor [25], benefit from inhomogeneous broadening [26], improved temperature-induced threshold increase (T_0) [27], and improved carrier dynamics [28]. Implementing InAs QDs has led to the development of high output power, efficient MLLs suitable as comb sources [29, 9].

Using the benefits of InAs/GaAs, quantum dot mode locked lasers (QD-MLLs) are capable of generating the flattest combs of any multi-wavelength light source, producing combs with tens of comb lines and a fixed channel spacing. This makes them ideal candidates for meeting the needs of next generation terabit-scale WDM systems for short reach applications, which demand low-cost, extremely low power consumption, and miniaturized size. This has attracted attention in using them in DWDM transmission systems for nearly two decades[30, 31], with the two main architectures originally shown in [31] and reproduced in Figure 1.1. The system on the left is a standard archetype DWDM system implementation using a single light source. The light must be spectrally separated with a demultiplexer (DeMux) into the individual modes or channels for each modulator, which

future due to silicon's indirect bandgap.

Multi-wavelength laser sources and modulator/driver arrays present the principal impediments to downscaling and commodifying WDM. Today's WDM optical sources based on DFB arrays on InP [6], or perhaps bonded to silicon in the future [7], have several drawbacks. These include the packaging complexity of multiple lasers, modulators, and drivers, as well as need for temperature control and multiple wavelength tracking that may become untenable in large-scale deployments. We believe that a better alternative, particularly for what will become commodity signaling systems, is a single diode comb laser based on InAs/GaAs quantum dots (QDs) [8, 9] that can provide multiple narrow-spectrum peaks, each corresponding to a longitudinal mode of the single laser cavity. This single laser is a viable WDM source because it overcomes many drawbacks of discrete laser array sources in conventional systems, although temperature adaptability remains challenging. Two potential comb laser-driven transceiver approaches are illustrated in Figure 2.

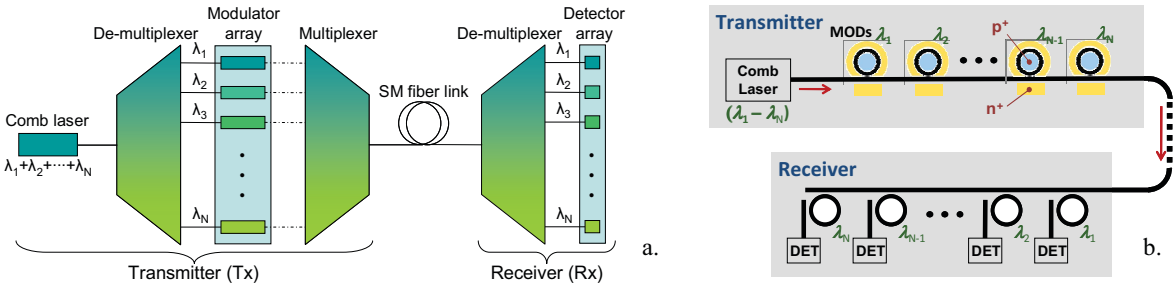

Figure 2. Comb laser-based WDM transceiver options: a. conventional design based on comb channel de-multiplexing, detection, and multiplexing in the Tx, Rx. b. unconventional design based on in-line ring resonators for combined channel selection and modulation in the Tx [10] and channel selection and detection in the Rx. Note that the microring-based transceiver has very challenging silicon photonics processing requirements.

Figure 1.1: The two commonly implemented QD comb data transmission schemes: (a) shows a conventional single light source system where the light is separated, modulated, and combined with DeMux, modulator, and Mux and the receiver uses a DeMux and detectors. (b) shows a compact system designed around silicon-based PIC, where wavelength-specific MRM allow in-line operation with no Mux/DeMux required. figure reproduced from [31].

is typically a Mach-Zehnder Interferometer (MZI). The modulated channels each receive data, and are combined with a Mux before being transmitted down the same fiber. At the receiver, another DeMux is used to separate each channel into it's respective detector. The system on the right uses the unique properties of MRM, to selectively modulate an individual channel of a DWDM signal without the need for a DeMux/Mux. These two layouts are discussed in greater detail in the rest of this chapter.

1.2 DWDM System Architecture

The following system drawn in Figure 1.2 is designed to leverage the advantages of using a QD-MLL for DWDM data transmission. This link architecture along with experimental results are discussed in [32], and is similar in design to 1.1 b. The system utilizes one QD-MLL as a multi-wavelength source that produces twenty-wavelength (20-λ) comb with 60 Ghz spacing. The laser drives two independent transmitters, each capable of transmitting 1 Tb/s; the output from each facet of the laser is fiber coupled with polarization-maintaining (PM) fiber to the inputs of photonics PIC. The channels of the 20-λ comb are first split with a 1×2 power splitter for polarization division multi-

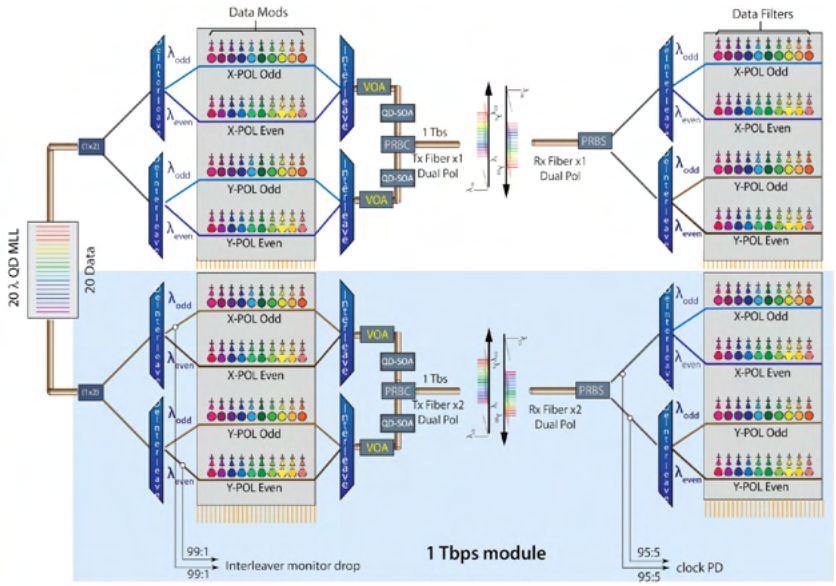

Figure 1.2: Schematic of the MRM-based DWDM-transmission system. A single QD-MLL produces 20 wavelength channels to drive 20 MRMs for each polarization. This system is designed to transmit 1 Tb/s with minimal size and power consumption. Reproduced from [32]

plexing; for each of wavelength there are two MRMs, one for each polarization. Following this, the channels are separated with an interleaver into even and odd channels to increase the comb spacing present at the MRM banks to 120 GHz. This is done to reduce the crosstalk between channels caused by parasitic modulation of adjacent channels by MRMs[33].

The data is encoded on each channel with 26.4 Gb/s NRZ signal with 5.6% forward error correction (FEC) overhead, netting a 25 Gb/s data rate. An in-depth discussion of the need for FEC in compact, energy efficient links along with the accrued latency is discussed in [32]. The net data rate per channel gives 500 GB/s for one comb. The output from the PIC is then amplified by a QD semiconductor optical amplifier (SOA), before passing through a polarizing rotating beam combiner to launch both outputs of the PIC onto one PM fiber on orthogonal polarizations, which increases the data per fiber to 1 Tb/s. The received data is first polarization demultiplexed with a polarizating

rotating beam splitter before passing though an interleaver to separate the channels into even and odd. The received signals are then wavelength demultiplexed with ring filters. The drop port of the ring filter is connected to a high speed photodetector (PD), which recovers the original data signal. Clock forwarding is accomplished by using a variable optical attenuator modulator with a 209 MHz signal, which is 128 times slower than the data rate. This clock fowarding scheme is implemented to reduce energy consumption by removing the need for clock recovery digital signal processing[34].

This system places several constraints on the MLL. The most important restriction is the wavelength stability of the individual comb lines, because MRMs have frequency dependent loss and extinction ratio. MLL-based combs have a very stable comb spacing, however the absolute frequency does drift[35] These lasers were shown to be stable enough for data transmission[36, 32]. Additionally, the power of each comb line must fall in a narrow window. The power of the highest line must not exceed the nonlinear thermal threshold of the MRM. Simultaneously, the power of the lowest line (PoLL) in the 20-λ must have a large enough power to have the required received power at the receiver PD to have the required SNR to meet the bit error ratio (BER) required for the FEC architecture chosen. Most importantly, the laser much produce the comb with the power allocated in the budget. Temperature performance is also considered, because the system was designed to work from 20 to 80°C and the laser was designed to operate at the average temperature, 50°C. These metrics will be discussed in detail in later chapters.

In addition, the QD-MLLs were also used in a coherent experiment involving two MLLs, one as the transmitter, and the other as an optical local oscillator (LO). The experimental setup is shown in Figure 1.3, and the full details can be found in in [36]. This setup is similar to 1.1 a, however it uses a tunable bandpass filter (TBF) to separate comb lines for data transmission, instead of a DeMux, which is commonly done in demonstrations. Because the data is coherently encoded, an additional laser at the

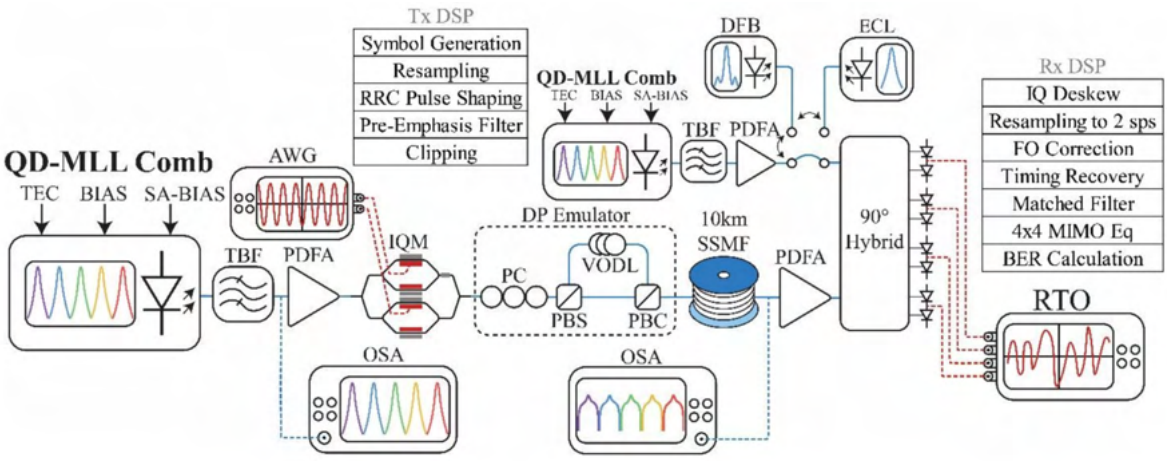

Figure 1.3: experimental setup for a comb to comb transmission expirement. Figure taken from [36]

receiver is used as a LO in coherent detection. In DWDM demonstration experiments, a commercial external cavity laser (ECL) or DFB is commonly used, which could have better phase noise performance than the transmitter light source. However, this experiment uses a QD-MLL at the receiver, identical to a real world deployment of the system. The two QD-MLLs are as identical as possible; the devices come from the same laser bar and have the same saturable absorber length. This gives very similar performance between the devices, particularly that they have identical repetition rates, and very similar comb bandwidth and power per line. This coherent data transmission experiment uses a IQ MZI, because MRM are only capable of intensity modulation. Multiple praseodymium-doped fiber amplifiers (PDFAs) were used to overcome the losses from the MZI and TBFs.

1.3 DWDM Data transmission with QD-MLLs

The QD-MLL-powered DWDM system was envisioned by Innolume GMBH and the first demonstrations were performed using QD-Fabry-Perot (FP) lasers with either 40 or

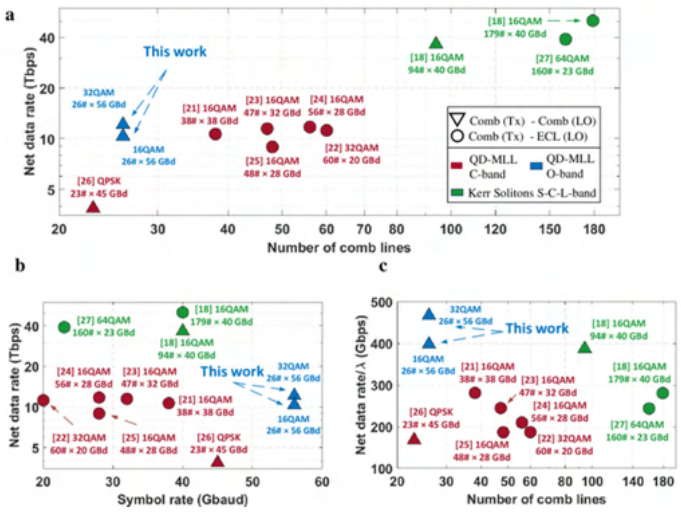

Figure 1.4: Comparison of the state-of-the-art data transmission experiments done using a single source. (a) compares the net data rate vs. the number of channels encoded. (b) compares the net data rate vs. symbol rate, and (c) compares the net data rate for one channel vs. the number of channels used. Figure taken from [36]

80 GHz channel spacing[30, 31]. An individual comb line was filtered out using a TBF, amplified with a QD-SOA, and modulated with a lithium niobate (LiNb) MZI. In [30], they modulated ten comb lines with with 10 Gb/s, and achieved error free transmission (BER$< 10^{-13}$) for all lines, while in [31] they modulated an unspecified number of lines that were within 3 dB of the highest powered mode and achieved error free transmission. The demonstrations that followed switched to MLLs because of the previously mentioned benefits, such as flatter spectra and equal channel spacing. Although self-mode locking was observed in both InAs/GaAs and InAs/Indium Phosphide (InP) MLLs[37, 38], most DWDM data transmission experiments were conducted on InAs/InP self-mode-locked MLLs due to larger interest in C-band operation.

Figure 1.4 shows a summary of the highest data rate transmission experiments with different sources. (a) compares the number of channels vs. aggregate data rate. All other MLL demonstrations on Figure 1.4 are C-band with InAs/InP based lasers, which have channel spacing of 42[39], 25[40], 34[41], 28[42], and 28[43] for the 10, 12, 12.03, 12.5, and

12.54 Tb/s respectively. These demonstrations are labeled 21-25 in 1.4. Not included in the figure is a previous demonstration from UCSB, where a comb with 20 GHz spacing was used to transmit 4.1 Tb/s[23] by using 65 comb lines. The data labeled "this work" refers to an experiment conducted in [36], outlined in Figure 1.4, which uses a QD-MLL with 58 GHz comb spacing.

The work presented in [36] produced the highest data transmission rate for a single device in the O-Band, and the highest data rate for a comb-2-comb data transmission experiment using MLLs. This was achieved by using the high channel spacing, which is $1.5 - 2\times$ larger channel spacing of the other MLL demonstrations, which allowed data transmission with higher symbol rate of 56 GBaud. Additionally, the excellent noise performance of the lasers allowed more complex modulation formats up 32QAM. An aggregate data rate of 12.1 Tb/s was achieved with 26 comb lines, about $\frac{1}{2}$ the number of lines of the other MLL demonstrations. This gives the highest net data rate per channel out of any demonstration.

1.4 Dissertation Outline

The body of this dissertation discusses all aspects of the production, characterization, physics of operation, and optimization of QD-MLLs for generation of combs. The next chapter is dedicated to an overview of all aspects of QD-MLLs and Optical Frequency Comb (OFC) in general. The growth of material, fabrication processes, and operational principles are detailed. Following this, the analytical tools used to characterize lasers are built up. The tools and methods used in collecting and analyzing data are explained. The types of combs generated by QD-MLLs are discussed, and distinguished from the mode-locking typically observed. In the last chapter, a systematic study of the doping in the active region is explained, which shows the optimum p-doping.

Chapter 2

Introduction to Quantum Dot Mode Locked Lasers

In this chapter, all the individual aspects that constitute QD-MLLs are discussed. To understand their operation, both the production steps and the fundamental operating principles will be discussed.

The growth of QDs by molecular beam epitaxy (MBE) will first be discussed. Unlike a QW gain region, which can be grown with relatively large changes in growth conditions, particularly temperature, QD growth requires exact and repeatable conditions. Following this the fabrication of MLLs will be discussed. The process is similar to FP laser fabrication, and different waveguide structures are discussed.

The second portion covers theoretical aspects of understanding comb operation and types of combs generated in semiconductor MLLs. Active versus passive mode locking is discussed, along with the different types of phase locking states that can be present inside a passive MLL. Lastly, harmonic mode locking is detailed, which is necessary to generate high channel spacing and temperature resilient lasers.

2.1 Growth of Quantum Dots by MBE

Quantum dots are extremely small particles, with sizes comparable to the de-Broglie wavelength of electrons in the material that they are made up of. This causes quantum confinement of electrons, and also holes in semiconductor materials, which gives them optical and electrical properties not exhibited by the bulk material. The carrier confinement causes discrete energy levels, similar to solving Schödinger's equation for a particle in a box with finite barriers. This energy structure is reminiscent of atomic spectra, and QDs are sometimes referred to as artificial atoms. By changing the size or shape, the electrical and optical properties can be tailored.

The concept of semiconductor-based QDs was first proposed by A. Arakawa and H. Sakaki in 1982[27] as purely a thought experiment that discussed the advantages of having a band structure with discrete energy levels and radiative recombination. They asserted that the radiative recombination could be temperature insensitive if the intraband separation was much larger than kT at room temperature, which does not hold true for holes in the InAs/GaAs or InAs/InP material system. The first demonstration of a QD laser was in 1994,by using Indium Gallium Arsenide (InGaAs) on GaAs. Mirin et al. demonstrated the first room temperature photoluminescence (PL) with clear evidence of Stranski–Krastanow (SK) growth of QD by MBE, showing evidence of the theorized atom-like density of states[44].

The term self-assembled QDs refers to using the SK growth mode to form QDs simply by supplying In and As atoms onto the surface without pre-patterning. In SK growth, the initial monolayers of material wets the surface with a conformal layer. The layer-by-layer growth continues until a critical thickness, governed predominantly by strain, is reached, after which the growth rapidly transitions to 3-D growth of self assembled islands. The fundamental principles driving SK growth, particularly in the process of QD formation

are explained in great detail in [45].

Because the kinetics of SK growth are governed heavily by strain, adatom mobility, and surface morphology, MBE is a well suited technique for highly tunable growth conditions necessary for repeating important parameters such as dot density or PL full width at half maximum (FWHM). Many studies have investigated the growth conditions that affect dot quality, some of which are temperature, growth rate, growth interruptions, V/III ratio, As_2/As_4 ratio[46, 47, 48, 49, 50, 51], and the use of a high temperature anneal known as an indium flush[52]. Additionally, QDs can be grown in a InGaAs QW which is referred to as a dots in a well (DWELL), which can have varying composition and thickness[53, 54].

The lasers analyzed in this dissertation were grown without major changes to the growth recipe discussed by Norman et al. in [55]. Predominantly, the indium growth rate was adjusted to change the InGaAs well composition from 13.5 to 14.5%, while leaving the deposition time constant. This small change, which alters the total InAs deposited from 2.24 to 2.43 monolayers and the growth rate from 0.1 to 0.107 ML/s, significantly alters the center wavelength of the PL. All QD layers were grown at 495°C, with a -3°C offset for 3" wafers. There was a growth interrupt around 1.3 monolayers, which is approximately at the initiation of island coalescence, which was observed in Reflection High Energy Electron Diffraction (RHEED). The V/III ratio used for the 2 nm prelayer of InGaAs before the QD growth is 15. Then, the QDs are grown with a relatively high V/III ratio of 35, to reduce adatom mobility and encouraging earlier dot nucleation. After 1.3 monolayers, during nucleation, a 1 second pause occurs and the remaining 1.1 monolayers is deposited in six bursts spaced by one second. After a ripening pause the QDs are capped with 5 nm of InGaAs and 2.5 nm of GaAs.

After the DWELL structure is grown and capped with GaAs, the sample is heated to 580 °C for 5 minutes to perform the indium flush. This allows the coalesced dots

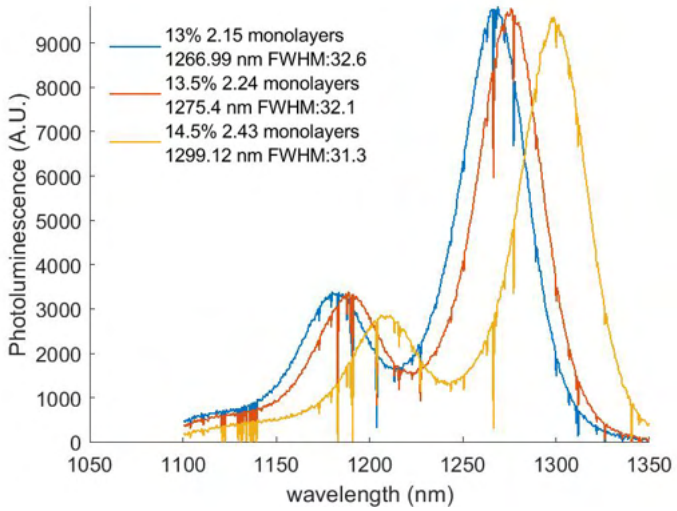

Figure 2.1: Measured PL from three samples grown the same day, each with a different InGaAs composition and total amount of InAs in the QD layer.

which protrude above the cap to either be removed through In evaporation or to reduce their height, while also allowing for Ga-In interdiffusion to make the dots more uniform, improving PL. After the In flush, a 35 nm GaAs spacer is grown in multiple QD-layer structures in order to prevent strain coupling between dot layers. Figure 2.1 shows how sensitive QD PL peak wavelength is to the amount of InAs deposited; the PL tunes 35 nm in wavelength with a 12% change in the amount of InAs deposited. For the system architecture discussed in Section 1.2, the device operation temperature and wavelength were specified. This required tuning the indium cell by as little as 0.1°C to tune the PL wavelength by 3-4 nm. The gain peak thermally tunes by 0.5 nm/°C, and a small error of 5 nm would result in a change of laser operating temperature by 10°C. This makes controlling the comb center at a specified temperature very difficult.

2.2 Epitaxial Layers for Quantum Dot Lasers

All devices discussed were grown on nominal (001) n-doped GaAs wafers with either a Varian GenII or VEECO GenIII solid source MBE machine. Either MBE system is capable of generating exceptionally-high-quality quantum dots with $6 \times 10^{10} cm^{-2}$ dot density and FWHM of 28 meV, so both systems were used interchangably. The details of the epi-stack are shown in Figure 2.2. The stack begins with a 400-nm-thick, highly-doped, n-contact layer. The aluminum content in the Aluminum Gallium Arsenide (AlGaAs) is then graded to 40% to form the waveguide lower cladding, which is 1.4 μm thick. The Al content is then graded to 20% for a 20-nm-thick confinement layer, before the active region. The active region contains either five[29] or six[56] DWELL layers, each separated by 37.5 nm of GaAs. The p-type cladding consists of the same Al concentrations and thicknesses, with a 300-nm-thick p-type, highly-doped, contact layer on top.

The doping of each layer is shown in Figure 2.2. The doping profile was optimized in order to give the best device efficiency. In a diode laser, there are three main sources that reduce efficiency: ohmic resistance, optical loss, and injection efficiency less than one. Considering the device through the perspective of conservation of energy, the laser output is usable energy removed from the system. Both optical loss, though scattering and absorption, and ohmic heating, are two sinks reducing usable energy extraction. Increased doping, particularly in the cladding and grading layers nearest the waveguide core, increases optical loss, through free carrier absorption and scattering, dopant absorption and scattering, and intervalence-band absorption. However, the increased doping helps reduce the series resistance of the device which reduces energy losses to ohmic heating. Therefore the doping is reduced in the grading layers and the p-cladding to optimize performance.

The growth temperature of the stack must also be considered for several factors. Due

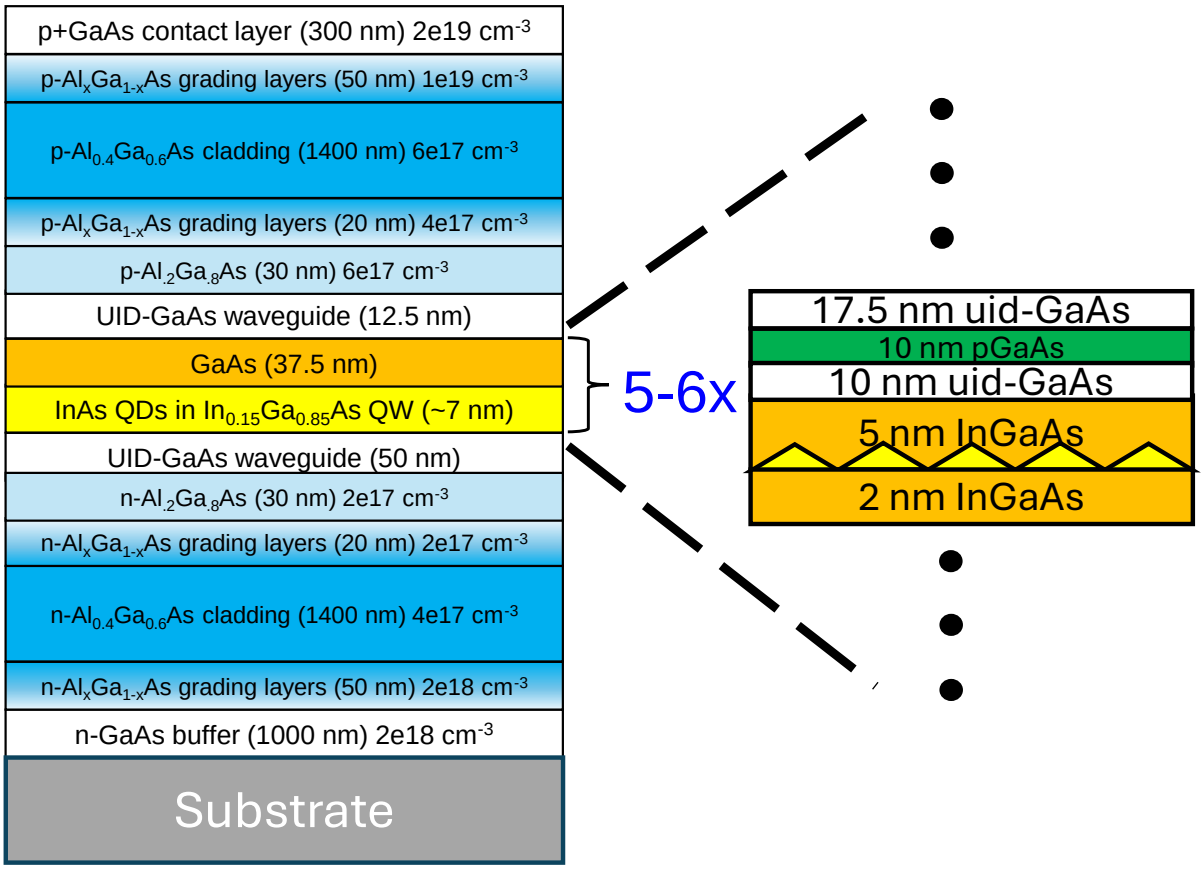

Figure 2.2: Schematic of the epitaxial layers used for the QD-MLLs in this dissertation.

to QD intermixing, the entire epi-stack above the QD layers is grown at 540° C. If a higher temperature is used, it will cause broadening of the PL, which degrades performance. Fortunately, incorporation of the p-type dopant, beryllium, into AlGaAs films is not heavily temperature dependent. The n-type $Al_{0.4}Ga_{0.6}As$ is however very sensitive to silicon incorporation [57, 58]. This is partially due to the high activation energy of Si in AlGaAs when Al content is over 22%, which are refered to as DX centers. They are the lowest energy level state for donors, and thus dominate the conductivity in the n-cladding[59]. This can be counteracted by incorporating higher Si levels, but avoiding Si incorporation in an arsenic sight, which compensates n-type doping. This is achieved by altering the As_2/As_4 ratio and substrate temperature to increase Si incorporation.

The incorporation and doping activation of Si in MBE AlGaAs films was studied via Secondary Ion Mass Spectroscopy (SIMS) in [60]. They found that the measured SIMS levels of Si decreased with increased arsenic overpreassure or increased substrate temperature. They believed arsenic was making a volatile compound with Si, which was removing it from the surface before incorporation. The doping level of $4 \times 10^{17} cm^{-3}$ was achieved in the n-type $Al_{0.4}Ga_{0.6}As$ by decreasing the growth substrate temperature from 580 to 560°C, decreasing the V/III ratio from 30 to 15, and decreasing the cracker temperature of the VEECO MrkIV Arsenic cell from 850 to 800° C, which increases the As_4/As_2 ratio. The change in As_4/As_2 ratio cannot be measured because the MBEs used do not have a direct way of distinguishing between As species during a flux measurements.

2.3 Fabrication

The epitaxial layers described in the previous section were processed into ridge-waveguide lasers of two different types. First the general fabrication steps involved in deeply-etched lasers will be described, and are presented in Figure 2.3, and most details of fabrication can be found in [61, 62, 63]. After growth, the first step is the deposition of p-metal, which is patterned in a liftoff process (a). The p-metal contact stack is Pd/Ti/Pd/Au. This is followed by deposition of 500 nm of SiO_2, which is patterned by dry etching to form a hard mask (b). The hard mask is used to dry etch the ridge waveguides with an inductively-coupled-plasma reactive-ion-etching process which uses N_2 and Cl_2 (c). The etch conditions were continually monitored and optimized to give vertical sidewalls with minimal sidewall roughness. Directly after etching, the sidewalls are passivated with 12 nm of atomic-layer-deposition alumina to reduce sidewall recombination, followed by 1 μm of sputtered SiO_2 (c). The n-via in the passivation is opened through dry-etching (d) and n-metal is deposited with electron beam deposition and pat-

terned with liftoff (e). The n-metal consists of Pd/Ge/Pd/Au. The p-via is then opened and 1μm of gold metalization is deposited for making electrical connections via probes or wirebonds (e). The substrate is thinned to 200 μm before depositing the same n-metal stack on the back of the chip for backside contact (for samples with n-type substrates). When all contact metal is deposited, the samples are rapid thermal annealed (RTA) for sixty seconds at 350° C. This makes the n-contact ohmic, and improves the resistance of the p-contact, yielding specific contact resistivities of about $2\times10^{-5}\Omega\cdot\text{cm}^2$ for both contacts. The samples are then cleaved using a Loomis LSD-100 or 155. This tool allows for precision scribing at finely tunable pressures, which is critical for cleaving and

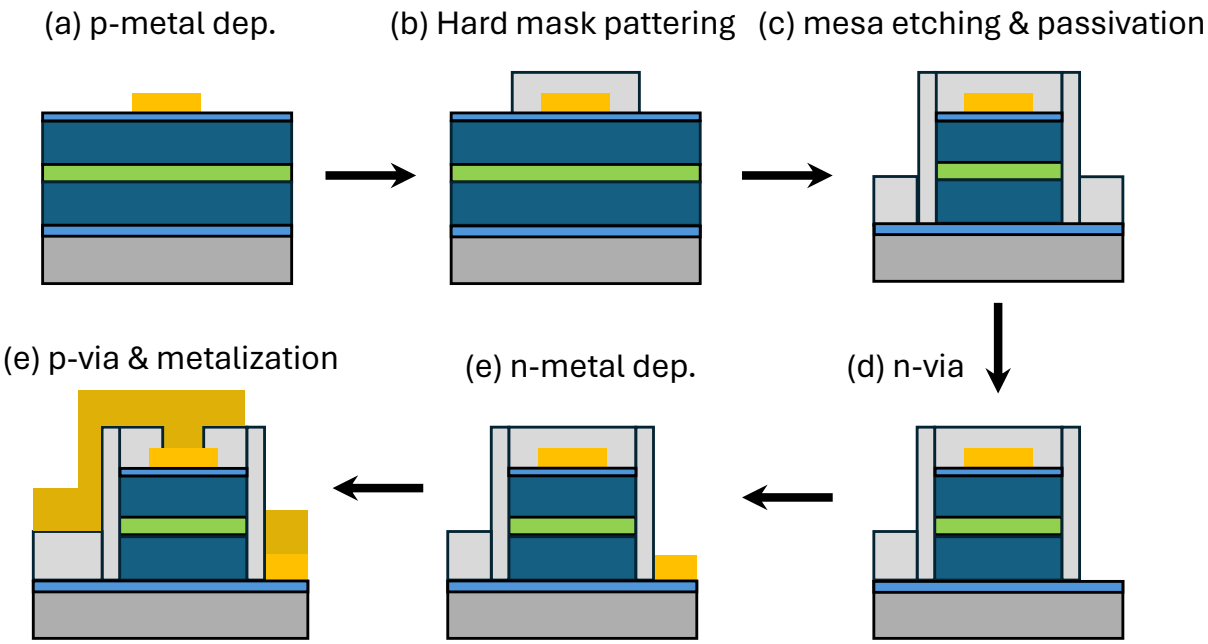

Figure 2.3: Overview of the fabrication process of deeply-etched QD lasers. (a) P-metal is deposited. (b) Hard mask is patterned for waveguide etch. (c) Laser mesas are etched and passivated with oxide. (d) N-via is opened. (e) n-metal is deposited. (f) P-via is opened and routing metal is deposited.

In addition, the general fabrication flow for shallow-etched ridge-waveguide lasers are depicted in Figure 2.4. The process is similar to the fabrication steps for the deeply-etched

lasers up until the waveguide etch. In the shallow-etched process, the waveguide etch stops at or above the active region, or equivalently at or above the 12.5 nm unintentionally doped (UID) GaAs layer in Figure 2.2. In actuality, it is possible to control the etch depth to an accuracy of 100 to 200 nm, so the target layer is the last 100 nm of the p-cladding, not the UID layer. In samples with backside contact, it is still necessary to have a topside n-type contact in order to allow for characterization (backside contact suffers from intermittent contact). This requires a separate dry-etch to the n-contact layer, which is shown in steps (d) & (e). This etch requires passivation to insure the n-contact does not short to the p-type layers that remain below the stopping point of the waveguide etch. A via in the n-contact area must be opened before deposition of the n-metal (f). Follow this, the p-via and metalization steps (g) & (h) are identical to the deeply-etched process, as well as the substrate thinning and backside metal deposition.

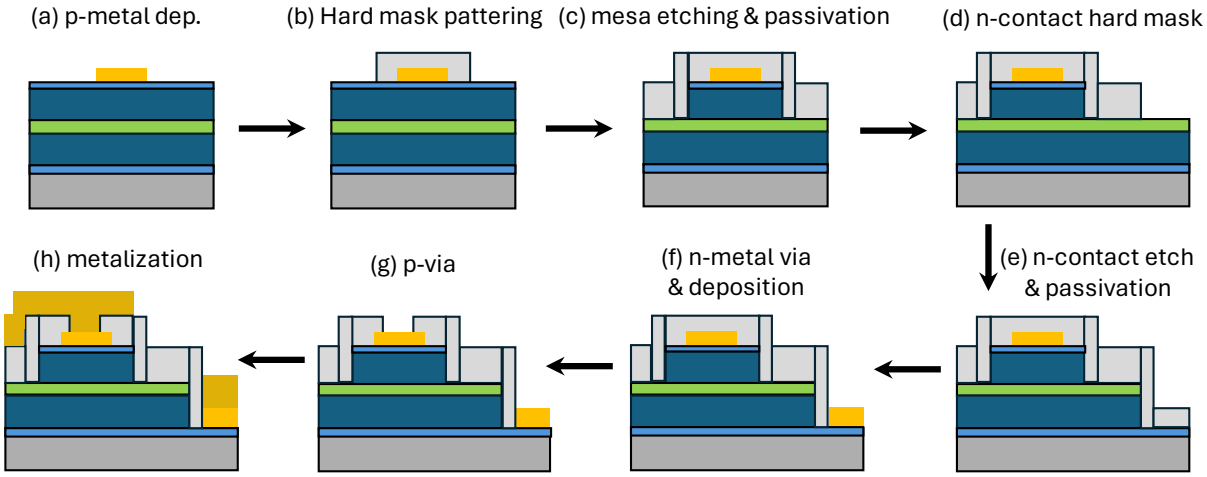

Figure 2.4: Fabrication process of shallow etched QD lasers. (a) P-metal is deposited. (b) Hard mask is patterned for waveguide etch. (c) Laser mesas are etched and passivated with oxide. (d) Hardmask for n-contact-etch is developed. (e) Openings for n-contact are etched and passivated with oxide. (f) N-via is opened and n-metal is deposited. (g) P-via is opened. (h) Routing metal is deposited.

2.4 Principles of Frequency Combs

OFCs represent a group of optical sources that have a periodically repeating output signal, which makes them coherent in time. This type of light output was first accomplished with a MLL[64], however other devices also emit OFCs such as Kerr solitons[9]. Taking the ideal case of a pulse circulating in a cavity with round trip
τ, every time the pulse strikes an output mirror, it would emit a pulse. This pulsetrain has a repetition rate of the pulse, $f_{rep} = \frac{1}{\tau} = \frac{v_g}{2L}$, where v_g is the velocity of the pulse. In the presence of dispersion, the speed that the pulse propagates is not equal to the speed of propagation of the electric field, v_c. This causes the position of the electric field inside a pulse to be slightly different from the preceding pulse (i.e. the pulse and the carrier wave walk off from one-another), and this phase shift that is added each sequential pulse is denoted with ϕ_{ceo}, called the carrier envelope offset phase. The pulse envelope function is periodic in time, but ϕ_{ceo} implies that the electric field is not. Thus the electric field can be defined as

$$E(t) = \sum_n E_n e^{i(n\omega_{rep}+\omega_{ceo})t}. \tag{2.1}$$

By imposing an added phase shift ϕ_{ceo} in the electric field at $E(t+\tau)$ from $E(t)$, and using the above definition of $E(t)$, this givs that $\omega_{ceo} = \dfrac{\phi_{ceo}}{\tau}$. This gives us the canonical definition of an OFC, that each frequency component is given by $f_n = nf_{rep} + f_{ceo}$, where $n >> 1$. Additionally, by taking the Fourier transform of the above definition of $E(t)$, each frequency component is spaced by f_{rep} and has an associated complex scalar, $E_n = A_n e^{i\phi_n}$. The phase term associated with each frequency component, ϕ_n is a scalar, and remains constant in time. The constant phase relationship of each frequency mode is an important result and the laser output is now referred to as mode locked. When the frequency of each mode is identical, ultrashort pulses are generated, however, other phase distributions exist which exhibit a constant phase relationship and do not emit

pulses.

2.5 Active Mode Locking

In active mode locking of semiconductor lasers, an electrical microwave signal is applied to the laser in addition to a DC bias[65]. The frequency of the modulation signal is chosen to be the free-spectral-range (FSR) of the laser cavity, which is typically in the GHz range. This is different from gain switching, where the frequency is not at or near the FSR, and
locking, typic
phase[67] or t
device is show
the gain secti
tegrated laser

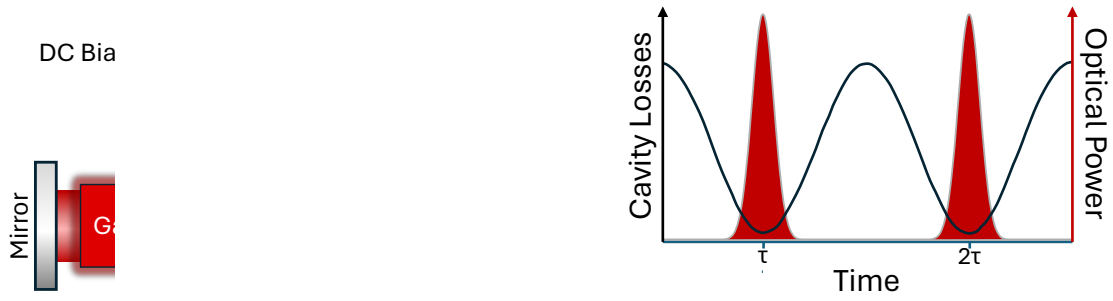

Figure 2.5: (a) is a diagram of a active mode locked semiconductor laser. The microwave bias can drive either the gain material or the modulator. (b) is a diagram of the cavity loss and internal power vs time. RF: radio frequency OC: Output Coupler, τ: round trip time

The case of cavity loss modulation is considered in Figure 2.5b. The frequency of the microwave signal is chosen to be near the FSR of the laser, such that the signal has a period equal to the round trip time of the laser cavity, τ. This causes a pulse

of light with the correct timing to pass through the modulator, while suppressing stray light at other times. Secondly, the leading and trailing edge of the pulse are attenuated by increased modulator loss, which is a pulse narrowing phenomenon. In the frequency domain, the individual longitudinal cavity modes, with slightly uneven frequency spacing, develop sidebands with equal frequency spacing. The sidebands are very near the adjacent longitudinal modes, which shift the modes via frequency pulling and create a cross-coupling between modes [69], creating a mode-locked state. This can be done at a harmonic frequency of the FSR, which increases the number of pulses circulating inside the cavity.

2.5.1 Passive Mode Locking

Passive mode locking is the most widely used form of mode locking; it allows for a optical frequency comb to be formed without the need for any active stabilization or modulation. This allows for the repetition rate of the device to be governed by the round-trip time, which can be made very small in integrated photonic devices, allowing repetition rates up to 100 GHz or greater to be achieved. Additionally, using a passive process eliminates the need for the active components in the previous section: particularly the microwave oscillator and modulator. This greatly simplifies the components necessary for the production of integrated MLLs on-chip. Perhaps most importantly, passive mode locking allows for the generation of extremely narrow temporal pulses. Through different passive processes, optical pulses with femtosecond temporal duration can be generated. The ability to generate such narrow pulses has found a large number of applications in science and engineering.

Even though the emission of periodically repeating optical pulses is often the goal of passive mode locking, it is not a requirement and a more general definition of mode

locking is required. Any signal that has an exact repeating nature in time requires that both the amplitude and phase of its frequency are constant, by virtue of the Fourier transform. This makes no assumption about ϕ_n for each frequency component, except that it is constant. If the phases of each component are contrived to be equal, then the output signal will be a pulsetrain, as discussed in Section 2.4. Because the amplitude of this signal is being periodically modulated, particularly if it was recorded with a high speed PD, this state is referred to as amplitude-modulated (AM) mode locking, because of its similarities to an AM encoded signal in the radio frequency (RF) scientific field. This is a common state in MLLs, and is often the goal. However other states of synchronization between the different modes of the frequency comb can exist and are stable. Other MLLs produce a nearly-continuous-wave (CW) output, which can be produced when the instantaneous frequency of the laser is being swept in a sawtooth-pattern. The nearly constant-power output with continually changing frequency is akin to information encoded in a frequency-modulated (FM) signal in the RF field, and is referred to as FM mode locking, and combs that exhibit this are referred to as FM combs. The differences will be discussed here and an in-depth analysis of FM-comb formation in QD-MLLs will be discussed in Chapter 4.

2.5.2 AM Mode Locking

In passive mode locking, the modes are phase locked through a nonlinear element in the laser cavity (Figure 2.6a)[70]. When the dynamics of the nonlinear element enhance the in-phase locking of modes, this causes self modulation of the intercavity light leading to optical pulses. In solid state lasers such as Ti:Sapphire, this is typically achieved with Kerr lensing[71, 72, 73]. However, passive mode locking is most commonly done with a saturable absorber (SA)[74, 75], which has a power dependent loss / absorption[76].

SAs provide both t

also typically achie

phenomena, which

active mode lockin

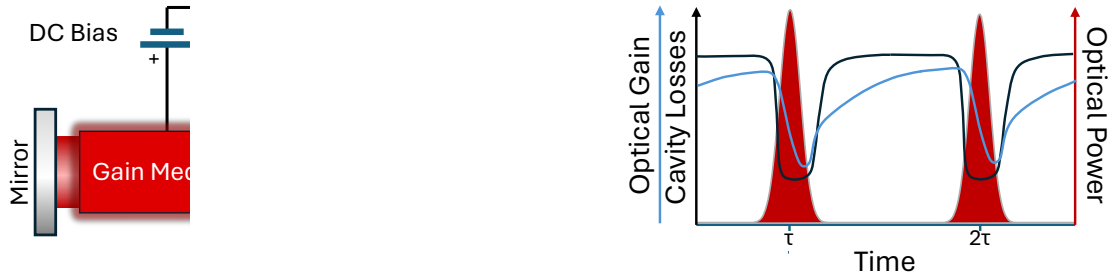

Figure 2.6: (a) is a diagram of a passive mode locked semiconductor laser. The SA is reverse biased with respect to the gain section. (b) is a diagram of the optical gain, cavity loss, and internal power vs. time. OC: Output Coupler, τ: round trip time

Semiconductors make an ideal material for SAs, because they undergo spectral hole burning, carrier heating, carrier depletion, and recovery[78]. The first demonstrations of passively mode locked semiconductor lasers were achieved with external nonlinear elements[79] and SAs[80]. By using an electrically isolated section of the gain medium in semiconductor-diode MLLs, the SA can be integrated into the laser cavity[81]. This allows the absorption to be perfectly matched to the the gain spectrum of the laser. The generation rate of electron-hole pairs in optical absorption is proportional to incident flux of photons and the absorption coefficient of the material, which is very large even near the bandedge in III-V semiconductors[82]. This makes semiconductors ideal material for saturable absorbers, and is the reason why semiconductor saturable absorber mirrors (SESAMs) are used in passive MLLs[78]. The fast bleaching in the absorption is shown with the steep leading edge in the cavity losses in Figure 2.6b, which attenuates the leading etch of the pulse, narrowing the pulse. The absorption recovers slower, because

the electron-holes must either recombine or be removed by an external electric field, which is depicted in Figure 2.6b with the shallower trailing edge of the cavity loss. This leads semiconductors to be classified as slow SAs. Applying an electric field to remove the carriers by an applied reverse bias recovers the absorption much more rapidly than recombination[83] (The SA is reverse biased in Figure 2.6a). This helps to attenuate the trailing edge of the pulse to narrow the pulse, but stable mode locking can still be achieved with a slow saturable absorber (recovery time)[75].

2.5.3 FM Mode Locking

In contrast to AM combs, other states of mode-synchronization exist that do not produce temporal pulses in the output. These states have been widely observed in quantum cascade lasers (QCLs)[84, 85] and have also been reported in III-V interband lasers based on 1310 nm InAs/GaAs QDs[86, 56], 1550 nm InAs/InP quantum dash (QDash)[87] and QD[37], as well as more traditional QW based lasers[88, 89]. Additionally, an important distinction of FM combs is their ability to form in single section / FP cavities; they do not require additional elements such as SAs in passive AM mode locking or modulators in active mode locking. Instead, FM combs were first discovered in FP cavities (without SAs) in QW lasers [90, 91], and have been observed in QCLs[92], 1310 nm QD lasers [38, 93, 94], QDash lasers[87, 95], 1550 nm QD lasers[37]. Because FM combs can be formed in FP cavities, they have gained interest, potentially offering the simplest and most power and size efficient implementation possible for comb generation, making them highly desirable for intgrated solutions where miniaturization is important. The dynamics of FM combs are discussed in detail in Chapter 4.

An important distinction to be made, the FM mode locking discussed here is self-starting and requires no externally controlled elements to form. This is in stark contrast

to FM combs formed by implementing a phase modulator inside the cavity, in a manner similar to active mode locking, but periodically modulating the intercavity phase [67, 96, 97] instead of the amplitude.

2.5.4 Colliding Pulse Mode Locked Lasers

Currently, DWDM networks typically operate at 50 or 100 GHz channel spacing and the lasers presented in this dissertation were designed for 60 GHz operation. When channel spacing exceeds 30-40 GHz, the cavity length becomes prohibitively short for QD-MLLs, and the laser gain cannot overcome the losses with enough headroom for high-quality or high-temperature passive-mode locking. In order to achieve 60 GHz spacing, colliding pulse mode locking (CPM) was employed to raise the channel spacing of lasers to multiples of the cavity FSR [98]. As an alternative to CPM, single section mode locking can also be used to remove the saturable absorber, which reduces the required net modal gain, and allows for higher channel spacing [93].

In CPM, the SAs are placed in a location that creates multiple pulses circulating in the cavity, which raises the repetition rate of the laser by an integer multiple equal to the number of pulses. This is accomplished by placing multiple SAs at integer fractions of the total cavity length. The denominator of the fraction is equal to the number of pulses circulating, and is known as the harmonic order (*i.e.* 3^{rd}, 4^{th} or 5^{th}), which is 3^{rd} in Figure 2.7a. When two pulses collide in the SA, they mutually bleach its absorption, which creates a lower-loss state in the laser than one pulse circulating. This moment is shown in Figure 2.7a at the right SA. In each instance that a pulse propagates through an SA, there is always another pulse to collide with it. For stability, the SAs closest to the two output facets must be included. The SAs at other positions in 4^{th} and 5^{th} harmonic lasers can be excluded.

The goal of CPM is to increase the channel spacing of MLLs, which is accomplished through increasing the repetition rate of the laser by the integer equal to the harmonic order. The Fourier transform of this higher frequency pulse-train gives a spectrum with greater frequency spacing between components. However, the fundamental modes of the laser cavity, which are spaced by a single FSR, are still present in the optical spectrum. These modes are considerably suppressed, as can be seen in Figure 2.7b. In this dissertation, this suppression is refered to as side mode suppression ratio (SMSR), and a SMSR of 30 dB or greater can be achieved for optimal states. This is a different use case than what is typically discussed for DFB lasers. The definition and analysis of SMSR is discussed in Subsection 3.5.1.

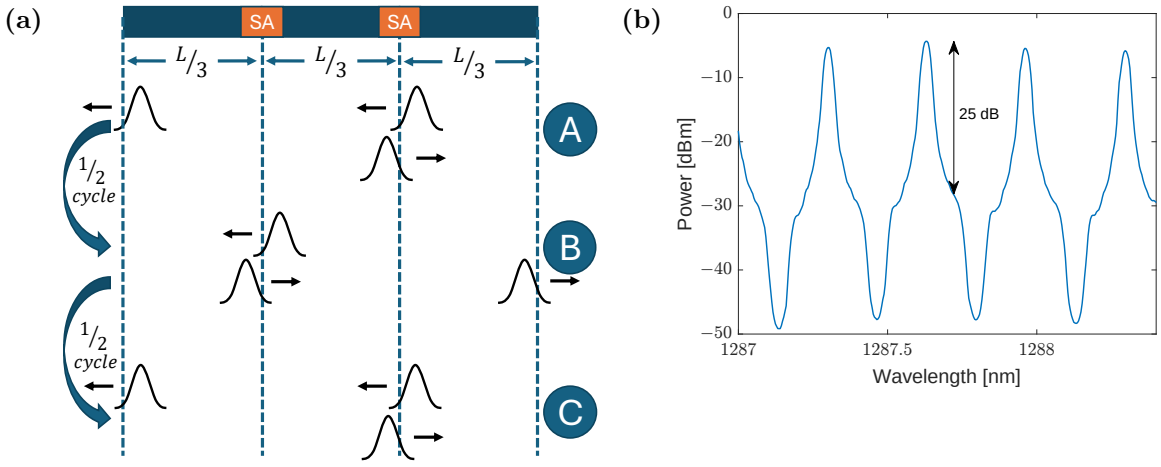

Figure 2.7: (**a**) Diagram of multiple pulses circulating in a 3^{rd} harmonic CPMLL. A pulse is emitted from a facet per cycle. In position A, two pulses are colliding in the right SA and a pulse is being emitted from the left facet. The position of the three pulses a half cycle later is shown in position B. Two pulses are colliding in the left SA and a pulse is being emitted from the right facet. In position C, one full cycle has been completed and the position of the pulses are analogous to position A. (**b**) Enlarged Optical Spectrum of a 3^{rd} harmonic CPMLL with high SMSR.

2.6 Conclusion

The aspects of producing QD-MLLs as well as their principles of operation were discussed in this chapter. The specific steps and growth conditions used in QD growth by MBE were explained. The sensitivity of QD PL-center-wavelength was also covered. Then, the fabrication processes necessary for producing devices were covered. Two different fabrication processes were covered, with the latter, shallow-etched, used for the devices in this dissertation.

Then an overview of the operational principles of MLLs was presented. The two overarching types of mode locking, active and passive, were briefly described. Passive mode locking requires no microwave frequency generators or feedback signals, offering a simple turnkey operation to generating OFCs. Two different types of passive combs, AM and FM, were distinguished. FM combs are of particular importance in this dissertation for producing many of the desirable aspects of a multi-wavelength source, and are discussed in great detail in Chapter 4.

Chapter 3

Efficient Comb Formation

3.1 Introduction

The footprint and power consumption requirements of copackaged optics necessitates optical sources with high data transmission capacity and high optical channel count, which has already been motivated. QD-MLLs simultaneously meet both of these needs, providing a large channel count and channel spacing to supply aggregate data rates of 12 Tb/s[36] and greater with a single compact turnkey source. However, there is an alternate metric, power efficiency, that is equally as important for the next generation of copackaged optics. The system power consumption requirements severely restrict the electrical power available for the laser to generate the optical carrier frequencies. Traditionally, one metric existed to describe the efficiency of lasers, known as the WPE. However, throughout this section analysis will be derived for the characterization of combs to better analyze their efficiency in DWDM systems. This approach is designed around a system viewpoint, where each channel has its own link budget and power allocation.

3.2 Wall Plug Efficiency

The output of a laser is generally characterized with a light-current-voltage (LIV) measurement, where the voltage and output power are measured as the current injected into the gain region is swept. The light-current (LI) is shown in Figure 3.1(a)[29], and voltage is omitted for clarity. The WPE is defined as

$$WPE = \frac{output\ power}{voltage \times current}, \tag{3.1}$$

which simply divides the power out of the laser by power in and it can be calculated for every point along an LIV curve, and this is shown in Figure 3.1(b). This figure of merit is used in a systems calculation to convert the optical power needed in a link budget to electrical power required and vise versa, for the case of a single frequency laser such as a DFB or distributed Bragg reflector (DBR) laser, where effectively all the output power is at one wavelength. With a multi-wavelength source, this analysis cannot describe how the power is distributed across the different wavelengths. Additionally MLLs have an SA, which affects the output power and WPE as the applied voltage is changed. This in general complicates the analysis.

3.3 Free Space Power Analysis of Mode Locked Lasers

The light-current and single sided WPE curves for 60 GHz 3^{rd} harmonic CPMLLs are shown in Figure 3.1 (a) and (b). The devices were tested continuous wave on a temperature controlled copper heatsink at 20°C. An integration sphere was used to measure light output, and voltage was measured in a four-wire or four-terminal configuration. The total SA length, as a fraction of the cavity length (2048 μm) is labeled on the respective curves. The performance of the devices are shown under two conditions; the first is with

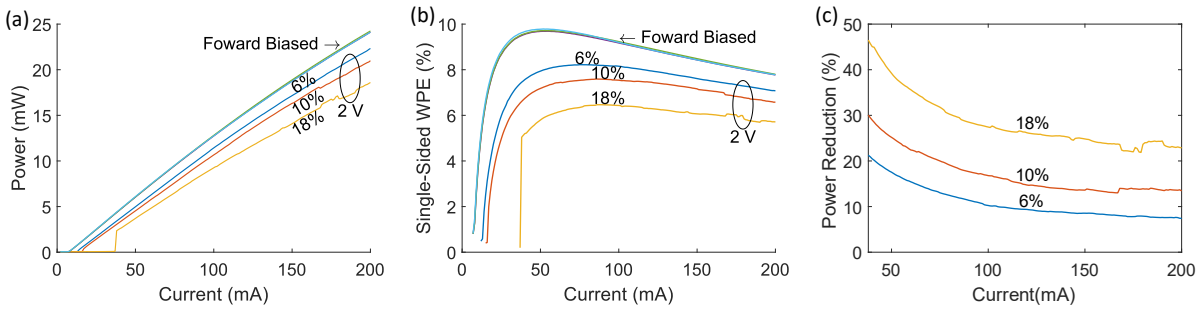

Figure 3.1: (a) shows the LI for three devices, which are identical except for the ratio of the SA to the total cavity length(6, 10, and 18%). Each laser has two LI curves: one with the SA forward biased in parallel with the gain section and one with the SA reverse biased at 2 V. (b) shows the wall plug efficiency for the devices in (a). (c) shows the reduction in power between the forward and reverse biased LI curves. Figure taken from [29]

the SA sections connected in parallel with the gain section (labeled forward biased), and the second is with the SA sections reverse biased at 2 V (labeled 2 V). The forward biased performance mimics the expected performance of FP lasers of the same design (i.e. lasers with no SA section). There is no significant difference in the light output or voltage between the three devices. When the SA is reverse biased, the decrease in output power due to the SA is clear. The small penalty in efficiency imposed by the SA creates equal frequency spacing between comb lines. The decrease in output power as a percentage of forward biased power is shown in Figure 3.1 (c). When considering devices with shorter SA sections, which will later be shown to be optimal for comb generation, the decrease in output power and WPE is only in the 10-20% range.

3.4 Two-Dimension Mapping of Mode Locked Lasers

The light output from the device is collected with PM fiber, which allows for data to be acquired with standard fiber-optic test equipment. The test setup is shown in Figure 3.2a, with the QD-MLL on the left. The DC gain drive current and SA bias voltage is supplied

by a dual channel source meter unit (SMU), which for most measurements is a Keithley 2600. The output light from the QD-MLL is collected by a PM lensed fiber, which is directly followed by an optical dual-stage isolator. This is followed by a series of optical splitters, with the splitting ratios listed in the diagram. All fiber hardware used is PM. Block (i) contains the optical analysis of the light collected, which includes an optical spectrum analyzer (OSA) and power meter. Block (ii) represents the RF analysis of the output light. The RF signal is generated by the high speed PD, but the frequency is to high for the electrical spectrum analyzer (ESA). A mixer and LO are used to shift the RF signal into the bandwidth of the ESA. Block (iii) contains the equipment used to analyze the optical pulsetrain that is gene
which generates a autocorrelation
the oscilloscope. A SOA is used to

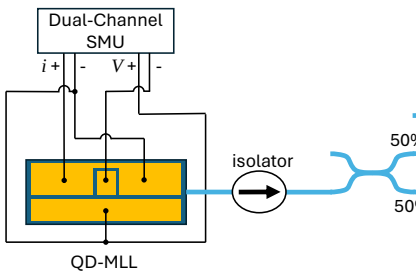

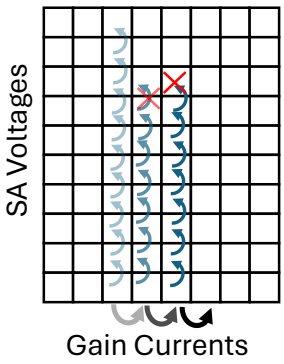

Figure 3.2: (a) shows a the measurement setup used to collect data to analyze the performance of QD-MLLs. (b) shows how the 2-D array of data is measured for given SA voltages and gain currents.

Figure 3.2b shows the order in which data is collected. An array of gain currents, typically 30-230 mA in 5 mA steps, and SA biases, typically 0-6.9 V in 0.3 V steps, are defined, which creates a matrix of all possible combinations of these two arrays. This is shown as the 2-D grid of boxes in Figure 3.2b. First, the gain current is set to a

value, then the SA is set to the first element in the array, 0 V. The fiber coupled power, optical spectrum, electrical spectrum, and autocorrelation trace are recorded along with the voltage and current of of the gain as SA section. The voltage is increased by 0.3 V to the next value and the same data is collected again for this data point. The SA voltage is increased (represented by the blue arrows in Figure 3.2b) until the 6.9 V is reached on the SA, unless the current compliance of the SA is reached or the laser stops lasing from the increased loss from the SA. If the compliance of the SA is reached, the data is collected for this point but the SA bias is not increased further ($\times$ on the arrow). If it is detected with the OSA that the laser is no longer lasing, no data is collected for that point ($\times$ in the square). The current is then increased to the next value and the SA voltage is swept again. This is done over the range of injection current values and when this is completed, data has been collected for all possible points of the matrix of injection currents and SA voltages. The data from each point is analyzed to extract key metrics, which are then plotted in 2-D color-coded plots in the following sections.

3.5 Optical Spectra Analysis

The analysis of the optical spectra collected from the method described in the previous section can be analyzed in several ways. There are several important metrics to OFC, and it is useful to analyze all spectra collected and plot each metric over the range of gain and SA biases. These 2-D color-coded plots are used to benchmark the performance of devices and to compare across different design parameters. The analysis techniques for finding the metrics are described in the following subsections.

3.5.1 Side Mode Suppression Ratio of Colliding Pulse Mode Locked Lasers

As was discussed in Subsection 2.5.4, the CPMLL geometry is used to increase the channel spacing of OFC. The fundamental FP modes are still present in the optical spectrum, and are spaced by the FSR of the cavity. The ratio of power between the enhanced and suppressed mode (or modes for higher harmonic CPMLLs) is defined as the SMSR, given by the following equation.

$$SMSR = \frac{power_{enhanced\ mode}}{power_{suppressed\ mode}} = power_{enhanced\ mode}[dB] - power_{suppressed\ mode}[dB].$$

An example calculation of this is shown in Figure 3.3: the collected optical spectrum from a particular gain and SA bias (120 mA, 1.5 V) of a 2^{nd} harmonic CPMLL is shown in Figure 3.3b, where every other mode suppressed. The enhanced modes are marked with yellow asterisks (*) and the suppressed modes with blue asterisks (*). Additionally, the twenty contiguous modes with the highest power are selected and shown with red asterisks (*), and the twenty-one suppressed modes surrounding them are shown with cyan asterisks (*). These modes are being considered becasue they are important for the 20-λ DWDM system. Looking on the edges of Figure 3.3a, it is clear that for the areas outside lasing bandwidth, the SMSR is small, even for a state with excellent CPM. Thus, the SMSR calculation is restricted to the twenty contiguous modes with the highest power.

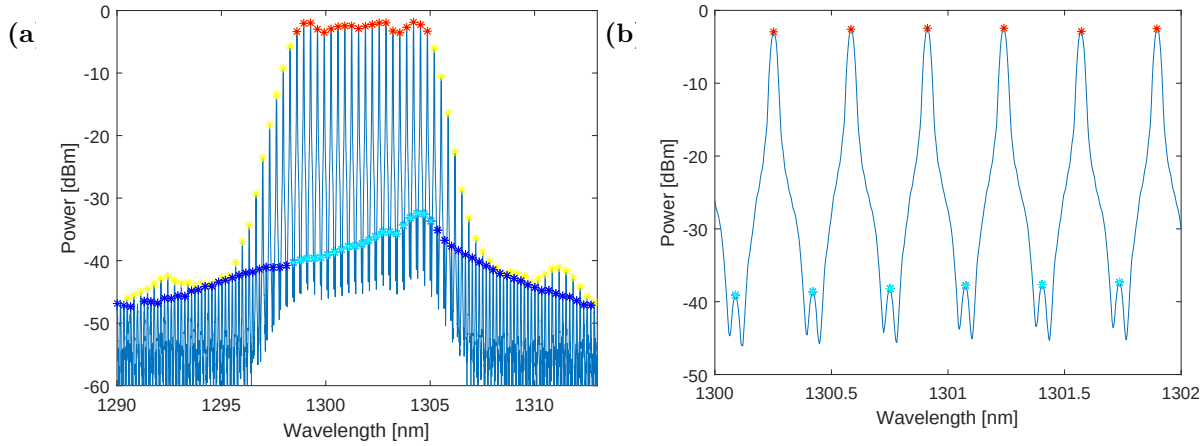

Figure 3.3: (a) depicts the identification of the enhanced modes (*) and suppressed modes (*) used in identifying side modes. The twenty contiguous modes of the spectrum are identified (with *) along with their corresponding side modes (with *). These are used to calculate the average SMSR of the state. (b) is a zoom-in of the middle of (a) to show the suppressed states clearly.

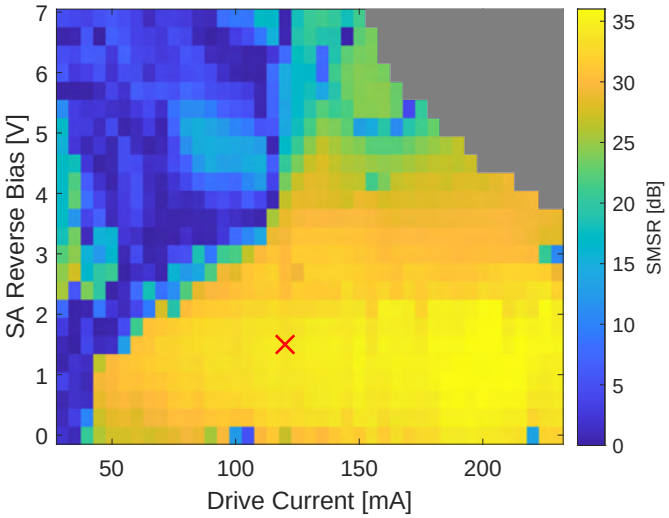

Figure 3.4: A color-coded plot of the average SMSR of each state measured for the 2^{nd} harmonic CPMLL. The state marked with a * shows a chosen operating condition for a 20-λ-DWDM system Greyed out region was not measured because compliance was reached in the SA section.

There are two values of the SMSR for each mode: one for the shorter wavelength and another for the longer wavelength side, which can be seen in Figure 3.3b, which is a zoomin of the center of Figure 3.3a. The smaller value for each mode is taken and

averaged for the twenty modes. This average is used to quantify the quality of the CPM and can be done for every spectrum collected in the 2-D array of gain current and SA values, as described in Section 3.4. The average SMSRs are displayed in a color-coded plot in Figure 3.4. The grayed-out region in the upper right corner was not tested because the current compliance was reached on the SA section, which prevents damage. These plots are useful for identifying the best areas of operation for generating OFCs. It is also relevant to compare the shape and area of states that have an SMSR $\geq$ 25 dB.

3.5.2 Comb Bandwidth Analysis

An important metric in characterizing OFCs is their optical bandwidth. The optical spectra, collected in the manner described in Section 3.4, are individually analyzed to calculate their bandwidth. The method for finding the bandwidth is depicted in Figure 3.5a, and starts with identifying the mode with the highest optical power, which is marked with a *. The bandwidth is then found by establishing the extent, or width, of the optical spectrum that is contained within a reduction in power from the peak, such as 3 or 6 dB. For this case, 6 dB cutoff is considered, and is shown with a dashed black line in Figure 3.5a. The continuous modes (which implies there are no gaps or missing lines) with power greater than this threshold are counted to find the bandwidth, and marked with *. For the spectrum in Figure 3.5a, there are 22 modes, and the modes are spaced by 58.2 GHz in this device, which gives bandwidth of 1.22 THz or 6.78 nm.

The bandwidth from every state measured is calculated and the results are shown in the 2-D color-coded plot in Figure 3.5b. The position of the state shown in Figure 3.5a is shown with a $\times$. This plot is useful for evaluating how the comb evolves over different bias conditions. There is a clear increase in bandwidth for states with high gain and SA biases.

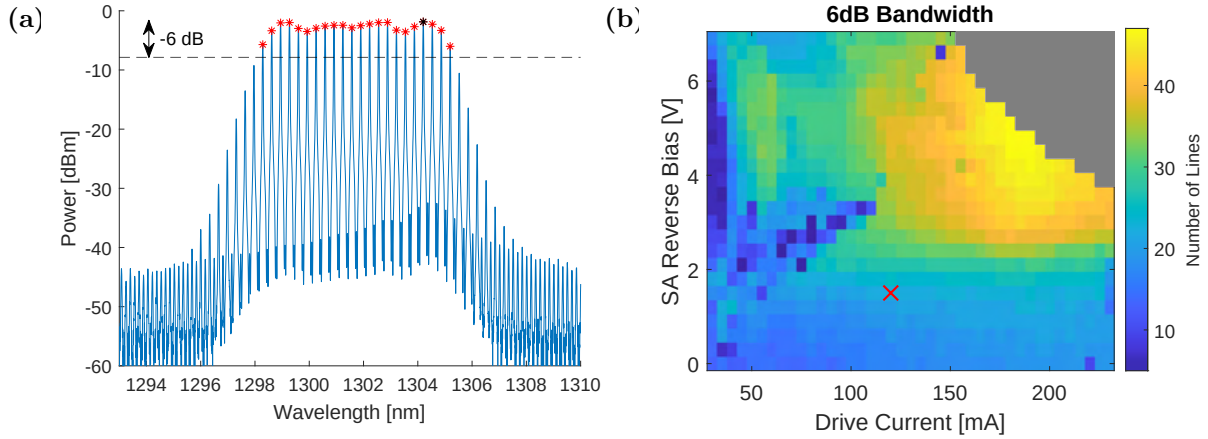

Figure 3.5: (a) depicts the modes that are contained within the 6 dB bandwidth of the spectrum. The highest power mode is marked with a * and the black dashed line represents the power level that is -6 dB below this mode. The modes that are above this level are contained in the 6 dB Bandwidth and identified with a *. The bandwidth of each spectrum, measured by the number of modes, is shown in (b). Greyed out region was not measured because compliance was reached in the SA section.

3.5.3 Individual Comb Line Power

The optical spectra can be further analyzed to understand how they can be used in a optical system for data transmission. In particular, these combs were designed for a 20-λ DWDM system, so understanding the performance of twenty comb lines was of particular importance. When data is encoded on each channel, there is an associated link budget requiring a maximum and minimum optical power for each channel, the latter being the major concern. Thus, it is useful to find the comb line with the minimum optical power and track this line over the 2-D array of gain currents and SA biases. The twenty contiguous comb lines (i.e. no gaps in the spectrum) with the highest power are identified in Figure 3.6a with *, and the comb line with the highest and lowest power are identified with a ◯ and ◯ respectively. The PoLL is tabulated for all states, and this is displayed in Figure 3.6b. This plot is very insightful for finding the optimum OFCs for data transmission. It is also possible to generate the 2-D plot for the power of the highest line and for the power difference between the highest and lowest line, but it is

not as useful for finding optimum states.

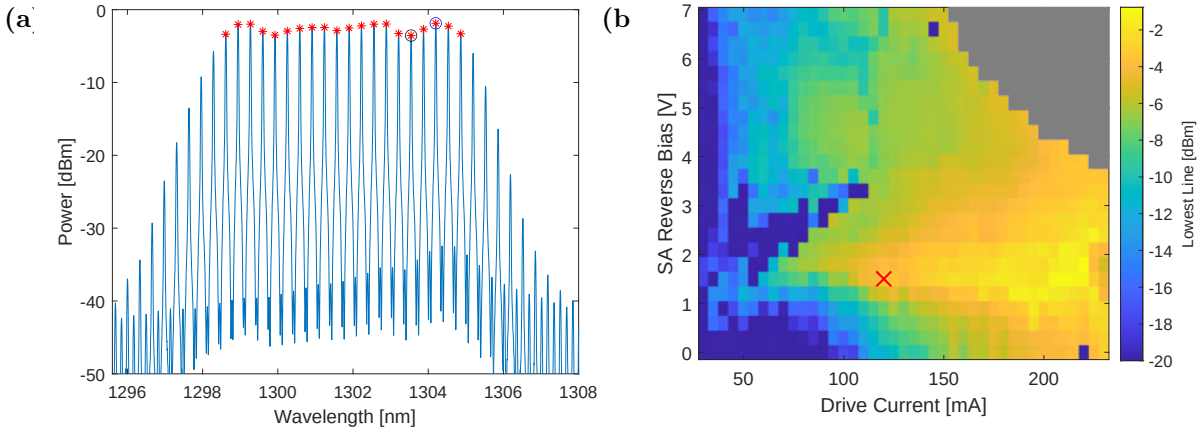

Figure 3.6: (a) An example optical spectrum with the 20 (b) 2-D color-coded plot of the comb line with the lowest power in a 20-λ comb. Greyed out region was not measured because compliance was reached in the SA section.

3.5.4 Individual Comb Line Efficiency

In addition to tracking the PoLL, the efficiency of generating each comb line is also a crucial parameter. This is calculated in a similar manner to WPE, but the power of each comb line is divided by the total electrical power consumed. Because the denominator is the same, the comb line with the lowest power will have the lowest WPE. This metric, referred to as wall plug efficiency of the 20^{th} line (WPE20), is calculated for every state and shown for the example device in Figure 3.7a. The example spectrum has the highest WPE20 out of any spectrum collected for this device, which is -26.13 dB. The value of PoLL is equal to -3.56 dBm and the power consumption is 180.65 mW or -22.57 dBm (and the WPE20 is found simply by the subtraction of the former from the latter when both are in dBm). The -26 dB metric was important because this signifies a WPE of 10% or better for each comb line. This remarkable device is able to produce an efficient 20-λ comb from 70 to 220 mA.

It is helpful to equate the WPE20 calculated in the previous paragraph to a linear

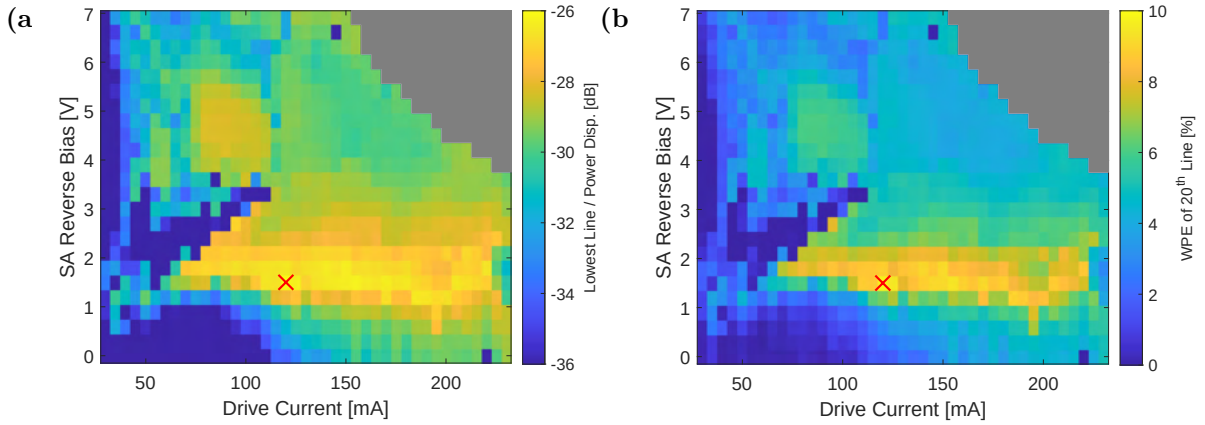

Figure 3.7: (a) shows the WPE of generating the 20^{th} comb line. The × shows the location of the state shown in Figure 3.6a. (b) shows the same information as (a), but assuming 20-λ spectrum, and using a linear scale to highlight the variation in high efficiency states

WPE value that was shown in Figure 3.1 and is (seldom) shown in data sheets. The power budget typically specifies an electrical power allocated per channel and a optical power requirement. Therefore, the electrical power consumption of the entire laser is divided by the number of channels, which is twenty in this document. Additionally, the lasers emit equal power from both facets, so the fiber coupled power is multiplied by a factor of two. The equal fiber power from both facets of the laser was confirmed with many devices both by LIV and fiber-coupled-LIV measurements of both facets and also confirming spectra were identical from both facets. Additionally packaged MLLs have two fibers per laser and show equal power per facet in the ideal case when both fiber attachments are done without significant fiber drift. The per-channel line efficiency is also more convenient to view in linear scale and is referred to as wall plug efficiency per channel (WPE/C). It is shown for the example device in Figure 3.7b. The example spectrum has a WPE/C of 9.76%. Comparing Figure 3.7a and Figure 3.7b and more generally the difference between a logarithmic and linear scale, the former shows better detail across all ranges and does not compress the lower efficiency states while that latter is better for comparing states that are closer to the top of the range, which is 10%

for WPE/C in this document. This device has an amazing bandwidth of producing all twenty wavelengths efficiently, allowing the PoLL to be tuned from -8 to -0.75 dBm by only tuning the gain, and leaving the SA bias constant at 1.8 V, with a WPE/C greater than 8%.

3.6 Electrical Spectrum Analysis

Optics enjoys the ability to detect the frequency and phase difference between two different wavelengths (or frequencies) of light by simply combining them on a PD, in a technique known as optical heterodyne detection[99]. This is used in coherent communication to extract information that is encoded on the phase and amplitude of an optical carrier. In contrast, heterodyne signals are created in electronics with a nonlinear circuit element, such as a rectifier, which has a quadratic response term. In photonics, the carrier frequency is too high to directly detect the electric field. Instead PDs convert optical power to photocurrent linearly, which makes them quadratic in response to the electric field. When the sum of the two electric fields are squared, it produces a cross term, which is responsible for the modulation of the photocurrent at both the sum and difference frequency of the two optical tones. In optical heterodyne detection, only the difference term is within the detector bandwidth, and is referred to as the beat note.

3.6.1 Fundamental Beat Note

The optical spectrum of MLLs are comprised of a large number of equidistant modes with a fixed phase relationship, where each mode is separated by the repetition rate of signal, f_{rep}. By virtue of a Fourier transform, this creates the periodic output signal with a period $\tau = 1/f_{rep}$. The periodic modulation of the amplitude can be detected with a PD, which produces an RF signal. However, more insightful analysis can be

understood in the frequency domain. The optical spectrum of the MLL is represented in Figure 3.8 with a series of complex scalars, $\boldsymbol{E}_m$, with an amplitude A_m and phase ϕ_m. $\boldsymbol{E}_m$ and $\boldsymbol{E}_{m+1}$ produce a heterodyne beat note signal, $\boldsymbol{B}_{m,m+1}$ at the frequency difference, $f_{m+1} - f_m = f_{rep}$, with an amplitude proportional to the product of A_m and A_{m+}

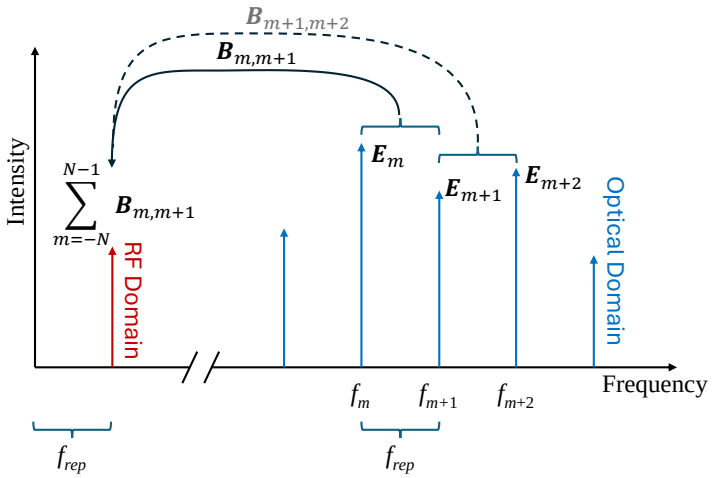

Figure 3.8: Diagram depicting the generation of a beat note. Each pair of optical modes creates a heterodyne signal, e.g. $\boldsymbol{B}_{m,m+1}$ for $\boldsymbol{E}_m$ and $\boldsymbol{E}_{m+1}$. This beat note has an amplitude and associated phase. The measured beat note, $\boldsymbol{B}$, is a complex sum of all heterodyne signals.

When the entire spectrum is incident on the PD, a heterodyne signal is produced from the sum of all the mode-pair beat notes, which is known as the fundamental beat note, $\boldsymbol{B}$, given by

$$\boldsymbol{B} = \sum_{m=-N}^{N} \boldsymbol{B}_{m,m+1}. \tag{3.2}$$

Typically the lineshape and magnitude of $\boldsymbol{B}$ is recovered with an ESA. If the phase of the individual beat notes are recovered, the phase of an individual comb line can be found through the following sum:

$$\phi_k = \sum_{m=-N}^{m=k-1} \Delta\phi_{m,m+1}, \tag{3.3}$$

assuming without loss of generality that $\phi_m = 0$. The full electric field can be recon-

structed with this information, with the assumption equating to a arbitrary delay in defining time $t = 0$. Further analysis in this topic is discussed in Subsection 4.3.1.

3.6.2 Measurement of the Fundamental Beat Note

The beat note generated by the RF PD and the MLL is analyzed with the ESA. The frequency corresponding to the harmonic beat note is around 58 to 60 GHz, which is above the bandwidth of most ESAs, including the one used for the following measurements. This requires the use of an electrical mixer and a LO to produce a difference, or intermediate, frequency that is within the bandwidth of the ESA. The frequency of the LO is chosen to be 39 GHz to produce an intermediate frequency around 20 GHz. Electrical spectra are collected for all available gain current and SA biases in the method described in Section 3.4. First, a broad sweep is completed, with a 4 GHz span, 100 kHz resolution bandwidth (RBW) and 100 kHz video bandwidth (VBW). If the peak of the trace exceeds -74 dBm, a finer resolution speed is collected with a 20 MHz span, 5 kHz RBW and 10 kHz VBW centered at the peak of the broad sweep. The finer scan is accurate enough to resolve the shape of the beat note, while also completing the scan quickly. Slower scans accumulate low frequency noise (particularly thermal fluctuations), which broaden the measured linewidth. Additionally, the Keithley SMU causes non-continuous jumps in the spectrum caused by digital feedback loop that controls the outputs for the gain current and SA bias, which can be seen Figure 3.9a around the peak. Faster acquisition time help to remove these noise sources and gives a more accurate snapshot of the beat note linewidth. A low noise current source must be used to capture an accurate beat note linewidth, however it would be too time consuming to map all devices with a low noise source.

3.6.3 Linewidth Extraction

The beat note is a good representation of all noise sources present in the laser (e.g. thermal, electrical, optical...), and thus the linewidth of the beat note is an objective metric for the noise level present in the state of the MLL. In particular, the square root of the beat-note linewidth is related to the timing jitter of the repetition rate of a MLL [100], but the devices here generally do not operate in a regime that generates pulses. The narrow electrical spectra collected are curvefit to extract the linewidth of the harmonic beat-note. This is typically done by fitting the data with a Voigt function, which is the convolution of a Gaussian and Lorentzian distribution. The use of a Voigt lineshape is complicated because the function does not have an analytical form and fitting the function is extremely difficult. The use of a Mathworks package for MatLab made the Voigt fitting possible. Figure 3.9a shows a spectrum, collected at the same bias conditions as the example optical spectrum in Section 3.5, that has been fit with the Voigt lineshape using the Mathworks package. It is plotted on a log scale, which exaggerates the fit error in areas with small signal, which would be the side wings of the spectrum, however this area doesn't have a large effect on the linewidth. Additionally, a large portion of the lineshape is hidden below the noise floor. To combat this, and data that constitutes the noise floor is removed before fitting. Only the data in black in Figure 3.9a is used for the fit. The linewidth extracted from this state is 103 kHz, which means it is likely being broadened by the noise from the Keithley SMU, because it is close to the minimum linewidth achievable using a Keithley SMU, which is roughly 50 kHz.

All the data collected is fit, and the extracted linewidths are plotted in a 2-D color-coded plot in Figure 3.9b. The Linewidth is plotted on a log scale to appreciate the entire range of values. This chart is very useful for identifying the useful areas of operation, which must have low linewidth. In general, states with linewidth greater than 2 MHz are

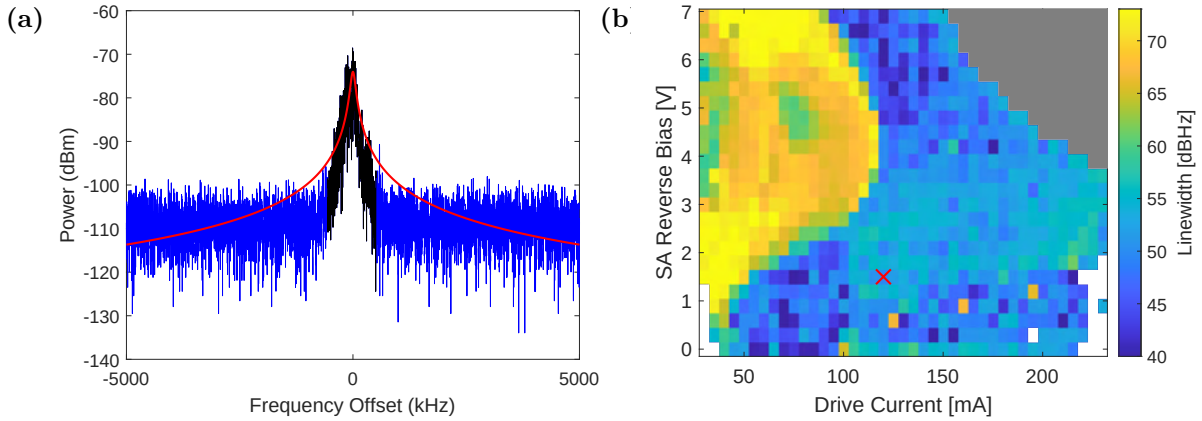

Figure 3.9: (a) shows the the fitting of the RF beat note collected by the ESA with a RBW of 5 kHz and a VBW (b) shows a 2-D color-coded plot of the extracted RF linewidth of all states. The × shows the location of the state shown in (a).

not usable, and states where the linewidth is below 2 MHz are usable. This fortunately corresponds to the area of efficient comb formation identified in Subsection 3.5.4, and this region will be discussed more in Chapter 4.

3.6.4 RF Power and Frequency

The ESA traces also give information about the RF power and frequency of the beat note. The RF power of the beat note is useful for understanding the comb dynamics, similar to the linewidth. The RF power and frequency are extracted from the broader sweep. The data is extracted from the sweep by establishing the point with the highest power and recording the power and frequency of this point. Figure 3.10a shows how the frequency tunes with gain current and SA bias. There is relatively little tuning with gain current, and large tuning with SA bias. This is fortunate, because it allows the gain to be tuned to different high efficiency states without changing the comb spacing. Figure 3.10b shows the change in RF power of the beat note across gain current and SA bias. There is a large change with SA bias and a small change with gain current surprisingly. This is attributed to the increased saturable loss in the laser at higher SA bias.

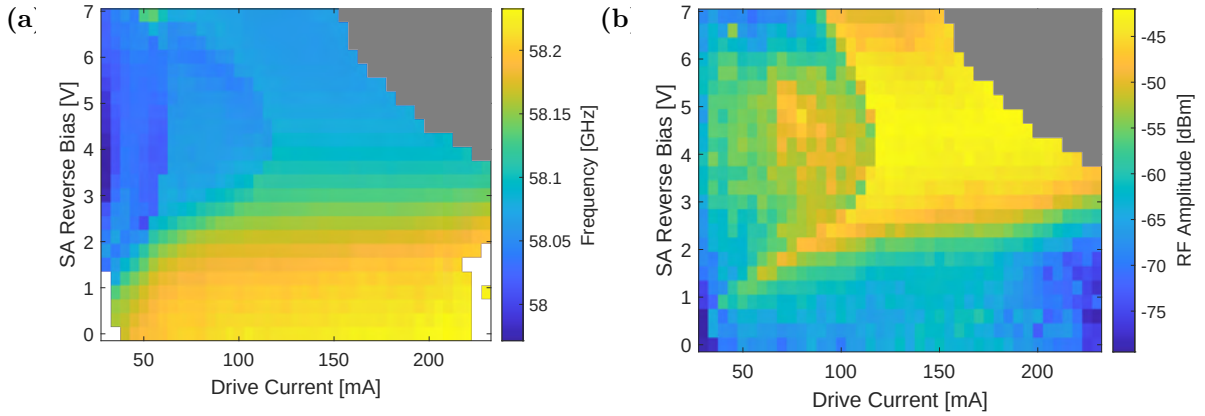

Figure 3.10: (a) shows a 2-D color-coded plot of the beat note frequency measured by the ESA (b) shows a 2-D color-coded plot of the maximum power measured of the beat note.

3.7 Autocorrelator analysis

To take a picture of an event, you need a shutter or strobe that is faster than the event being imaged. In general, the time resolution of imaging an event is limited by the minimum time aperture possible. However, the width of optical pulses with a 10 fs pulsewidth would require a detector with 100 THz of bandwidth. To circumvent this, the pulse itself is used as the time-aperture; the pulse is used to image itself. There are several measurement techniques developed to do this [101], and the process often used is known as an autocorrelation. The instrument used to measure the autocorrelation is known as a autocorrelator, and the type used for all measurements in this dissertation is shown in Figure 3.11.

The theory describing the output from the background-free autocorrelator is well documented[102]. When the output is averaged over several optical cycles, the output at the detector is equal to g^2, which is defined as

$$g^2(\tau) = \frac{\langle I(t)\, I(t-\tau)\rangle}{\langle |I(t)|^2\rangle}, \tag{3.4}$$

Ef

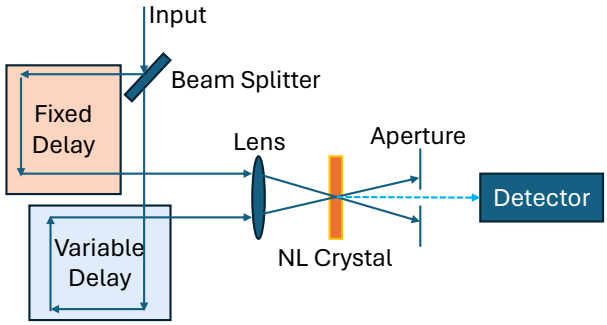

Figure 3.11: Diagram of a noncollinear second harmonic generation geometry which is found in background-free autocorrelator. NL: non-linear

where τ is the difference in the delay between the two arms of the autocorrelator shown Figure 3.11, and the range of the delay is normally around 50-200 psec. The optical delay is swept over a much larger time-scale than the delay itself. This means thousands or millions of pulses are interfered with themselves and time averaged through the collection of one trace. The AC outputs the autocorrelation trace as a voltage signal, which is captured by a real time oscilloscope. The data is averaged over 16 traces by the oscilloscope, which is collected by the computer. The timescale of the oscilloscope is converted to the optical time-delay with the conversion factor of 33250 psec/sec. An example trace is shown in Figure 3.12a. The AC used has a scan trace of 200 psec, and the repetition frequency of the laser is roughly 16.7 psec (for a 60 GHz harmonic repetition rate), which gives 12 pulses or cycles in one trace. Therefore, the length of the fixed-delay path should be carefully tuned to identify exactly which pulse is the autocorrelation, and which are cross-correlations, because only the autocorrelation pulse has an accurate pulse width (and timing jitter broadens the cross-correlation pulses).

3.7.1 Pulse extinction ratio

In order to analyze the autocorrelation, a simplified pulse extinction ratio, η_p, is defined in order to illustrate the different modes of operation in QD-MLLs. An example

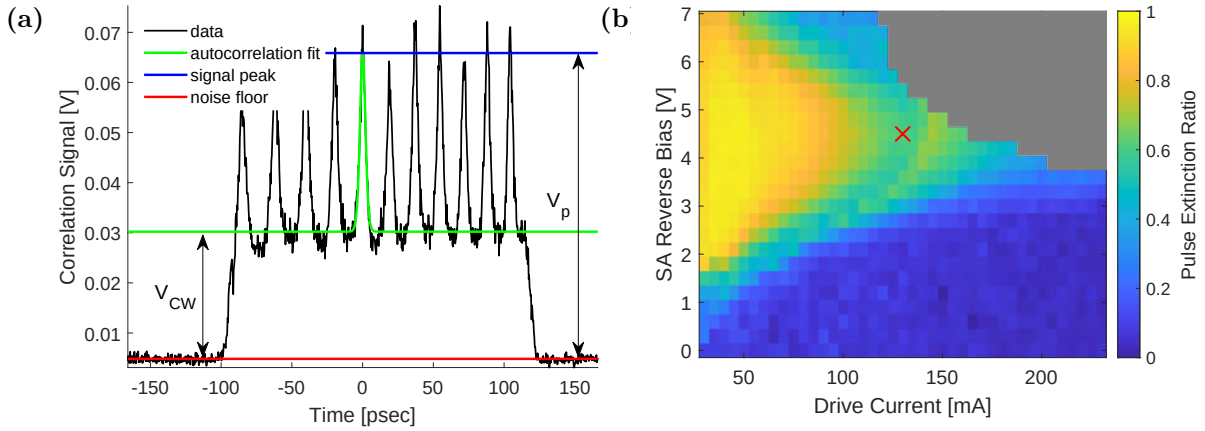

Figure 3.12: (a) shows the autocorrelation trace collected by the oscilloscope. The pulse power level, V_p, and CW power level, V_{cw}, are shown on the right. level are shown with black and blue line. (b) shows a color-coded 2-D plot of the extinction ratio for all states. The × shows the location of the state shown in (a).

of the process is shown in Figure 3.12a. The noise floor (which is very near zero) is identified to have a more accurate calculation. The CW level is established by smoothing the spectrum and identifying and averaging the four troughs on either side of the autocorrelation peak (which is at the zero time delay). The CW signal amplitude, V_{cw}, is the difference between the CW and noise floor, which is shown on Figure 3.12a. The pulse signal amplitude, V_p, is found by fitting the pulse (which is discussed in the next section). The fit is used because the peak level has considerable noise and the fit is more representative of the actual level. V_p is simply the subtraction of the peak value and the noise floor. η_p is defined by the following equation:

$$\eta_p = 1 - \frac{V_{CW}}{V_p} \begin{cases} \geq 0.5 & \text{(AM domination)} \\ < 0.5 & \text{(FM domination)} \end{cases} \tag{3.5}$$

A plot of η_p for all states measured is shown in Figure 3.12b, with the location of the example case from Figure 3.12a marked with a ×. This plot is useful for identifying different areas of operation, which were defined with the conditions listed in Equation 3.5.

The efficient states are located in the FM regime, where the pulse extinction ratio is low.

3.7.2 Pulsewidth

The pulsewidth is a key metric for all MLLs; it relates the phase relationship of comb lines to the temporal width of the pulse, through the time-bandwidth product[102]. The pulsewidth is conventionally measured with the FWHM of the intensity profile, which is found with an AC. A hyperbolic secant squared pulse shape is assumed for the pulses inside the QD-MLL, and it is given by

$$I(t) = \text{sech}^2\left(\frac{1.7627t}{\Delta t_p^{FWHM}}\right), \tag{3.6}$$

where Δt_p^{FWHM} is the temporal FWHM of the pulse. The autocorrelation of Equation 3.6 is given by

$$A^{(2)}(\tau) = \frac{3}{\sinh^2\left(\frac{2.7196\tau}{\Delta\tau_A^{FWHM}}\right)}\left[\frac{2.7196\tau}{\Delta\tau_A^{FWHM}}\coth\left(\frac{2.7196\tau}{\Delta\tau_A^{FWHM}}\right) - 1\right], \tag{3.7}$$

where $\Delta\tau_A^{FWHM}$ is the temporal FWHM of the autocorrelation trace. The two FWHM are related by

$$\Delta t_p^{FWHM} = 1.54\Delta\tau_A^{FWHM} \tag{3.8}$$

The function in Equation 3.7 is used to fit the data from the AC and the relation in 3.8 is used to find the FWHM of the pulse. An example of this is shown in Figure 3.13a, which is a zoomin of the pulse at zero time delay ($\tau = 0$). The curve has good fitting over the range, and the CW level is predetermined and input to the fit as a set parameter.

The pulsewidth is calculated for all states, and the results are shown in Figure 3.13b, with the state from Figure 3.13b marked with a $\times$. The state with the lowest pulswidth

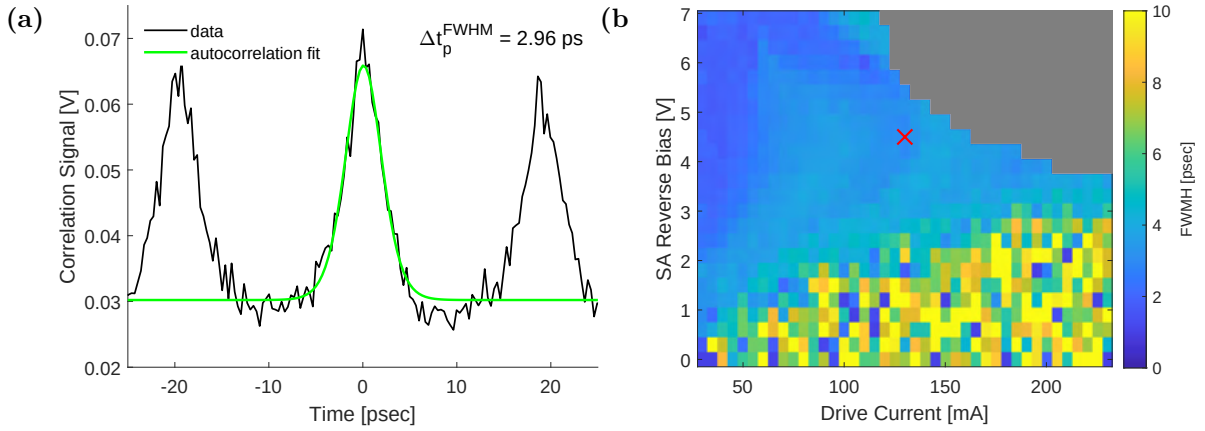

Figure 3.13: (a) shows a zoomin of autocorrelation trace collected by the oscilloscope around the zero time delay pulse, to illustrate the accuracy of the fit. (b) shows a color-coded 2-D plot of the pulsewidth for all states. The × shows the location of the state shown in (a).

is 110 mA and 6 V, with a FWHM of 1.78 psec. This is a relatively broad pulse, but these lasers are optimized for flat comb formation, not minimum pulsewidth. The area where the pulse extinction ratio is less than 0.15 cannot be fit accurately, because the amplitude of the pulse is on or below the level of the noise floor. The example state from Section 3.5 is plotted in Figure 3.14a, which has a η_p of 0.05. The fit analysis erroneously fits fluctuations in the power that are not at zero time delay. This is the cause of the large variation in the pulsewidth seen in Figure 3.13b. Therefore the area with low η_p is removed from the FWHM plot, which is shown in Figure 3.14b. This plot accurately shows the variation in FWHM for the states with visible pulsation. There is an area of low pulsewidth at high SA and low gain current, which is discussed in Chapter 4.

3.8 Conclusion

The various techniques developed for the analysis of QD-MLLs were detailed. The use of a multi-wavelength source requires more complex analysis of MLLs than single frequency lasers. The optical spectrum analysis was explained, and several key metrics for

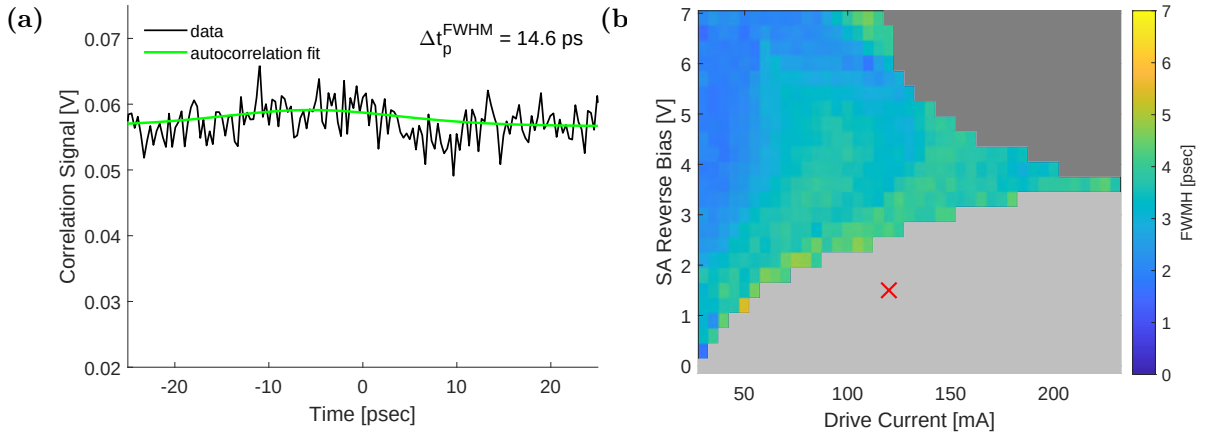

Figure 3.14: (a) shows a zoomin of autocorrelation trace collected by the oscilloscope around the zero time delay pulse. The data cannot be fit when the η_p is too small. (b) shows a color-coded 2-D plot of the pulsewidth for all states. The $\times$ shows the location of the state shown in (a).

benchmarking the performance of devices were defined, the most important of which is the WPE/C. Because MLLs emmit a periodic signal, additional analysis can be conducted. The electrical spectrum can be measured with a high speed PD and ESA, with the help of a mixer. This analysis is useful for gaining insights into the noise performance of the laser, by measuring the linewidth of the beat note. Lastly, the AC trace can be used to understand and identify the different regimes of operation present in QD-MLLs.

Chapter 4

FM Comb Formation

4.1 Introduction

The formation of FM combs establishes an exciting alternative to producing optical frequency combs to the traditional approach, which involves the production of optical pulses. Many of the desirable properties for multi-wavelength sources are found in FM combs, such as ultra-stable operation, broad combs with even power distribution, and self starting behavior enabling single-section MLLs[103, 37, 92, 90, 38], making them a highly researched topic. Traditional mode-locking was considered to only occur when all modes of the cavity are in phase with each other, giving rise to pulsating output. Unlike their AM counterparts, FM combs generate a quasi-CW output, which results in a flat-topped optical spectrum, giving equal power to all data channels necessary in DWDM systems.

Early efforts to produce optical frequency combs in QD lasers followed similar techniques used in QW devices, employing a two-section device geometry with an electrically isolated active region section acting as a SA[104]. Subsequent advancements allowed QD-MLLs to achieve transform limited pulses[105] and 400 fsec pulse duration[106]. Optical pulse generation occurs in AM mode locking states, where the phases of optical

modes are nearly identical, producing the narrowest transform-limited pulse when the phases are perfectly aligned[107]. SAs create coupling between cavity modes to achieve this, but several factors attribute to phase shifts being introduced between modes, causing a frequency chirp in the pulse. The intercavity dispersion causes pulse broadening through frequency chirp, and is especially challenging for semiconductor MLLs because it is generally difficult to implement broadband frequency chirp compensation in integrated platforms[108]. Additionally, the high peak power present in narrow pulses causes nonlinear phenomena such as gain saturation and self phase modulation[70], which both attribute to pulse broadening.

Additionally, QD lasers experience increased spatial hole burning (SpaHB) over QW devices from enhanced carrier confinement[103]. In semiconductor lasers, carrier-population oscillations are caused by standing wave patterns formed by different FP modes[109, 110, 111]. The carrier-density undulations cause oscillations in the gain, which is referred to as SpaHB, which destabilizes single-mode emission[112]. The changing carrier concentration also causes index gratings, through both the linewidth enhancement factor and the carrier plasma effect, which in combination with gain gratings leads to enhanced Four Wave Mixing (FWM)[110]. In QW devices, the gratings with small wavelength are washed out by the higher minority carrier diffusion lengths present[113], however QD lasers see an enhanced grating strength leading to larger FWM[114]. FM combs equally distribute power across the cavity, which alleviates the gain compression caused by SpaHB. Additionally, the colliding pulse cavity arrangement combined with linear frequency chirp generated in FM states causes the same wavelength light to cross in the SA, leading to enhanced bleaching. These factors form FM combs with a narrow beat note and quiet operation.

4.2 Device Design

The devices used in this study implement the shallow etch ridge-waveguide structure, which was discussed earlier in Section 2.3. An overview of the device design and structure is shown in Figure 4.1(a). The total cavity length is designed to be 1.37 mm, which produces a cavity FSR of 30 GHz. The device is a 2^{nd} harmonic CPMLL, with a single SA centered in the middle of the cavity, which creates a optical spectrum with 60 GHz spacing (additional details in Subsection 2.5.4). A short SA whose length is 7.8% of the total cavity length strikes a good balance between efficiency and performance. The SA of this device is created by etching a 500 nm deep isolation trench that is the width of the waveguide and 10 μm long. Figure 4.1(b) shows a cross-section Scanning Electron Microscope (SEM) image of a output facet of the device. Certain regions are shown in false color; the active region, shown in red, is below the termination point of the waveguide etch. The width of the shallow-etched ridge width is chosen to be 2.6 μm to improve WPE.

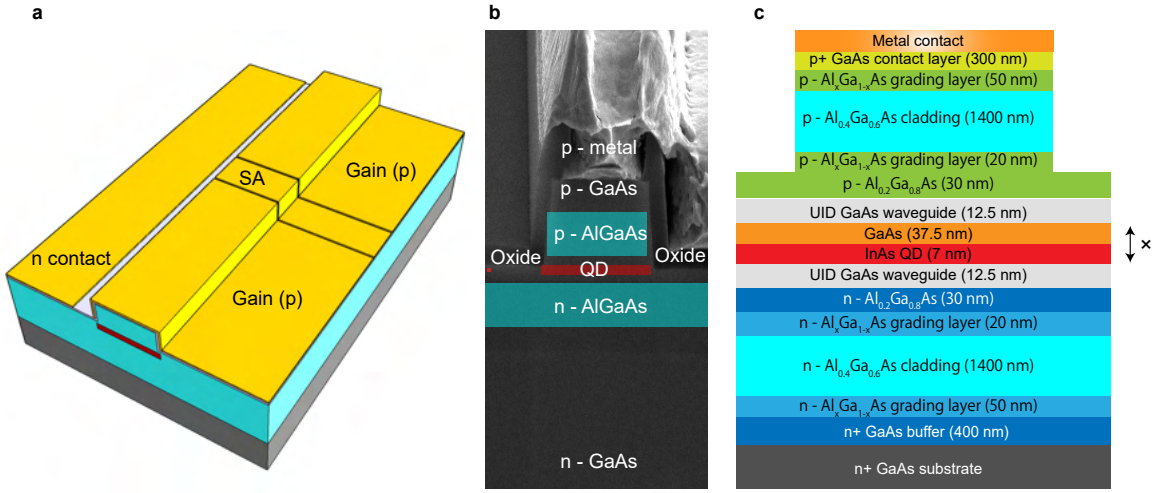

Figure 4.1: (a) Schematic of the InAs/GaAs CPMLL. The total cavity length is 3.7 mm, and the SA, whose length is 7.8% of the total cavity length, is placed at the center of the cavity. (b) Cross-section SEM image of the shallow-etched waveguide structure. Figure taken from [56]

Figure 4.2a shows the free-space characterization of the device. Both facets of the FP cavity are left as-cleaved, which gives equal output power from each facet and enables the most efficient comb dynamics. Because the formation of the AM/FM comb is dependent on the bias conditions of the gain and the SA sections, Figure 4.2a depicts the light-current (L-I) curves under different reverse biases on the SA. With the increase in SA reverse voltage from 0 to -6 V, the slight increase in the internal loss results in an increase in the threshold current from 15 to 21 mA along with a decrease in single-facet external efficiency η from 13% to 10.1%. The latter is calculated by $\eta = \frac{q\lambda}{hc}\frac{\Delta P}{\Delta I}$, with h the Planck constant, c the speed of light, q the electron charge, and λ the lasing wavelength. In all SA bias conditions, the QD laser studied exhibits a sufficient free-space output power over 15 mW and a peak WPE of 9% (single-side) (Figure 4.2b).

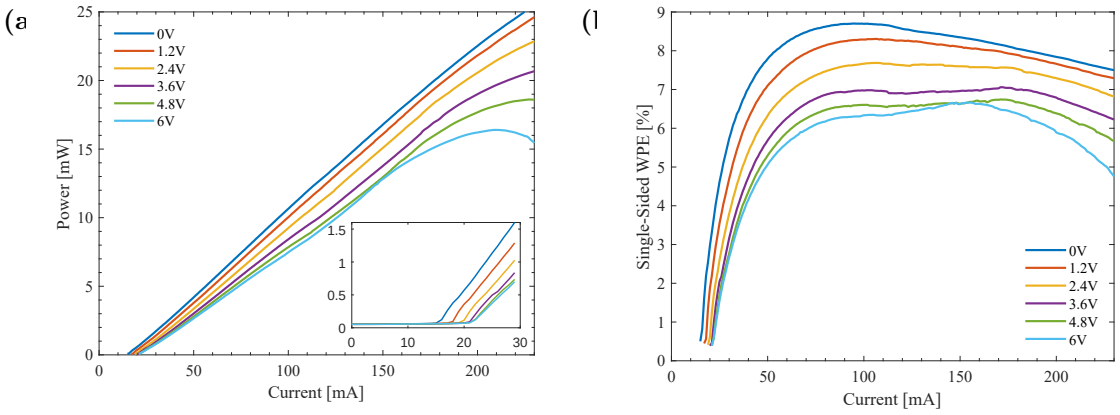

Figure 4.2: (a) LI curves of the QD laser under different SA reverse biases at 20° C. (b) Corresponding WPE curves calculated from the data in (a).

4.3 Inter-modal Phase Measurement

In general, the phase relationship between optical modes is important to characterize and difficult to measure. It is necessary for both the amplitude and the phase of each comb line to remain constant in order to have a periodic signal in time. The (optical)

spectral amplitude is extremely easy to measure, only requiring an OSA. However the phase of the optical carriers are difficult to measure because the laser can have phase drift from the various noise sources (particularly thermal drift on the order of msec, which is the time required to take ESA traces) and the frequency is extremely high, (229 THz for 1310 nm): PDs record only received power, not the electric field itself. However, optical heterodyne detection (Section 3.6) does recover the phase difference between the two frequencies. This can be leveraged to recover the phase difference between optical modes [115, 87, 116]. Two lines can be filtered out from the spectrum and analyzed with a oscilloscope, however the phase difference cannot be recovered directly, because it is arbitrary without a reference (the measured phase of the beat note is shifted with a time delay, and data acquisition cannot be synchronized to an optical carrier frequency). The laser can be electrically modulated[117], which allows synchronization with the RF source, but this also actively mode-locks the laser. The output light can be externally modulated but the oscillator must be synchronized to the free-running laser. This requires an external clock recovery signal to generate the synchronization signal, which is complex to implement. This optical heterodyne technique resolves the synchronization dilemma by using the fundamental beat note of the MLL as the phase reference.

Figure 4.3 shows the measurement setup for the experiment. The tunable laser source (TLS) is used as an optical local oscillator, which is positioned at a frequency between m^{th} and $m^{th}+1$ comb lines. The linewidth of the TLS is around 100 kHz, which is below the linewidth of the comb lines so it does not significantly impact the measurement resolution. The TLS is mixed with the two comb lines by simply using a fused fiber coupler and a 50 GHz PD; all fiber components are PM to ensure the beams are colinear at the detector. The resultant beat signals are amplified by a low noise amplifier before being mixed with an analog mixer with an electronic local oscillator. With thoughtful selection of the frequency of theTLS and the electronic local oscillator, the three necessary

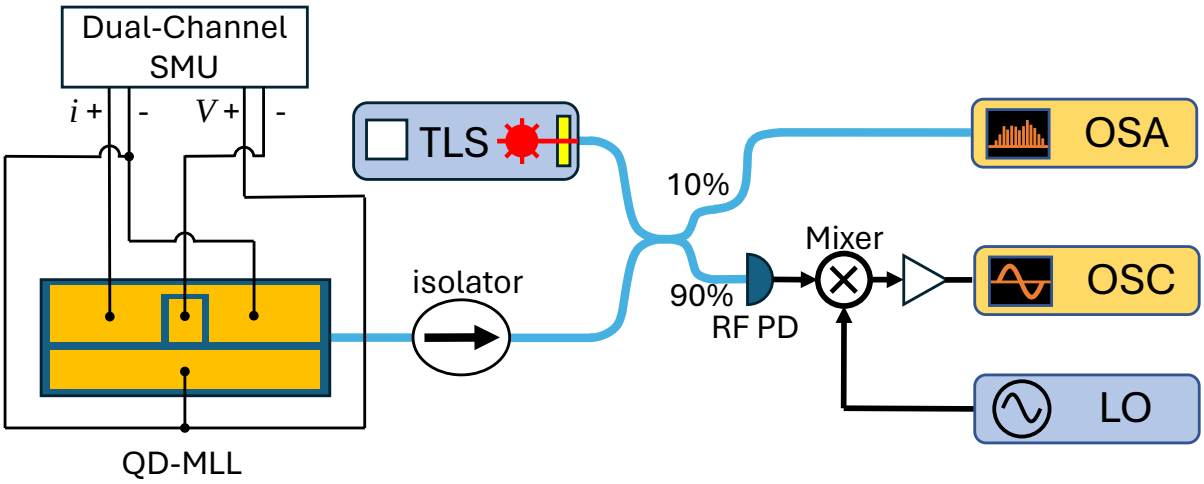

Figure 4.3: Schematic diagram of experimental setup used for inter-modal phase measurement. TLS: tunable laser source, OSA: optical spectrum analyzer, OSC: real-time oscilloscope, LO: local oscillator

beat notes can always be placed in the bandwidth of the real-time oscilloscope, and the measurement is only limited by the bandwidth of the PD and analog mixer. The data collected by the real-time oscilloscope is analyzed to find the intermodal phase difference between the two modes. The TLS is then stepped by the repetition rate of the MLL to determine the phase difference between the $m^{th}+1$ and $m^{th}+2$ comb lines.

4.3.1 Theory for Inter-modal Phase Extraction

The output of a MLL is a periodic signal, which means it can be described by summation of complex frequency components spaced by the repetition rate of the laser. In analogous to RF systems, these spectral components can be described as modulations on a high frequency signal carrier at ω_s. The electric field of the MLL, which was generally defined in Subsection 3.6.1 can be expressed more rigorously as

$$E_{sig}(t) = \sum_{m=-N}^{N} \left(\sqrt{P_m}\exp(jm\Omega t + j\phi_m)\right)\exp(j\omega_s t + j\phi_s(t)), \tag{4.1}$$

where P_m is the power of the m^{th} comb line, $2\pi/\Omega$ is the period of the signal, ϕ_m is the spectral phase of the m^{th} mode, ω_s is the average optical frequency of the signal, and $\phi_s(t)$ is the phase noise of the carrier. There is phase noise for each frequency component, however it is much smaller than the common-mode noise and can be ignored for this measurement[35] Similarly, the electric field of the optical local oscillator can be described with

$$E(t) = \sqrt{P_{LO}} \exp\left(i\omega_{LO}t + i\phi_{LO}(t)\right). \tag{4.2}$$

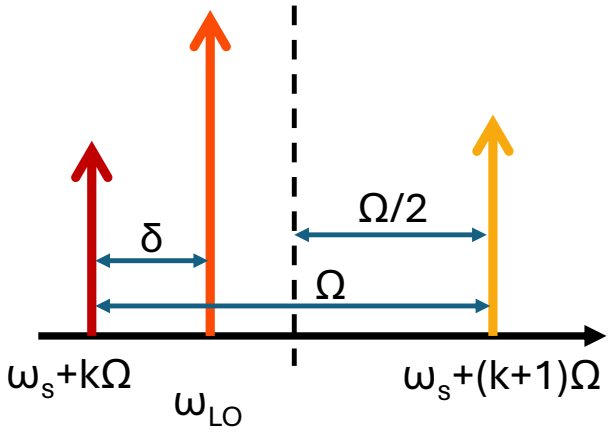

Figure 4.4: Diagram showing the placement of the TLS between the k^{th} and the k^{th+1} mode.

The heterodyne beat note signals are detected by the the PD, which has large enough bandwidth to detect all signals, including the fundamental beat note at 60 GHz. These are electrically mixed with an local oscillator at the frequency f, which gives a signal

given by

$$\begin{aligned} S(t) \propto & \sqrt{P_{LO}P_k}\cos\left(\delta t + \phi_{LO}(t) - \phi_s(t) - \phi_k\right) \\ & + \sqrt{P_{LO}P_{k+1}}\cos\left((\Omega - \delta - f)t - \phi_{LO}(t) + \phi_s(t) - \phi_f(t) + \phi_{k+1}\right) \\ & + \eta_m A_{fund}\cos\left((\Omega - f)t - \phi_f(t) + \phi_{fund}\right) + DC\ terms + higher\ order\ terms, \end{aligned} \tag{4.3}$$

where $\phi_f(t)$ is the phase noise of the electronic local oscillator, η_m is the efficiency of the mixer, and A_{fund} and ϕ_{fund} are the amplitude and phase of the fundamental beat note at Ω. The 90%/10% fiber splitter in Figure 4.3 is chosen to maximize the product $\sqrt{P_{LO}P_k}$ given that the power of the TLS is 10 dBm and a comb line is -5 dBm. The first three terms in Equation 4.3 are needed to find the intermodal phase difference; which is found by summing the phase arguments of the component at δ and $\Omega - \delta - f$ and subtracting this from the phase of the $\Omega - f$ component. In doing so the phase noise of the laser, TLS, and the electronic local oscillator all cancel out. The remaining terms are the intermodal phase difference, $\Delta\phi = \phi_{k+1} - \phi_k - \phi_{fund}$. This process determines $\Delta\phi$ between two modes up to a offset, ϕ_{fund}, which remains constant for each pair of modes considered in the spectrum. This term acts as an anchor for the intermodal phase difference, otherwise the phase difference of two frequency components varies with a time delay. This is analogous to the discussion earlier about clock synchronization; in this case, the difference $\Delta\phi$ for the k and $k+1$ mode-pair and the $k+1$ and $k+2$ mode-pair are synchronized with the fundamental beat note. This constant phase-offset, ϕ_{fund} equates to a time delay of ϕ_{fund}/Ω in Equation 4.1, and doesn't affect the temporal reconstruction of the signal, therefore, the average $\Delta\phi$ is subtracted when data is displayed.

4.3.2 Data Acquisition and Analysis

The phase arguments of each term in Equation 4.3 can be acquired by calculating the fast fourier transform (FFT) of the signal collected by the real-time oscilloscope. The signal from the PD is first amplified by a low-noise RF amplifier with a gain of 30 dB and a bandwidth of 18 GHz. The amplifier helps improve the fidelity of the measurement and overcome the mixer loss, which is around 10 dB. The device has a repetition rate of roughly 60 GHz and the frequency detuning of the TLS was chosen to be 10 GHz, which produces three beat signals at 10, 50 and 60 GHz. The frequency of the electronic local oscillator, f, is chosen to be 45 GHz, so that the down-converted signals $\Omega - f - \delta$ and $\Omega - f$ are at 5 and 15 GHz respectively. A small portion of the data collected by the real-time oscilloscope is shown in Figure 4.5; the interference of multiple signals can be clearly seen in the trace.

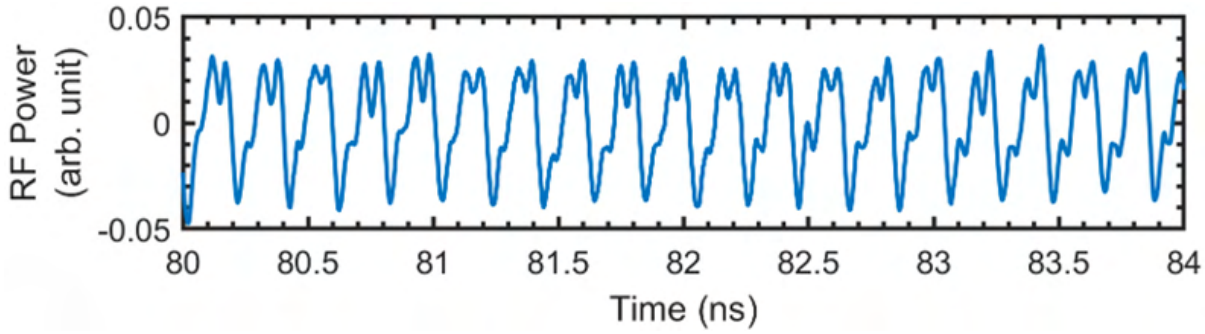

Figure 4.5: Small segment of raw data collected by the real-time oscilloscope of heterodyne signal of the TLS and hte MLL. Figure taken from [56]

The real-time oscilloscope used is capable of collecting 256 GSa/sec and data is typically collected for 2^{17} samples, which equates to 8.1 μsec of data collected. This strikes a good balance between brevity in the measurement duration and frequency resolution in the FFT. The duration of the measurement should be kept short primarily to avoid drift in the wavelength of both the MLL and the TLS. Additionally, the wavelength control circuit in the TLS periodically shifts the grating in the laser, which causes frequency

jumps in the output of the TLS. The data is collected in a continuous manner, and on short enough time scales, which is the main advantage to a real-time scope over a sampling scope. This allows for accurate phase measurement of the optical signals, and problematic data with frequency discontinuities can also be identified and removed.

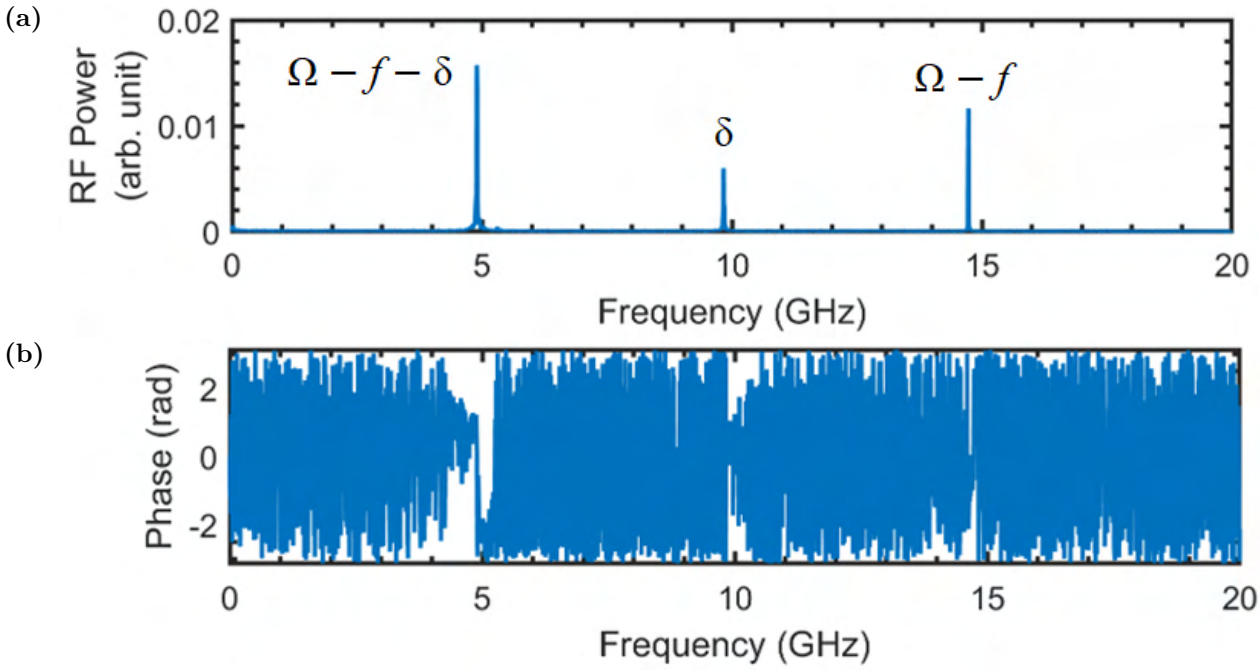

Figure 4.6: FFT amplitude (a) and phase (b) of the data shown in Figure 4.5. Figure taken from [56]

The data from the real-time scope is analyzed by applying a FFT to either the entire block of data or subsets of the data. The three beat signals are clearly identifiable in the amplitude of the FFT coefficients (Figure 4.6a). To check the quality of the data, the frequency of FFT component with the greatest amplitude at $\Omega - f - \delta$ and δ are summed and compared to the frequency of the peak component at $\Omega - f$. If they are equal, then the phasors for each FFT component are normalized and $\Delta\phi$ is calculated. If they are not equal, this is an indication that a frequency jump or large drift occurred at some point in the data. If this occurs, the data is divided by a factor of 2, and the process is carried out on all data tranches that meet the requirement. $\Delta\phi$ is calculated for each tranche and

averaged. The tranche-processing was performed on data that met the null-frequency-difference condition, and identical $\Delta\phi$ was calculated in both techniques. Additionally, a Hilbert transform can be used to extract the phase difference. This requires that the two signals at $\Omega - f - \delta$ and δ are mixed in the digital domain to produce a signal at $\Omega - f$, which is then filtered out with a raised cosine filter. This gives two signals at the same frequency, $\Omega - f$, and the phase difference is extracted with a Hilbert transform.

4.4 FM Comb Formation in QD-MLLs

Generating optical pulses is a sufficient but not necessary condition for mode locking; there are additional states of modal synchronization that can occur in MLLs. In a optical frequency comb, each pair of modes produces a beat note envelope in the electric field intensity; as was discussed in Subsection 3.6.1. This beat note has a frequency equal to the repetition frequency of the comb as well as an associated phase, which together can be considered an oscillator. Each pair of modes has a beat note, and they sum together to form the fundamental beat note; when the comb reaches a quiet operational condition each beat note has nearly identical frequency and this leads to a narrowing of the linewidth of the fundamental beat note. The individual modes of the laser are coupled together through a passive mode locking effect, gain dynamics and nonlinear effects inside the laser cavity, which couples the oscillators together that represent each beat note.

AM comb operation is produced by in-phase synchronization of the oscillators, which is equivalent to temporally aligning the beat note envelope of all mode pairs. This state is represented with the top array of metronomes in Figure 4.7, where each mode pair beat note occupies the same location on the unit circle. However, additional stable states of synchronization exist in coupled oscillators which are referred to as splayed-phase or

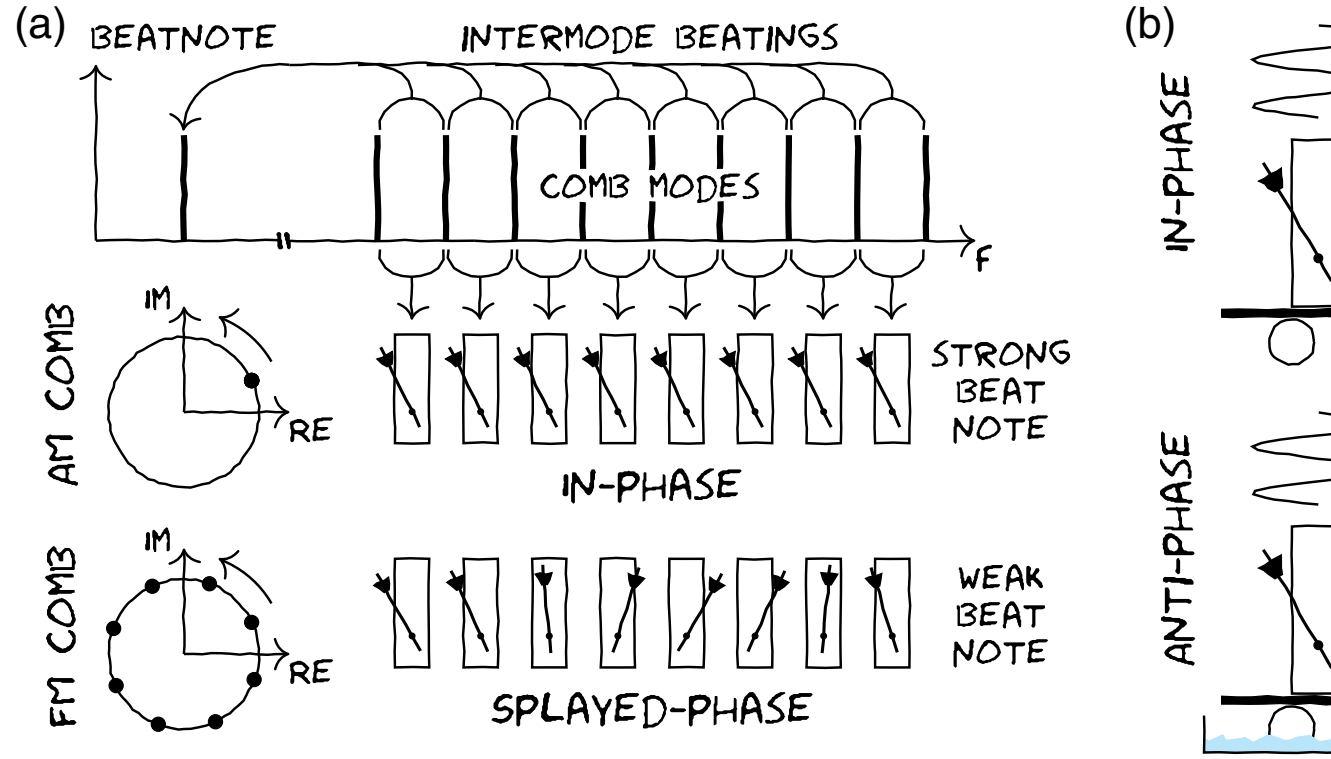

Figure 4.7: The fundamental beat note signal is produced from the combination of heterodyne beat notes from each pair of modes, which are coupled through interactions in the laser. The phase of each beat note is represented with a metronome and a point on the unit circle. In the case of AM combs, all beat notes are in phase with each other, which produces a strong amplitude modulation and beat note. Another synchronization state exists where the contribution of one beat note is canceled by another that is π out of phase, suppressing the beat note and amplitude modulation. Figure reproduced from [86].

anti-synchronization in synchronization theory[118], and is represented in the lower row of oscillators in Figure 4.7. This state consists of an ensemble of oscillators with their phases spaced equally across the unit circle. In this configuration, for any oscillator, there exists another oscillator that is π out of phase, mutually annihilating their contributions to amplitude modulations and the beat note. The unique gain properties of QDs make them well suited for generating both states of operation, which shows that two mode locking conditions are not mutually exclusive, and can be supported in the same device.

FIG. 1. (a) Different synchronization states of intermode beatings. Eve

These oscillators are coupled globally through their collective action—

synchronization states are observed. In an AM comb, they are synchronize

In an FM comb, the phases are splayed uniformly across the unit circle. He

annihilate each other. This suppresses amplitude modulations and the b

coupled metronomes on a movable platform. Metronomes positioned c

antiphase, depending on the damping. Such damping can be added by pla

AM and FM comb generation with semiconductor lasers. AM combs can

loss, while FM comb can even be realized in single-section lasers. There,

note similarly to the water bath in (b).

We show that this interpretation can be applied to semiconductor lasers. We demonstrate experimentally that both AM and FM comb states can be generated in the very same laser, while leaving the gain dynamics unchanged. Therefore, we can conclude that AM and FM comb generation in semiconductor lasers does not exclude each other.

the

0.2

gai

gai

tha

oth

tun

4.4.1 Intermodal Phase Analysis of FM Combs

The FM comb dynamics were investigated by using the stepped heterodyne method to measure intermodal phase in Section 4.3, and are summarized in Figure 4.8. Two states were chosen for illustrating the FM dynamics, which have identical gain current, 110 mA. The state in the left column is at 0.9 V and the state in the right column is 3.3 V. The optical spectra are shown in the first row, and the inset depicts the RF spectra with a Voigt lineshape fitted, as was detailed in Subsection 3.6.3. The second row shows the extracted intermodal phase, $\Delta\phi$ for the two states. Each state shows the fingerprint of FM combs, which is a linear distribution of intermodal phases over 2π, for the modes within the high-power flat-topped part of the optical spectrum, which is highlighted in blue. The autocorrelator traces obtained by intensity autocorrelation are then shown in the third row.

The two states together demonstrate that QD-MLLs have the ability to generate FM combs, and that the FM comb dynamics and importantly the bandwidth can be tuned simply by changing the SA bias. The state at lower SA bias, on the left, represents the regime of FM combs that are achieved more readily in the QD-MLL platform, even for non-optimized devices, and has a very flat optical spectrum, only 1.5 dB of power variation across the FM bandwidth. This is attributed to the long recovery time of the SA, which suppresses AM operation. This state has an $\eta_p = 0.13$, which is similar to values observed for CW operation, which also corresponds to a weak beat note signal of -70 dBm. When considering the oscillators discussed in the last section, this state had the phases of all oscillators spread uniformly over 2π and the amplitude of each oscillator identically matched. This leads to strong annihilation of the beat note signal, flat optical spectrum and flat AC trace.

When the SA bias is increased to 3.3 V, the FM operation is still maintained with

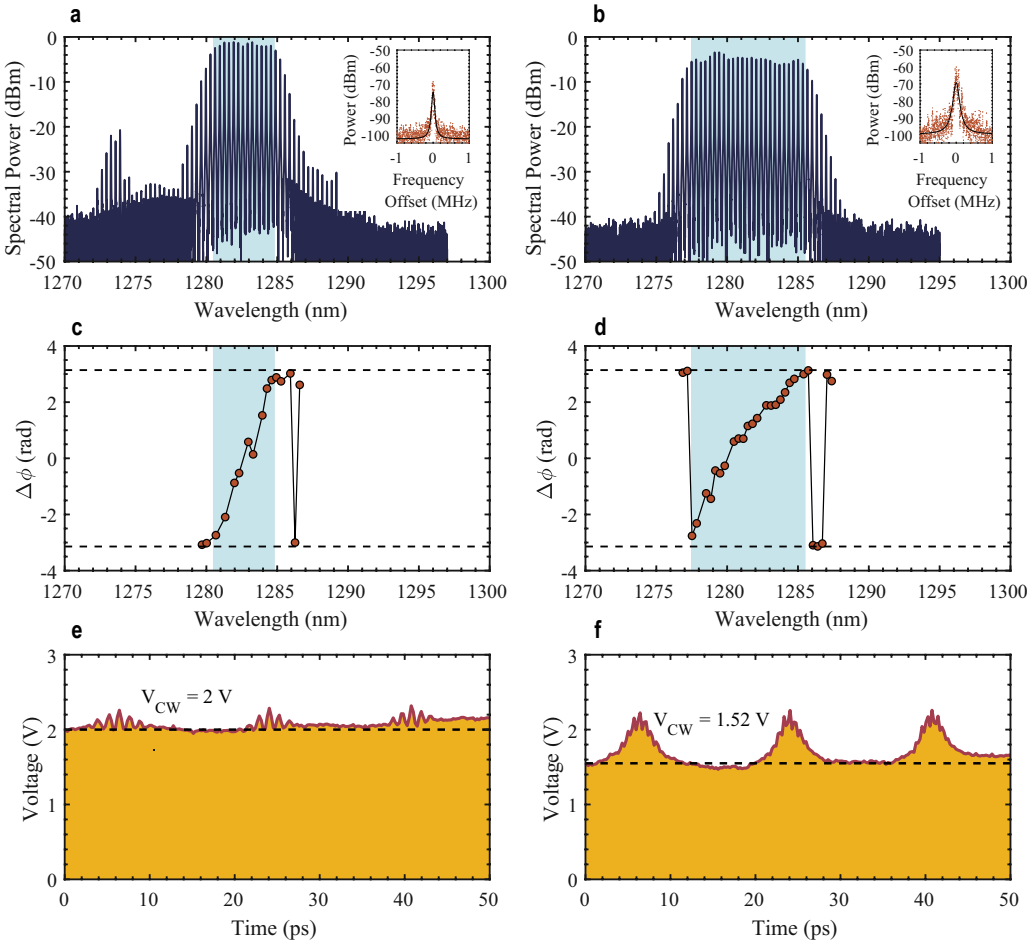

Figure 4.8: (c) and (d) show the measured intermodal phase of two FM comb states. Both states have the same gain current, and only the SA bias is changed from 0.9 to 3.3 V. (a) and (b) show the corresponding OSA trace, with the insets showing the narrow RF beatnotes. (e) and (f) show the corresponding AC traces with the CW levels marked with dashed lines.

an increased comb bandwidth. The 10-dB optical bandwidth is increased from 5.6 nm (1.02 THz) to 8.2 nm (1.49 THz). Additionally the linewidth of the beat note degrades slightly from 20 kHz to 40 kHz, which is attributed to the increased number of comb lines contributing to the beat note. In the 3.3 V state, the $\Delta\phi$ are also distributed over the range of 2π, but in a less uniform fashion; the slope of $\Delta\phi$ versus wavelength is not as constant. Additionally the power of all comb lines are not as equally matched; the power fluctuation across the comb increases to 3 dB. These two factors cause a less equal

annihilation of the contribution of each oscillator, which leads to larger AM ripples. This is directly seen in the AC trace with clear pulses present, and a $\eta_p = 0.34$. This also leads to an increased beat note, which shows a 10 dB increase in power. The useful tuning of FM comb states of QD-MLLs is discussed in more detail in Section 4.5.

4.4.2 Regimes of Operation

QD-MLLs are capable of creating both AM and FM combs in the same device, simple by changing the injection current of the gain section and the reverse bias of the SA section. This demonstrates that FM and AM operation are not mutually exclusive modes of operation in semiconductor lasers. The long upper state lifetime of interband lasers, which is on the order of nanoseconds, is much larger than the round trip time of the lasers, allowing for stable pulse propagation inside the cavity. Additionally, an intercavity saturable absorber with fast recovery time is achieved simply by reverse biasing part of the active region[119, 120]. However, quantum dots possess enhanced three-dimensional (3-D) carrier confinement over their QW counterparts[103], which enhances SpaHB leading to multimodal lasing[109, 113] and enhanced FWM[114]. Additionally the inhomogeneous broadening of the QD gain spectrum leads to large gain bandwidth[121], all of which leads to a broad optical spectrum with even power distribution.

The most definitive method of determining if the comb is FM or AM in nature is to measure the inter-modal phase (discussed previously in Section 4.3), but this is a very intricate and time consuming measurement, which cannot be carried out for all 984 possible gain current and SA bias combinations. However, the AC data, which is collected for every state, can be used to identify the different regimes of operation by extracting the pulse extinction ratio, η_p, which was defined in Subsection 3.7.1, but is

defined again for ease of reference. The pulse extinction ratio is expressed as follows:

$$\eta_p = 1 - \frac{V_{CW}}{V_p} \begin{cases} \geq 0.5 & \text{(AM domination)} \\ < 0.5 & \text{(FM domination)} \end{cases} \tag{4.4}$$

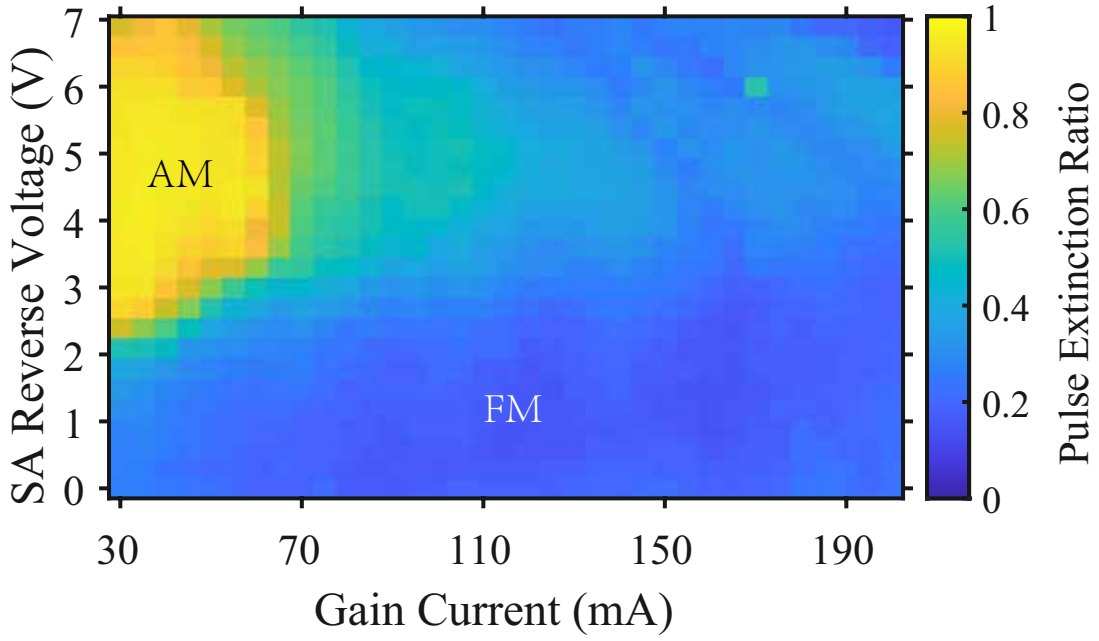

Figure 4.9: Pulse extinction ratio in the QD mode-locked laser. The formation of an AM comb requires that the gain recovery is slower than the SA recovery. The QD laser should operate with a low gain current and a high SA reverse bias to generate an AM comb. An increase in the gain current leads to the formation of an FM comb owing to the four-wave mixing. Figure taken from [56]

The ranges in Equation 4.4 are used to determine the boundary between state that are AM or FM operation. Figure 4.9 depicts the pulse extinction ratio of the QD-MLL shown in Figure 4.2, with the AM and FM operating conditions labeled. It should be noted that the definition of $\eta_p = 0.5$ is a rough estimation for the boundary of AM and FM operation. Pure AM state take place when η_p close to 1. It should be noted that $\eta_p = 0$ is not a necessary condition for an FM comb, because there is always power imbalance present between optical modes in the comb. This leads to an imbalance in the

annihilation of the amplitude modulation and the fundamental beat note. This allows the beat note to be detected with a fast PD and an ESA, even for FM states. In this work, we demonstrate that values near $\eta_p = 0.1\text{-}0.3$ produce an FM comb. Additionally, AM operation plays a dominant role in the laser's operation while $0.8 < \eta_p < 1$.

4.4.3 AM Mode Locking Regime

The two regimes of operation present in the laser will be discussed starting with AM operation. The area of AM operation occurs at lower gain bias conditions and higher SA reverse bias conditions. The recovery time of the SA exponentially decreases with reverse bias, from 62 psec to 700 fsec over 0-10 V range[83] as can be seen in Figure 4.10b. The recovery time is affected by the electric field and not the applied voltage, but their structure is similar to the one under consideration. At 4.5 V, the recovery time is approximately 16 psec, which is the equal to $\tau = 1/f_{rep}$. This allows the absorption of the SA to significantly recover between pulses. Additionally, the gain recovery time increases for lower injection current densities[28]. These conditions lead to a loss and gain profile similar to Figure 2.6b, where a periodic window in the net gain opens, producing stable pulsed operation. The increased SA reverse bias also changes the absorption spectrum, which is depicted in Figure 4.10. Primarily, there is a redshift in the absorption, due to the quantum confined Stark effect[120, 83]. The absorption peak also decreases in strength and broadens, however the peak tunes into the lasing bandwidth, yielding a net increase in modal loss with increasing reverse bias. Thus there generally exists a balance between decreased gain recovery time and increased internal loss in establishing the optimum AM mode locking.

The data collected was classified with the conditions in Equation 4.4 and states dominated by AM combs dynamics are summarized in Figure 4.11. The QD laser suffers from

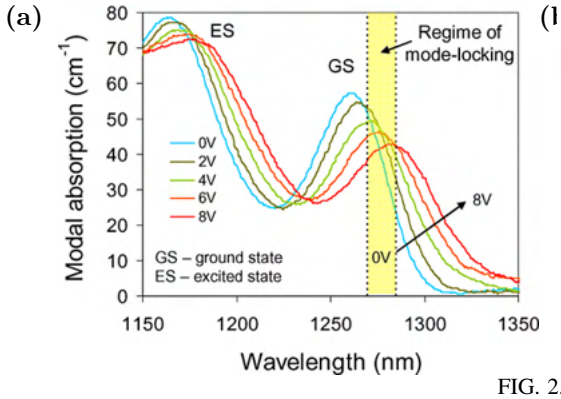

Figure 4.10: (a) displays the change in modal absorption in QD based SAs. Figure reproduced from [120]. (b) displays the change in absorption recovery time with applied reverse bias voltage. Figure reproduced from [83].

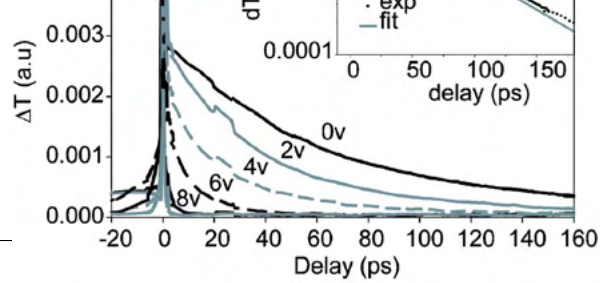

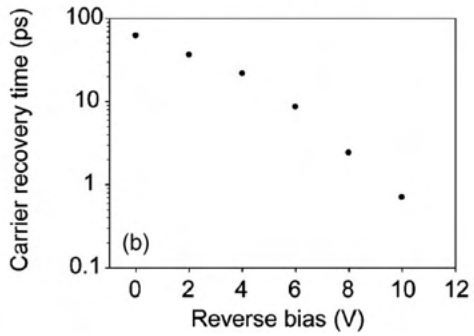

FIG. 2. Time resolved pump-probe traces for increasing reverse bias on the QD modal absorption (a). Single exponential fits used (inset). Absorption recovery times from exponential fitting (b).

a reduction in the comb bandwidth in AM operation due to the decrease in the SpaHB which drives multimode operation in QD lasers. Additionally the bandwidth is reduced by the bell-shape distribution in the optical spectrum, which is a result of the pulseshape in the time domain. An example of the AM comb is shown in Fig. 4.11(e), where the QD laser operates with 45 mA applied to the gain and -4.5 V applied to the SA. Corresponding intensity autocorrelation is shown in Figure 4.11(d). In the AM-dominant comb regime, the pulse width ranges from 1.7 to 3 ps by assuming a sech^2 shape, and the RF beatnote intensity is as large as -50 dBm.

As the gain current and SA bias increase, an unstable operating range is reached, where the SMSR decreases to nearly zero in Figure 4.11(a), but pulses are present in the AC. This is likely an AM region that is experiencing some mode instability. This may be caused by the higher pulse powers achieved in this region which saturates the gain and causes unstable operation. This effect limits the size of usable combs in the AM regime and is a drawback to operating in this area. Additionally, the combs generated are not flat-topped, which is not ideal for DWDM applications.

(~300 K V/cm). The measured traces are shown in Fig. 2(a). The pump pulse energy employed was 580 fJ, causing absorption saturation through band filling and giving rise to the steplike increase in probe transmission. Interestingly, we see no evidence of field screening effects in the leading edge of the traces,[11] which leads us to believe that any such effect is minimal due to the low number of carriers generated in the dots. At zero delay, the observed spike can be attributed to the interference between the overlapping probe pulses and the leaked TE component of the pump pulses.

With increasing probe delay, the transmission decays as photogenerated electrons and holes either escape or recombine. We found that the measured absorption recoveries fit best to a single exponential of the type $\exp(-t/\tau)$ in a simple rate equation model, where τ is the recovery time [inset Fig. 2(a)]. As depicted in Fig. 2(b), the recovery time decreases by almost two orders of magnitude from 62 ps to 700 fs as the reverse applied voltage varies from 0 to 10 V. These results suggest that the dynamic response of our device is limited by carrier escape only, in contrast to measurements reported in other QD structures with no applied bias.[12]

Figure 3 shows the measured absorption recovery rates Γ ($=1/\tau$) as a function of applied reverse voltage. These rates can be expressed as the sum of contributions from recombination (Γ_{rec}), thermionic emission (Γ_{th}), and tunneling (Γ_{tun}) mechanisms given by

$$\Gamma = \Gamma_{rec} + \Gamma_{th} + \Gamma_{tun}. \quad (1)$$

The short recovery time (62 ps) measured at zero applied field, suggests that the contribution of recombination processes is not significant at room temperature (consistent with nanosecond recombination times as previously reported[13]).

The effect of an applied reverse field is threefold. Firstly, this causes a lowering of the barrier height by $\Delta E = E_{b0} - E_b = q\beta|F|/2$, where a is the dot height and q is the electron

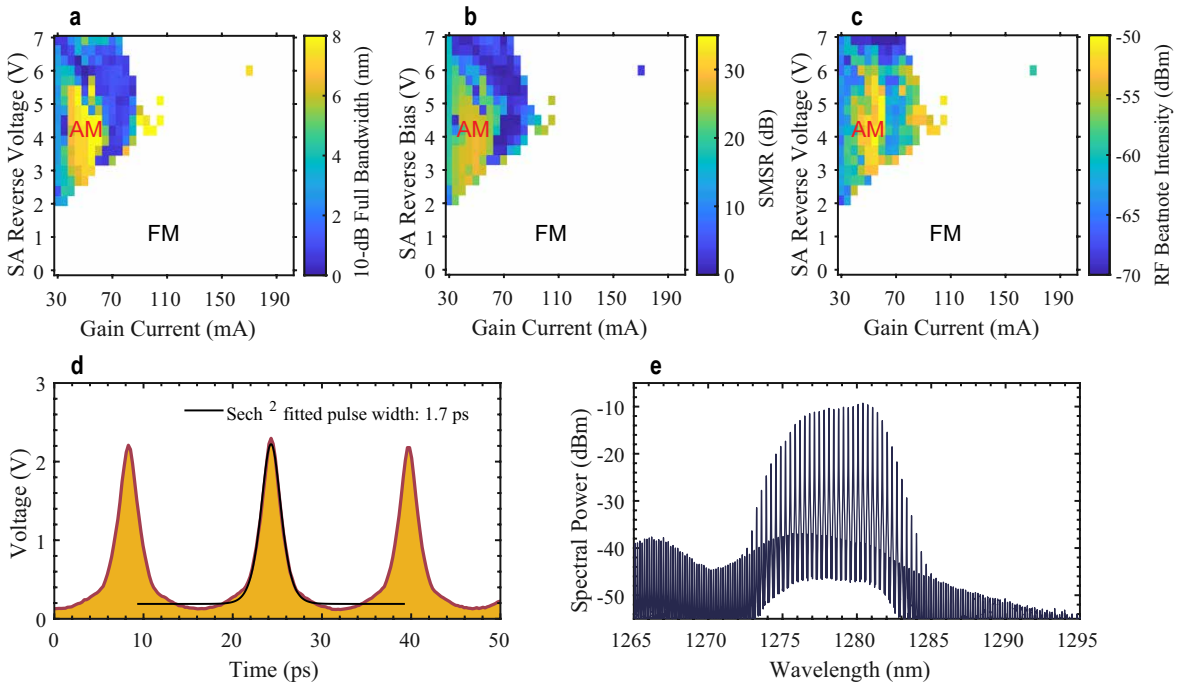

Figure 4.11: (a) Mapping of the 10-dB optical bandwidth under different biases on the gain and the SA. (b) Mapping of the average side-mode-suppression-ratio (SMSR) among the central 20 comb lines under different biases on the gain and the SA. (c) Mapping of the RF beatnote intensity under different biases on the gain and the SA. AM, amplitude-modulated dominant operation; FM, frequency-modulated dominant operation. (d) Intensity autocorrelation of an AM comb state. (e) Optical spectrum of an AM comb state. The gain current is 45 mA and the SA reverse voltage is -4.5 V. Figure taken from [56]

4.4.4 FM Mode Locking Regime

This section explores the states characterized by FM operation. The devices in this study primarily exhibit FM operation, as demonstrated in Figure 4.12 and Figure 4.13, which has the AM data removed. The pulse extinction ratio is effective at identifying AM states, however the autocorrelator alone cannot distinguish between a CW state and a FM state which has a quasi-CW output; both produce a flat AC trace. CW states produce a coherence spike only at zero time delay. FM states, however, generated a series of coherence spikes spaced by τ, because the coherent comb repeats itself after one period. An example of a FM autocorrelator can be seen in Figure 4.8, where the coherence spikes

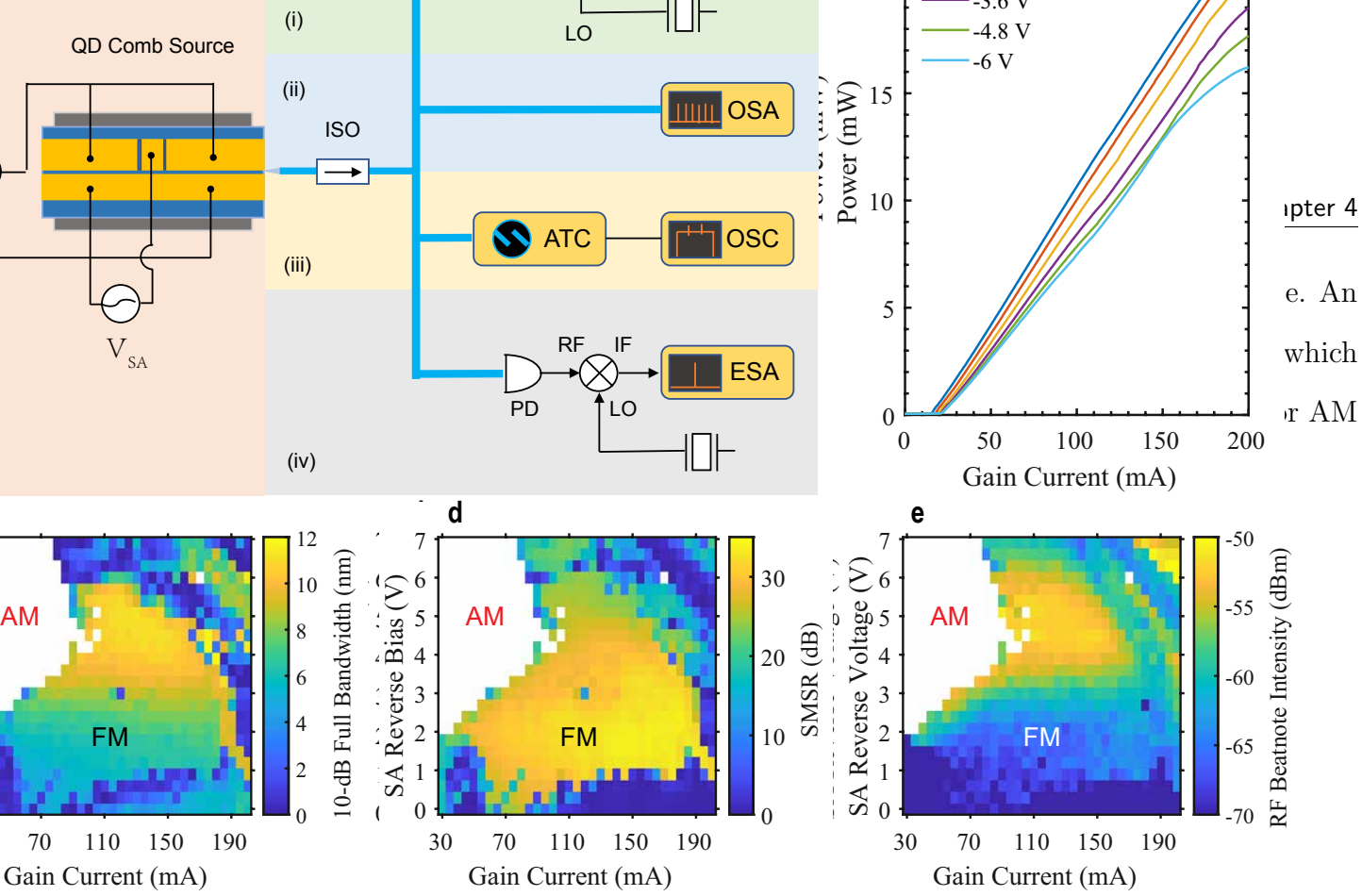

Figure 4.12: (a) depicts the SMSR of the FM states. (b) illustrates the change in the beat note intensity of FM states

The FM operation is most easily achieved with low SA bias, starting near threshold and extending through the entire gain current range, however it also occurs at higher SA biases for a more limited current range. The area in Figure 4.12a with SMSR greater than 20 dB are FM comb states, and the highest SMSR is achieved in the 0-2 V SA bias range. In the low SA bias range of 0-2 V, the recovery of the SA is much slower than the repetition period of the signal[83], which leads to the SA being continually saturated. This causes there to be a nearly constant cavity loss profile in time, which suppresses AM operation. This particular device does not show FM operation from 0-0.7 V, but it can be achieved, such as the device shown in Figure 3.4.

The low SA bias range also shows the narrowest beat note linewidth and the lowest beat note intensity, which is a signature of FM comb formation. This behavior is shown in Figure 4.13a, however the trends in linewidth are not completely illuminated because the Keithley SMU limits the narrowest measurable linewidth to about 100 kHz. The

linewidth of two states are measured with a low noise current source and shown in Figure 4.8. The state in the left column is made with a 0.9 V SA bias and has a linewidth below 20 kHz, while the state in right column has the same gain current and a 3.3 V bias and possesses a 40 kHz linewidth. The trend in beat note intensity is clearer in Figure 4.12b, increasing with higher SA bias, which was discussed previously.

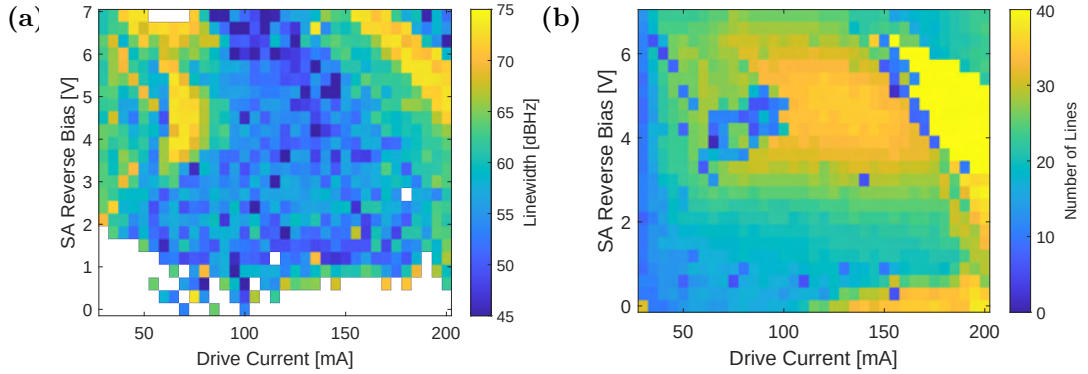

Figure 4.13: (a) Linewidth of the beat note for all states. The FM states have the narrowest beat note. (b) 10 dB optical bandwidth of the comb for all states.

However, for higher SA biases, the FM operation is infringed at both lower and higher gain bias with different modes of operation, which shows up as a triangular area of FM operation in Figure 4.12a. Considering a cut across the states at 4.5 V, the different regimes can be seen. At lower gain currents, the operation is AM as previously discussed in Subsection 4.4.3. As the gain current increases, the bandwidth of the comb increases, as can be seen in Figure 4.12b until about 60 mA. Here the optical bandwidth is too broad to sustain AM operation from chirp in the pulse. The extracted pulsewidth is shown in Figure 4.14, and there is a clear increase in pulsewidth which is accompanied by a very broad beat note linewidth (Figure 4.13) and low SMSR(Figure 4.11b). This is an area of unstable mode-locking, caused by a lack of SA recovery and high inter-cavity power.

For gain currents above 100 mA, the device switches to FM operation. In this region high comb bandwidths are achieved, as can be seen in the plot of 10 dB bandwidth

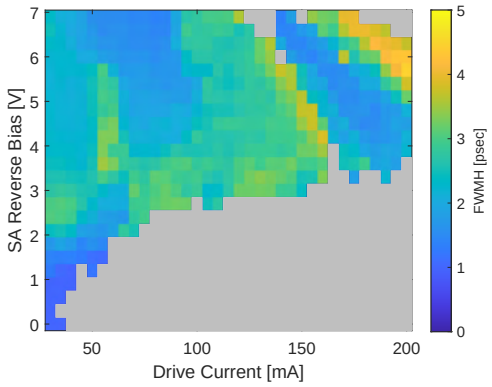

Figure 4.14: Extracted pulsewidth of states with a $\eta_p > 0.15$. States with low η_p are shown in light gray, because they cannot be accurately fitted.

in Figure 4.13b. This area achieves greater than 35 comb lines (11.8 nm) in the 10 dB bandwidth. This area was confirmed to be FM operation as was shown for the state at 110 mA and 3.3 V in Figure 4.8d. In the region of FM operation the bandwidth is relatively constant with gain current, and is mainly controlled with the SA bias; increasing bias increases the comb bandwidth. The operation eventually becomes unstable for large gain current and large SA biases around 170 mA. Above this current the bandwidth becomes larger but the beat note linewidth increases to greater than 1 MHz (Figure 4.13a), and the SMSR drops below 20 dB. There is also a clear increase in the pulsewidth at this transition from FM to unstable mode locking. Further increasing the gain current causes completely unstable operation, with SMSR near zero and linewidth above 10 MHz.

4.5 Dispersion and Kerr Nonlinearity in FM combs

A unique and counter-intuitive property of FM comb formation in QD-MLLs is that the bandwidth is independent of changing the gain current, in contrast to FP QD lasers, where optical bandwidth increases with pump current. In AM combs, dispersion is an unwanted parameter normally compensated for; however, interestingly, dispersion is necessary for FM combs to form. In FM combs, the bandwidth is not governed by the gain

bandwidth of the material. Instead, the FM bandwidth is mainly governed by a balance of SpaHB, dispersion, and the Kerr nonlinearity induced by the gain[122], which is well described by the model in [123]. This model was used to simulate FM comb formation in a QCL laser. Figure 4.15a shows $\Delta\phi$ of the FM comb formed for five different values of cavity group velocity dispersion (GVD)[123]. There is a minimum required GVD necessary for FM comb formation; below which the bandwidth of the comb is greater than the material gain and unstable CW operation occurs. As the GVD increases, the slope of the intermodal phase, which is directly related to instantaneous frequency chip of the comb, increases and the bandwidth decrease. In AM comb operation, GVD negatively impacts pulsewidth, however nonzero GVD is necessary for FM comb formation, which helps define the comb bandwidth necessary to span 2π intermodal phase distribution, which creates the FM-comb state.

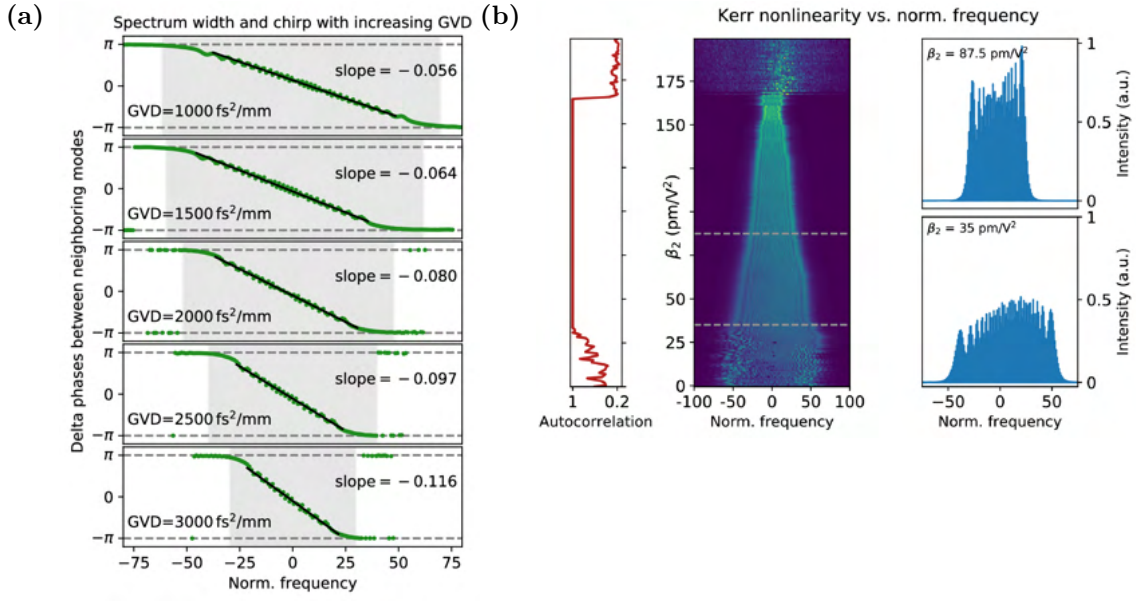

Figure 4.15: (a) depicts the change in intermodal phase slope and comb bandwidth caused by changing the cavity dispersion, which also results in a change in FM comb bandwidth. (b) depicts the change in the FM comb bandwidth with a change in the gain-induced Kerr effect, β_2. The Autocorrelation shows the degree of comb temporal coherence. Figures taken from [123] and [124] respectively.

It has also understood that nonlinear optical properties play an important role in the cross-coupling of optical modes in a laser cavity[125, 126]. The affect of the Kerr nonlinearity was also modeled in [124] and are shown in Figure 4.15b, where the dispersion of the cavity is assumed to be zero. The optical spectrum of the device was calculated for different values of the gain induced Kerr nonlinearity, β_2, and shown in the waterfall plot in the center of Figure 4.15a. The autocorrelation on the left is calculated by comparing the temporal intensity of one round trip with itself after 500 round trips. With low β_2, a chaotic CW operation with low autocorrelation is achieved because the required FM bandwidth is broader than the gain bandwidth. The threshold for FM formation is around $\beta_2 = 35pm/V^2$, at which the maximum comb bandwidth is achieved. As β_2 increases, the maximum bandwidth of the comb decreases, corresponding to a steeper slope in the plot of $\Delta\phi$ versus wavelength, similar to the affects of increasing GVD in Figure 4.15a. The two dashed yellow lines show the position of the two spectra on the right in the waterfall plot showing a decrease in bandwidth with increasing β_2.

4.5.1 Dispersion and Linewidth Enhancement Factor in QD-MLLs

The FM comb bandwidth is determined by the interplay of the GVD and Kerr nonlinearity present inside the cavity. As was previously motivated, the cavity dispersion is necessary for FM comb formation and is important to characterize for the laser in this study. For high Q ring-resonators, several techniques have been employed to measure the dispersion, mostly by sweeping an ECL laser and measuring the transmission signal with a synchronized PD. The wavelength of the ECL is calibrated with an unbalanced MZI or a fiber comb laser with 40 MHz FSR to resolve the exact position of the resonances[127]. These types of techniques excel at sharp resonances, but don't facilitate more accurate

resolution in the low-Q resonators created by FP lasers, particularly because the resonance is broad, making it hard to identify the exact resonance position in the presence of noise.

To overcome this, a novel method of measuring GVD was implemented in this study[56], which is depicted in Figure 4.16 a. The amplified spontaneous emission (ASE) emission of the SOA provides a ripple-free light-source, which propagates through the unpumped, cold-cavity of the laser. In order to avoid the large interband absorption of the active region, the SOA center wavelength was chosen to be 1320 nm, with a 40 nm bandwith. An FP laser of the same length and ridge width was used in the dispersion measurement. The transmission spectrum of the ASE is collected with an OSA, and the data is smoothed before the resonance locations are determined. The normalized group delay is proportional to the first derivative of resonance position with respect to ω, so the derivative is averaged over multiple resonances to improve accuracy. The measured normalized group delay is shown with blue dots in Figure 4.16 b. The data is fit with a linear curve, shown with a blue line. The derivative of the best fit line is proportional to GVD, which was calculated to be 1200 fs^2/mm. The dispersion of the laser was simulated in a model that takes into account both material and geometric dispersion, the results of which are shown with the red curve of GVD on Figure 4.16 b. In the lasing range of the QD-MLL, the simulated value of GVD ranges from 1164 to 1257 fs^2/mm, with an average of 1210 fs^2/mm, which is in good agreement with the measured value. The laser operates from 1280-1310 nm across 20-80°C temperature operating range at maximum, in which the simulated GVD changes marginally from 1210 to 1320 fs^2/mm. Thus the GVD does not change considerably or effect FM-comb formation over the operating regime.

The increased bandwidth seen from increasing the SA bias in Figure 4.13b and Figure 4.8 is attributed to increased Kerr nonlinearity. In III-V lasers, the real part of the refractive index is linked to the imaginary part of the index, through a relation called the

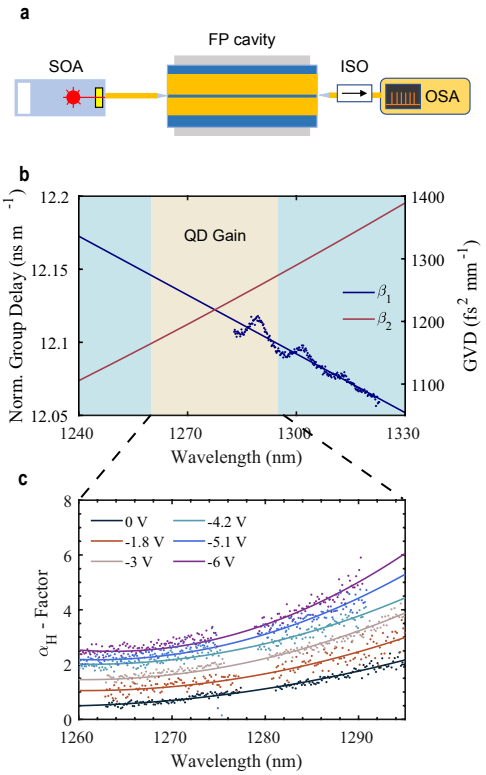

Figure 4.16: (a) depicts the setup used to measure the dispersion of QD lasers. SOA: semiconductor optical amplifier, FP: Fabry-Perot, ISO: isolator, OSA: optical spectrum analyzer (b) measured normalized group delay shown with blue points with linear line of best fit shown in blue. Simulated GVD shown in red. (c) measured α_H-factor versus wavelength from the QD-MLL for different SA biases.

linewidth enhancement factor (LEF), denoted by α_H. Both the real and imaginary part of the index vary with carrier concentration in the active region, therefore, it is useful to express the LEF as[128]:

$$\alpha_H = -2\frac{\omega}{c}\frac{dn/dN}{dg/dN} = -\frac{4\pi}{\lambda}\frac{dn/dN}{dg/dN} \tag{4.5}$$

where N the carrier density injected into the active region, λ is the lasing wavelength, dn/dN the differential refractive index, and dg/dN the differential gain. The α_H-factor quantifies the change in the real part of the refractive index caused by the change the gain or the imaginary part of the index. The standing-wave patterns in FP cavities

that form population undulations, which lead to SpaHB, also cause a modulation in the index through the α_H[110]. Because the differential gain is very closely linked to intercavity light intensity in III-V lasers, the index change produced by α_H is intensity dependent. By definition, the Kerr nonlinearity is a change in index of refraction with light intensity. Thus, this effect is termed the gain-induced Kerr nonlinearity, β_2[122]. The crystalline Kerr effect in III-V semiconductors is relatively small, however fast gain material, particularly QCLs, show a large gain-induced β_2. Nevertheless, it should be noted that the Kerr effect is much weaker in lasers with a slow gain medium, such as QW lasers, due to the decreased SpaHB[129].

QD lasers can possess a significant gain-induced Kerr nonlinearity due to their fast gain medium[28] and enhanced SpaHB from greater carrier confinement[103]. However, QD lasers can have exceptionally low α_H[130], which is a desirable property in many applications[131, 132], but diminishes the gain-induced Kerr effect. Recently, it was demonstrated that the α_H-factor of QD-MLLs substantially increases with applied SA reverse voltage [133, 134], where a similar device was shown to increase its α_H from 2 to 12 when the SA was swept from 0 to 5 V in [134]. This illustrates that the Kerr nonlinearity in QD-MLLs can be tuned by adjusting the SA bias and the α_H-factor.

Figure 4.16c depicts the spectrally resolved α_H-factor for varying SA biases measured at threshold for the QD-MLL used in this study. Around the gain peak, the α_H-factor increases from 1 to 3.1 when the reverse bias of the SA is increased from 0 to 6 V. This is less variation than the samples in [134] where the lasers had roughly twice as much p-doping in the active region as the samples in this study. As was shown in [134], the affect is mainly due to the increase in the numerator of Equation 4.5, which is the carrier-induced refractive index change. The denominator, which is the differential gain, does also decrease slightly. The ASE method is used to extract the sub-threshold differential gain and α_H-factor from the ASE[135]. The change in wavelength of an individual mode

is tracked above and below threshold with optical spectra to eliminate the thermally induced changes and determine carrier-induced index change[134, 56]. The data around the peak of the gain region is missing because this region experiences strong intermodal perturbations from SpaHB[129, 103], preventing accurate measurement of the α_H-factor in this region. Importantly, the slope of the α_H-factor versus frequency $\mathrm{d}\alpha_H(\omega)/\mathrm{d}\omega$, determines the sign of β_2 [136], which is negative for the QD comb laser studied. With a positive GVD and a negative Kerr nonlinearity, an increasing α_H leads to an larger magnitude β_2, which compensates the cavity dispersion, leading to broader FM comb bandwidth[56]. This aspect allows the comb bandwidth to be tuned by a factor of 2x by changing the SA bias.

4.6 Conclusion

In this chapter, the comb dynamics of a 60 GHz QD-MLL were investigated. The design of the device utilized a shallow-etched design, which greatly improved the performance of the device, enabling efficient FM formation over an extremely large range. A method for investigating the intermodal phase, refered to as the stepped heterodyne technique, was thoroughly explained in Section 4.3. The method involves using a ECL laser to create two distinct beat notes, from which the the intermodal phase is recovered. The mathematical model used in the method and the data analysis techniques were detailed.

The stepped heterodyne technique was used to analyze the phase relationship present in the laser used in this study. It was shown that the laser produced the splayed-phase state, proving that the comb dynamics are in fact FM in nature. The intermodal phase was measured for two states with different bandwidth and both states were found to be FM combs, with the bandwidth increasing by 50% in the comb state with higher SA bias.

The device in this chapter was shown to achieve both AM and FM comb operation, and each regime was investigated in detail. The FM region was demonstrated to maintain constant bandwidth with increasing gain current, a striking difference from QD-based FP lasers; instead the comb bandwidth is completely controlled by the SA bias.

Lastly, the dependence of comb bandwidth on cavity GVD and the gain-induced Kerr nonlinearity was discussed. First modeling analysis of FM comb dynamics in QCLs was depicted to illustrate the role that both the dispersion and the Kerr nonlinearity play in FM comb formation. The necessity of cavity dispersion for FM comb formation was shown. The origin of a intensity dependent index perturbation, termed the gain-induced Kerr nonlinearity, was explained and the role that this has in FM comb bandwidth was discussed. The cavity GVD was measured with a novel method and the measured GVD was found to be in good agreement with a thorough dispersion model. The LEF factor was also measured over a large wavelength range, and for a range of SA biases. LEF was shown to increase with increasing SA bias, which increases the strength of the Kerr nonlinearity. This effect is attributed to the tunable bandwidth observed in QD-MLL in this study.

Chapter 5

Effect of P-doping in the Active Region on Comb Efficiency

5.1 Introduction

QDs offer an exciting alternative to QW lasers for a multitude of reasons. They were theorized to offer temperature insensitive operation due to the atom-like density of states[27], assuming that energy separation between ground state (GS) and excited state (ES) was much larger than kT at room temperature. However, as is the case for most III/V materials combinations, in the InAs/GaAs materials system used for QD lasers, the valence band offset is much smaller than the conduction band offset, leading to a smaller confinement energy barrier for holes. This allows holes to have a high rate of thermal-escape out of the ground state of QDs[137], which leads to decreased gain with increasing temperature.

III-V materials suffer from the effective mass of holes being much larger than the effective mass of electrons. This in general leads to a slower filling of the available valence band states versus the conduction band states under uniform injection, leading

to less quasi-Fermi level displacement in the valence band and non-ideal hole occupation in the ground state and lower optical gain[138]. This was mitigated in QW lasers with strain engineering, by breaking the light hole and heavy hole degeneracy. However, strain is already a growth condition optimized in DWELL growth structure, and is not a free parameter to adjust. Additionally, the larger effective mass leads to closer energy spacing in the bond states of holes in the QD. The larger effective mass combined with the smaller valence band offset leads to an energy level spacing in the valence band of 10 meV, which is smaller than the value of kT at room temperature, 25 meV.

Adding additional holes into the active region from p-type doping has been studied both theoretically [139, 137, 140, 138] and experimentally[139, 141, 142] to alleviate the issues outlined above. This is done by inserting a thin p-modulation doped (pMD) GaAs layer near a DWELL structure[142], to avoid acceptors in the area of radiative recombination. Using pMD layers has enabled lasers with large T_0[143] compared to QW devices in the 1.3μm range. pMD has enabled regions of infinite T_0[144] and even CW-lasing up to 220°C[145]. This is accomplished by increasing the saturated modal gain per QD layer by increasing the quasi-Fermi-level separation[138, 139] and also by reducing thermal depopulation of the GS in the valence band[137].

An agreement on the optimum pMD level has not been reached in the community. In general, the p-doping is measured in reference to the number of holes divided by the number of QDs referred to as holes per QD (HPD), which links dot density to the thickness or doping concentration of the pMD layer. This makes comparisons between reports difficult, because dot densities vary, QD structures are not consistent (i.e. different DWELL structures or QDs embedded in GaAs). Initial reports stated very high HPD levels of 52[142], 15[146], and 18[144]. Later, studies lowering the level to 10[147].

The benefits of pMD in QD lasers does saturate at a given point, and eventually leads to decreased performance. In an investigation involving a first principles simulation

combined with experimental data, saturation was attributed to increased scattering and enhanced nonradiative recombination[139], and Auger recombination was identified as the predominant source in [138, 148, 149]. Free-carrier absorption[150] and inter-valence band absorption[144] have been discussed as sources of increased loss, and nonuniform injection of electrons from a shifted depletion region[151] have also been discussed as a mechanism that leads to decreased performance. Regardless of the cause, pMD doping in the active region leads to increased room-temperature threshold[141]. The WPE of a laser is acutely sensitive to the threshold, which merits the optimization of pMD levels.

5.2 Challenges of Studying Active Region p-Doping

Studying and comparing the effects of pMD can be challenging because other factors can conflate the results of varied pMD. The SK growth mode used for quantum dots is inherently very sensitive to growth-conditions[46, 47]. In particular, dot density is affected by small variations in growth temperature and the indium growth rate[48]. The dot density in QD lasers correlates directly with the saturated modal gain of the laser[152], and higher saturated modal gain results in increased maximum lasing temperature[153]. Additionally, altering the dot density changes the HPD for a given pMD layer. This leads to potential confounding effects from increasing the pMD and decreased dot density and vice versa. Additionally, fabrication issues in laser processing can detrimentally affect laser performance, which further complicates the study. Slight changes in processing such as different etch stop positions and ruff mesa hardmask patterning can negatively impact injection efficiency and internal loss, which both lead to worse high temperature performance.

There have been several studies on the optimum doping in QD FP-lasers[141, 150, 144], however, there have been no studies on optimizing pMD in QD-MLLs. Additionally,

room temperature performance, particularly threshold, is sacrificed in pMD lasers for higher T_0 and T_1 values. However, determining the optimum doping to yield the highest efficiency at a elevated temperature, such at 60°C, requires intricate analysis. The goal of the following study is to investigate the role that pMD plays in comb formation at elevated temperatures, and particularly, how doping effects the efficiency of generating individual comb lines at elevated temperatures.

5.2.1 Active Region Doping

5.2.2 Devices for studying doping

The effects of pMD in the active region were studied with a series of different wafers grown for laser fabrication. Four samples were grown by MBE, all with an identical laser structure, which is shown on the left of Figure 5.1. More details on the MBE growth of the standard 40% AlGaAs laser structure can be found in Section 2.2. All layers in the four samples are identical except for the 37.5 nm GaAs spacer layer between QD layers. The pMD layer is inserted roughly 15 nm above the preceding QD layer. To adjust the number of acceptors, only the thickness of the pMD layer was changed, and the doping was held constant at 5×10^{17} cm^{-3}. The samples have approximately 5×10^{10} cm^{-2} areal dot density, which was confirmed with atomic force microscope (AFM) of surface dots on test samples grown under the same conditions. This gives the four samples a HPD level of 0, 2.5, 5 ,and 7.5 from right to left. All samples have six QD layers, except the UID sample, which has five QD layers for legacy reasons, because all previous QD-MLL samples made at UCSB had five layers [23, 93, 154].

All four samples were processed in a manner to limit the effects on laser performance from variations in the growth and fabrication. All samples were grown in the same MBE in order to minimize the variations inherent between different systems arising from dif-

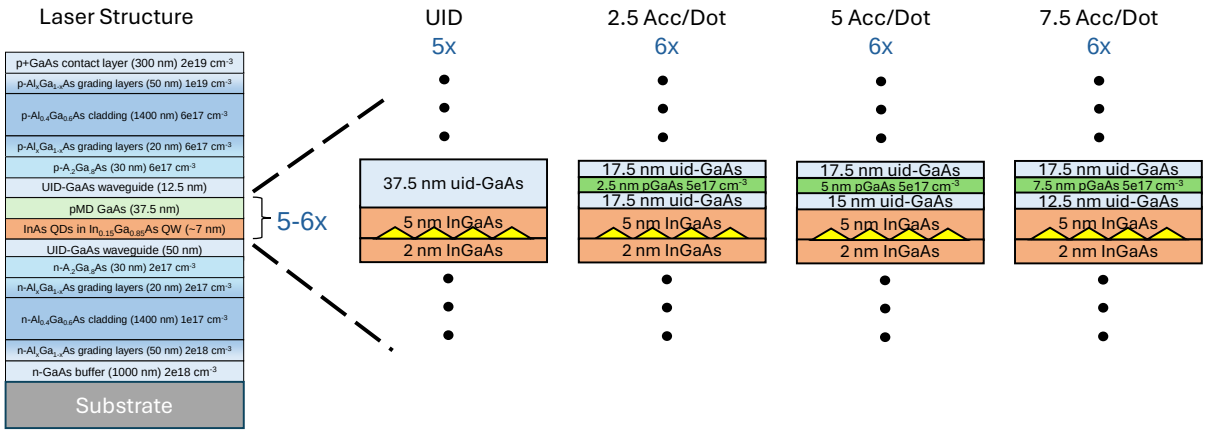

Figure 5.1: Devices used in the pMD study. All devices have identical structure except for the thickness of the pMD layer. Samples from right to left have 0, 2.5, 5, and 7.5 HPD

ferent calibrations. The samples with 5 and 7.5 HPD were grown within a 10 day period. The samples with 0 (UID), 5, and 7.5 HPD were coprocessed in the same fabrication run, to share as many of the fabrication steps as possible. The metal depositions, passivization layers and via opening were done simultaneously. The dry etching of the waveguide was done independently, to ensure the etch was stopped at the correct height above the active region. The 2.5 HPD sample was coprocessed with 0 and 5 HPD samples in a separate run. The 0 and 5 HPD samples show similar performance between the two runs, confirming that the fabrication between all four samples is comparable.

5.2.3 Device Design

The devices in this study are identical in design the laser used in Chapter 4, which was 2^{nd} harmonic CPMLL with roughly a 60 GHz repetition rate and a 30 GHz cavity FSR with a 1.37 mm length. An in depth discussion of the fabrication process was discussed in Section 2.3, which describes microfabrication steps used in making the lasers. Figure 5.2a shows the location where the etch is terminated to form the shallow-etched waveguides and Figure 5.2b shows the a cross-section SEM of the fabricated lasers used in the study.

The waveguide etch was terminated 200 nm above the active region by laser-etch monitor. The active region, which is mainly composed of GaAs spacer layers, has a slightly different contrast than the AlGaAs in SEM, but it is hard to distinguish. Dashed lines are added in Fi lGaAs cladding

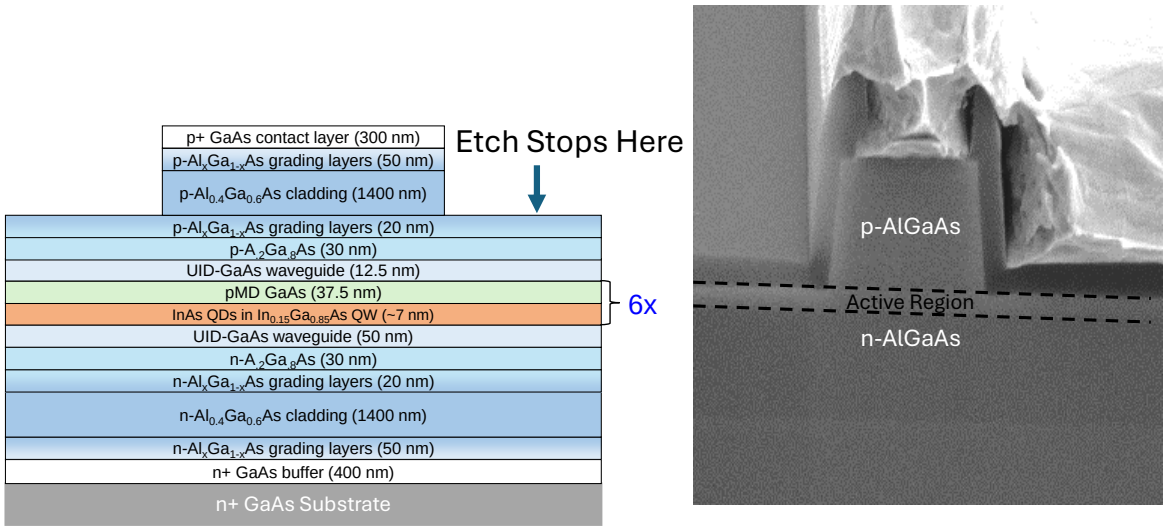

Figure 5.2: (a) depicts a schematic of the epi-stack used for the lasers in this study. (b) illustrates the shallow-etch waveguide profile used for this study. The etch is terminated just above the active region.

5.3 LI and WPE Performance

To understand the role that pMD plays in comb efficiency at elevated temperatures, the free-space LI performance of the four lasers under study is first considered. The comb efficiency of a single line cannot exceed the net WPE efficiency of the laser itself, which is heavily affected by the SA. Figure 5.3 illustrates the effect that SA bias has on WPE; as the SA reverse bias is increased, the efficiency of the laser decreases. This problem is marginal at 20°C, in both UID and pMD devices. The free-space, double-sided WPE of the UID and 5 HPD devices at 20°C (5.3a and 5.3c) both show a small decrease of about

1 dB in the WPE when the SA is biased at 2 V versus floating. This is one aspect that allows similar performance between UID and pMD devices when considering only 20 °C.

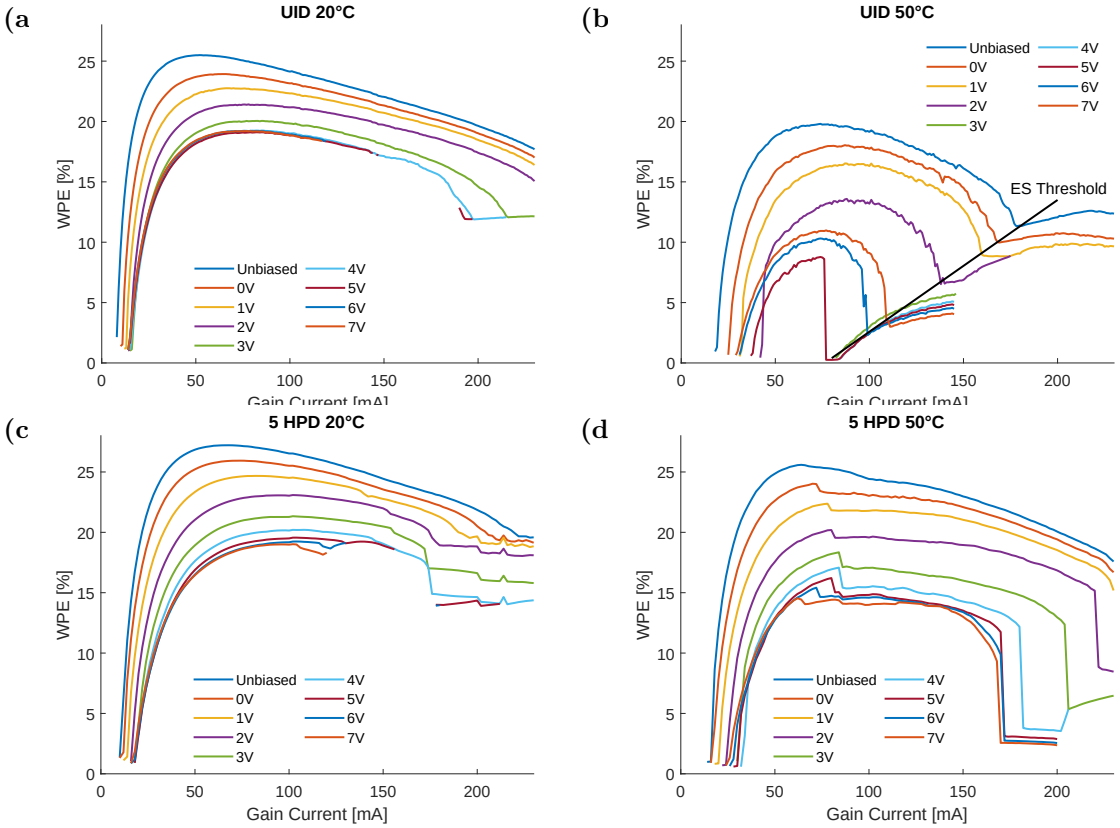

Figure 5.3: Figures (a) and (b) show the WPE of the UID MLL at 20 and 50°C for varying SA biases, while Figures (c) and (d) show the same information for the 5 HPD MLL

When examining the WPE performance at an elevated temperature such as 50°C, the difference in performance between the UID and pMD devices is much clearer. The WPE of the UID MLL now decreases by more than 2 dB at 2 V from its unbiased efficiency. Additionally, the onset of ES lasing limits the current range over which the device can operate at 2 V bias. The transition, which is marked with a black line in Figure 5.3b, causes a dip in the WPE and mixed GS-ES occurs to the right. This effect is is also seen in the 5 HPD at 50°C, but only at very high gain currents or high SA biases, because pMD delays the onset of ES lasing[150]. Additionally, the 5 HPD device has a performance

that is nearly identical to the 20°C performance, with only a 0.73 dB decrease in the peak WPE from 20 to 50°C at 2V, with a nearly identical gain-current operation window. This shows the importance of having pMD incorporated into the active region of the laser to retain the room temperature performance at elevated temperatures.

5.3.1 Comparing LI and WPE performance versus doping

The LI and WPE performance of all devices is compared over the temperature range of 20-80C, as is shown in Figure 5.4 and Figure 5.5. The first figure compares the LI performance of the four devices used in this study. 5.4a shows the performance of the devices when the SA is left floating. In this condition, the SA is easily bleached, so their performance is similar to FP lasers. The top row shows performance at 20°C. The four devices show similar LI curves, with the UID device showing the lowest threshold. The UID device and the 2.5 HPD device also experience the most thermal rollover, because they are more sensitive to self-heating. In 5.4b, the LI performance at a SA bias of 2 V is compared. The 20°C performance in 5.4b does not show significant changes to 5.4b.

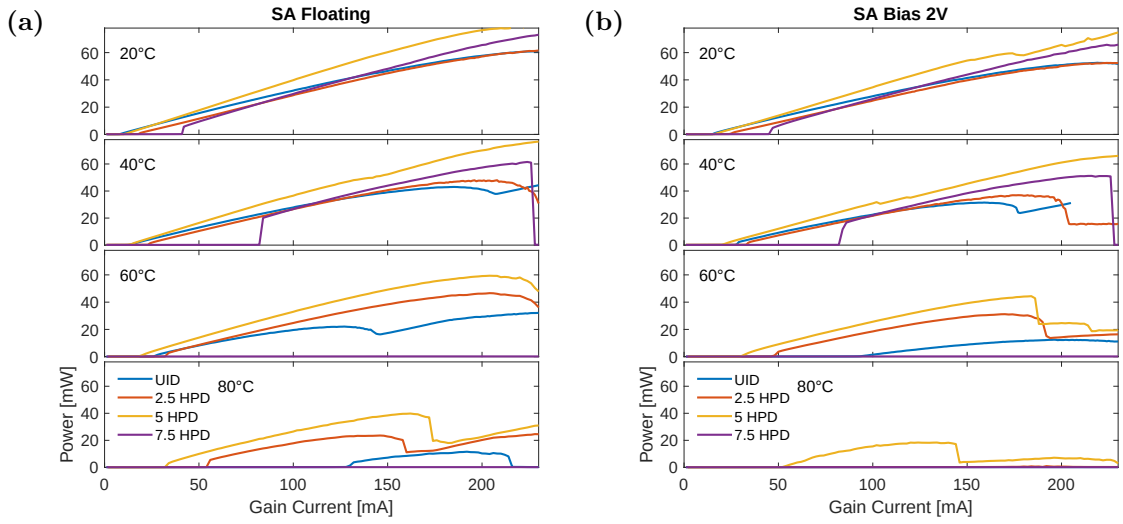

Figure 5.4: (a) shows the LI performance for devices with the SA unbiased for 0 (UID), 2.5, 5, and 7.5 HPD. Data for 2 V reverse biased SA is shown in (b). Data is shown for 20, 40, 60, and 80°C

As the temperature increases, the device with the highest output power for both the 5.4a and 5.4b is the 5 HPD. The 2.5 HPD device is close in performance, however it experiences thermal rollover sooner and it cannot sustain lasing at 80°C and 2 V. At 60°C, the UID device shows 20 mW of output power at 100 mA while the SA is floating, but at 2 V, it experiences mixed GS-ES lasing. ES lasing makes the MLL output unusable for many reasons, most importantly because the increased absorption causes current densities in the SA large enough to permanently damage it.

Increased doping does offer higher gain[138], however the LI data suggests that the 7.5 HPD device has too much internal loss. This can be seen with the large q-switch step at threshold from bleaching the SA, which increases with temperature, showing the increased internal loss present in the SA that must be bleached in order to lase. The internal loss from p-doping, particularly from increased Auger recombination, increases with temperature. This causes the 7.5 HPD to suffer from worse performance than the 5 HPD device at elevated temperatures, leading to it not reaching lasing for 80°C.

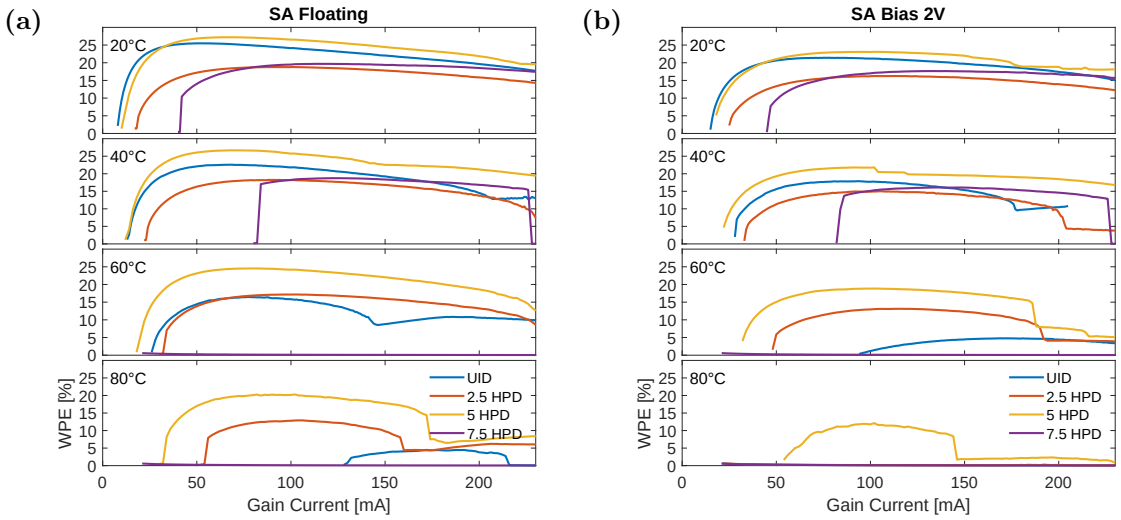

Figure 5.5: (a) shows the WPE for devices with the SA unbiased for 0 (UID), 2.5, 5, and 7.5 HPD. Data for 2 V reverse biased SA is shown in (b). Data is shown for 20, 40, 60, and 80°C

The WPE follows similar trends to the LI performance, which is shown in Figure 5.5.

The 7.5 HPD device does show the smallest degradation in WPE, however it starts as the least efficient device and it cannot reach a point where it outperforms the devices before it cannot sustain lasing at elevated temperatures. The UID and 2.5 HPD device have good performance at 20°C, but slowly degrade in performance. The 5 HPD device consistently has the highest WPE out of the devices considered for both the unbiased and 2 V bias cases, showing that it is the optimum balance between the increased gain and loss from pMD doping.

5.4 UID Comb Efficiency versus Temperature

The QD MLLs in this study were designed to be multiwavelength sources for DWDM applications. The energy efficiency of devices are of particular importance for this application, so the efficiency performance of the four devices is compared. The efficiency of generating the 20^{th} comb line, WPE20, is the benchmark metric for comparing the performance between devices. Thus the comb performance of the devices are analyzed in the manner outlined in Subsection 3.5.4. Small efficiency differences between different devices are more easily shown in the linear scale, so the WPE/C of the devices are compared.

All four devices have efficient performance at 20°C and the UID device has the highest WPE/C achieved in the study at 9.3%. The performance in Figure 5.4b and Figure 5.5b shows that the UID and 5 HPD have the highest WPE at 20°C, which is an indicator of generating an efficient 20-λ comb. The 2-D color-coded plot of the WPE/C (Figure 5.6a) and the SMSR (Figure 5.6b) show a large area of efficient operation for the UID device at 20°C. This MLL achieves a a peak WPE/C value of 9.3% at 95 mA and 1.8 V, which is close to the location of the peak free-space WPE of 21.4% at 75 mA in Figure 5.6b, The UID MLL generates an efficient comb over the large current range of 70 to 230 mA at

1.8 V SA bias, with a slight decrease in efficiency with increasing current, which mirrors the WPE curve in Figure 5.6b. High WPE/C requires large SMSR, and the device produces a large area of high SMSR states within which all the high efficiency states are contained. The SMSR is calculated in the method described in Subsection 3.5.1. Several key metrics of performance are extracted from this data, and shown in Figure 5.9, and will be discussed later.

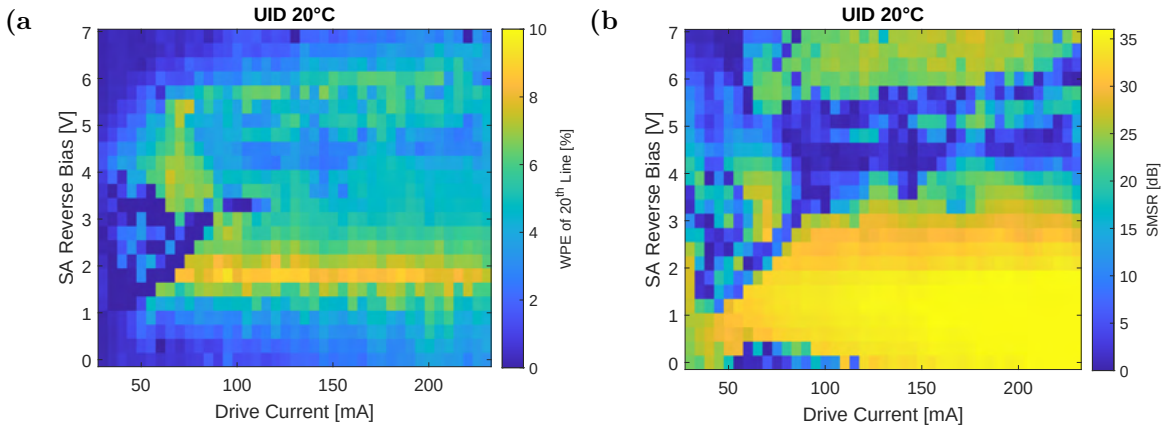

Figure 5.6: (a) shows the WPE/C and (b) shows the SMSR of the UID CPMLL at 20°C.

As the temperature increases, the performance of the UID MLL degrades. At 40°C, the device has similar performance as at 20°C, but there is a noticeable decrease in the peak WPE/C, which decreases to 8.4% and the current range of efficient states, which decreases to 75-200 mA (Figure 5.7a). The change in area of states with high SMSR can be seen in 5.7b. The reduction comes mainly from the loss of states around 3 V SA bias. The horizontal range of high SMSR states around 1.8 V SA bias decreases slightly. These changes are somewhat hard to identify just by looking at the 2-D color-coded plots, but can be clearly seen in Figure 5.9. To prevent damage to the SA, the grayed-out portion in upper left corner of the plots in Figure 5.7 were not tested because of excessive SA current, from the onset of ES lasing.

Examining the 60°C comb performance, a dramatic reduction in performance is ap-

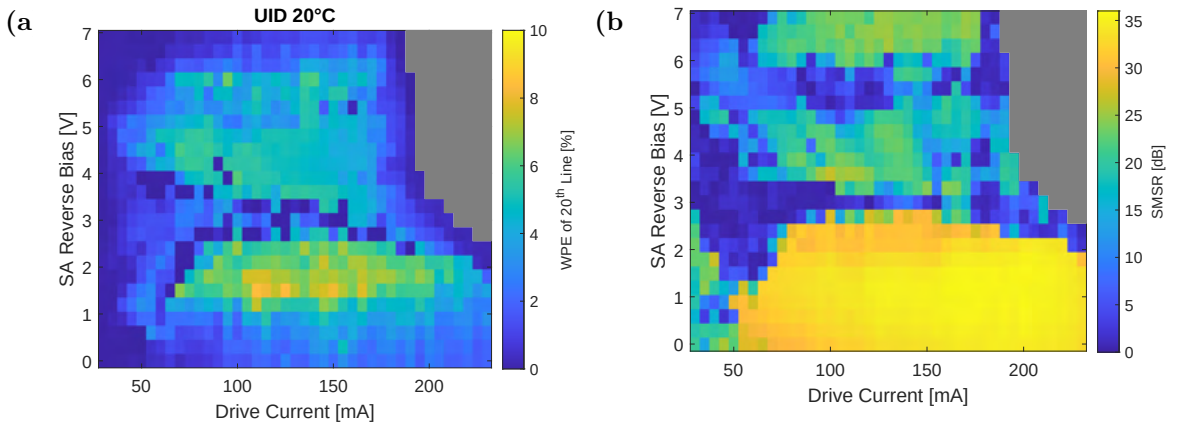

Figure 5.7: (a) shows the WPE/C and (b) shows the SMSR of the UID CPMLL at 40°C. Grayed-out region in the upper right corner was not tested due to high SA photocurrent.

parent, which echoes the trends seen in the LI performance in Figure 5.4. The peak WPE/C falls to 3.2% and the range of operation is dramatically reduced. At this elevated temperature, ES emission, both subthreshold and above threshold, causes poor comb performance. The range of low SMSR seen in Figure 5.8b above 1.2 V at 100 mA is an area of operation where subthreshold ASE emission at the ES wavelength causes unlocked operation. For higher gain currents or SA bias, the increased carrier concentration required to sustain lasing leads to the GS-ES lasing. This regime is marked on Figure 5.8b with the light gray area, and causes poor comb performance. The effects of ES radiation, severely limits the operation of UID MLLs at elevated temperatures, motivating the need for p-doping in the active region.

The color coded plots in 5.6, 5.7, and 5.8 are very illustrative, however synthesizing the performance into several key metrics can help interpreting the data. Five key metrics can be tracked to help identify the quality of operation over temperature range of operation, which are shown in Figure 5.9, each of which has its own y-axis on the left. In blue, the number of states with SMSR>25 dB are listed, with total possible number of states being 984. This parameter shows a linear decline after 30°C, showing the reducing area of

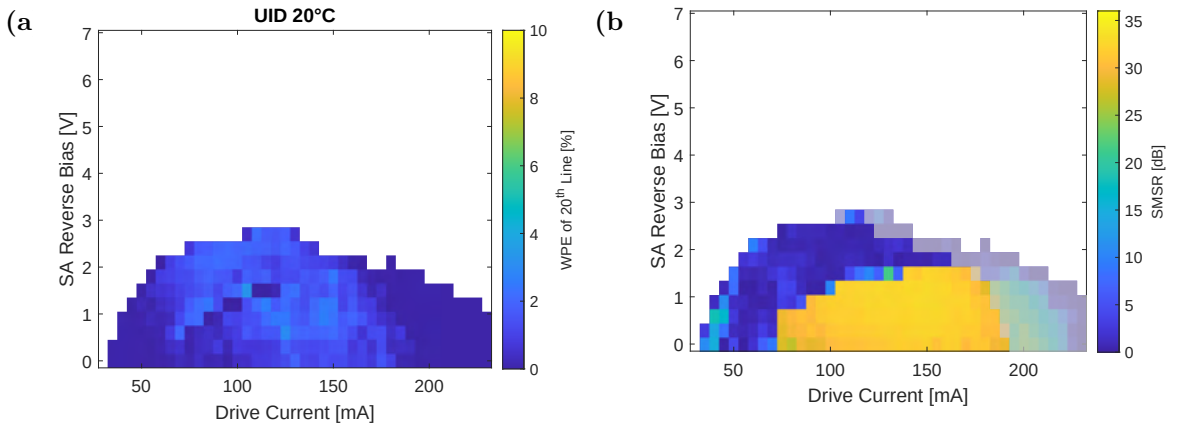

Figure 5.8: (a) shows the WPE/C and (b) shows the SMSR of the UID CPMLL at 60°C.The light-shaded area in (b) denotes states where GS-ES lasing is occurring

mode-locking with increasing temperature. The second metric is the maximum WPE/C achieved in the scan, which takes a 1 dB decrease after 20°C, then dramatically decreases after 50°C. The third metric is highest single-sided power measured for the 20^{th} comb line, which was defined as PoLL in Subsection 3.5.3. This shows a steady decrease with power, tracking the first metric. The fourth parameter is defined as the number of states within 1 dB of the max WPE/C measured for the temperature and device under consideration. This is useful for measuring the area of efficient operation, along with the last metric. The increase at 30 °C is due to the most efficient SA bias lying between 1.8 and 1.5 V, which roughly doubles the number from 20 °C. The last metric is the range of current over which the high efficiency states from the last parameter occurs. This metric is a very strong indicator of the efficient operating range of the MLL. All five metrics show a strong decrease in magnitude with temperature, particularly those that measure the range of operation. The WPE/C does remain surprisingly high until 60 °C. This shows that QD-MLLs have the ability to maintain an optimum bandwidth for a 20-λ comb despite temperature induced changes in laser parameters such as threshold. The strong decline in all of these parameters with increasing temperature shows the need for p-doping to improve high temperature performance.

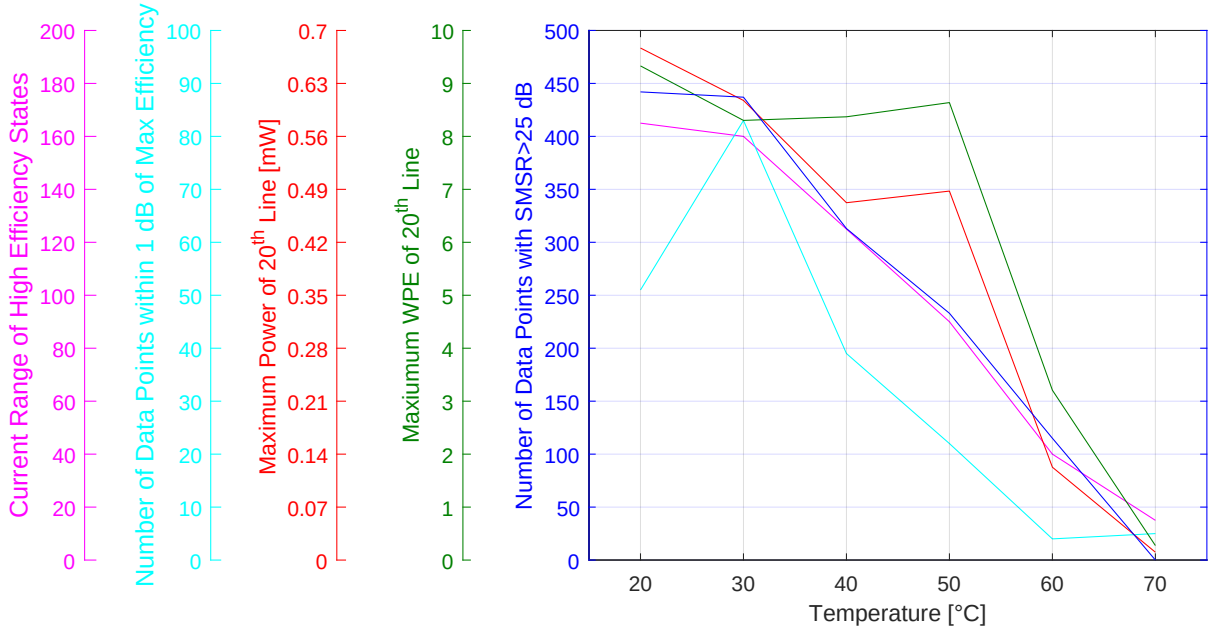

Figure 5.9: sdf

5.5 Comparison of Temperature Performance for Different Doping Levels

The lasing performance of UID MLL was shown in the last section to be very sensitive to increased stage temperature. Figure Figure 5.9 displays two different trends in temperature degradation. The area of high quality mode locking begins shrinking linearly from 30 °C, and the efficiency and comb power steeply decline after 50°C. The benefits of P-doping to improve temperature performance were discussed in Subsection 5.3.1, but free-space WPE is not a direct indicator of WPE/C performance. All devices in the study were measured in the method described in Section 3.4. In order to compare the performance of different devices, the key metrics in Figure 5.9 will be compared individually for the four devices.

The SMSR is a direct indicator of comb performance, which makes it useful for gauging the area of comb operation in a device. Figure 5.10 shows the number of states

out of the 984 possible with SMSR greater than 25 dB for the temperature range tested. All devices produce a large area of operation and therefore have a large area of operation at 20 °C, except the the 5 HPD sample. All devices show a degradation in the area of operation with increasing temperature. The UID device shows the earliest decline in area, which is to be expected. Interestingly the 7.5 HPD sample has the second earliest temperature induced decline, which is attributed the the higher internal loss in the device. This illustrates that the optimal p-doping in a QD-MLL is less than that typically required in a FP or DFB laser, likely because the SA is an additional source of loss. The 2.5 and 5 HPD have the best performance versus temperature, with the 5 HPD device have the most gradual degradation and the highest number of states at 80 °C. The UID and 7.5 HPD devices do not have data at 80 °C because they do not lase. The 5 HPD sample has a dip in performance at 20 and 30 °C which is caused by a higher order mode aligning poorly with the fundamental mode, and will be discussed in detail in a subsequent section.

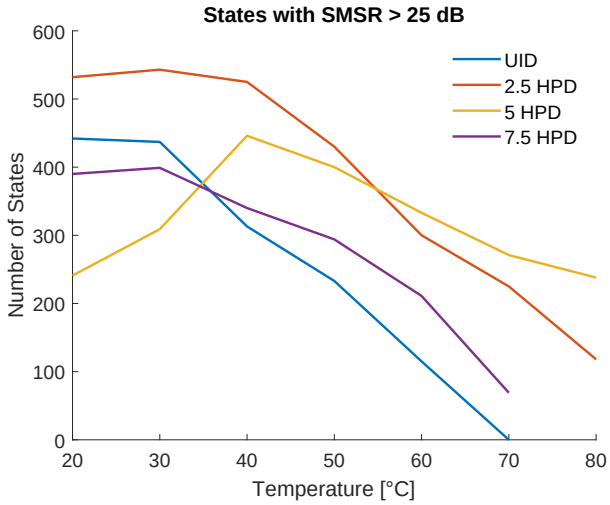

Figure 5.10: The number of states with SMSR greater than 25 dB versus temperature for MLLs with 0 (UID), 2.5, 5, and 7.5 HPD.

The figure of merit most central to this investigation is the WPE/C, which is shown in Figure 5.11. The UID MLL has the highest achieved WPE/C, but shows poor tempera-

ture performance. The measured WPE/C is somewhat resilient to temperature increases up to 50 °C, which similar to the performance of the free-space WPE shown in Figure 5.3, but the efficiency steeply declines from 50 °C. The 5 HPD sample comes close to the UID device with 9% at 50°C, and remarkably maintains high efficiency at 70 and 80°C with 8.6% and 6.8% respectively.

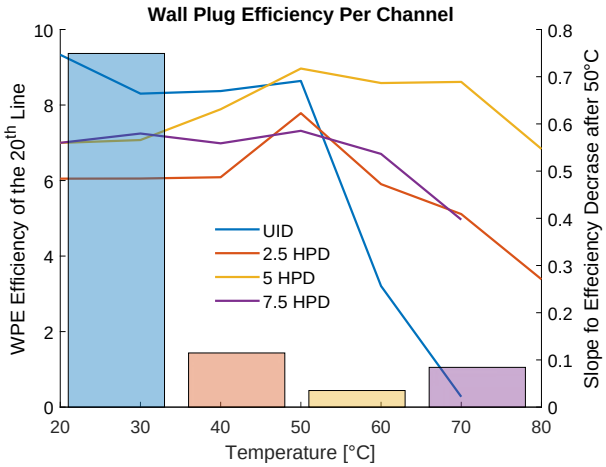

Figure 5.11: The WPE/C versus temperature for MLLs with 0 (UID), 2.5, 5, and 7.5 HPD.

Additionally, the available WPE/C data from 50 to 80°C is fit with a linear curve, and the slopes for the 0 (UID), 2.5, 5 and 7.5 HPD devices are overlaid on the image. The rollover in the UID device is -0.75%/°C, which is 21 times larger than the -0.035 %/°C roll-off in the 5 HPD sample. The 2.5 HPD sample has a slope of -0.11%/°C, which shows that the p-doping has already made a significant improvement, even at such a low level. The 2.5 HPD device has a lower starting efficiency than all the other devices, and this is a reflection of it having the lowest WPE in Figure 5.5. The 7.5 HPD device suprisingly has a similar slope to the 2.5 HPD sample with -.08 %/°C, but is likely from the pMD being too high, which also reduced the peak WPE/C through worse 20°C performance. This demonstrates that 5 HPD is the optimum level of doping.

In a DWDM system, the optical power of each channel is an extremely important parameter. In this study the analysis is centered on a 20-λ system, and the power of

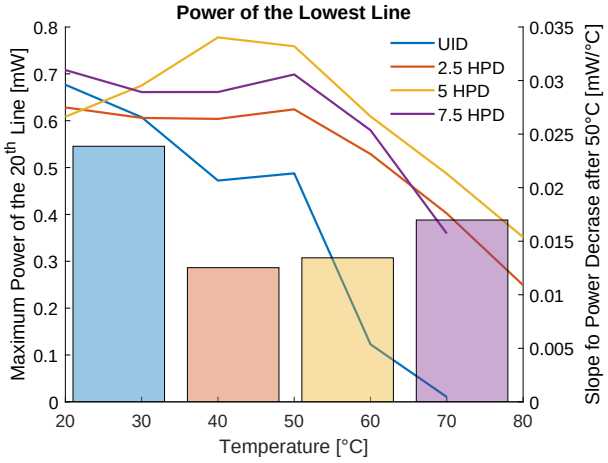

Figure 5.12: The PoLL versus temperature for MLLs with 0 (UID), 2.5, 5, and 7.5 HPD.

the 20^{th} channel, PoLL, is extracted in the method described in Subsection 3.5.3. The peak value of PoLL from the data collected is shown for each device in Figure 5.12. Additionally the slope of the degradation from 50°C is plotted on the right axis. The slope of three pMD devices are similar, and the they are about 2.5 dB better than the slope of the UID device. However, the UID device shows a strong decrease in the maximum PoLL immediately from 20°C, while the pMD devices all show a relatively flat power from 20 to 50°C. This shows the remarkable ability of the pMD devices to produce similar power and efficiency over a large temperature range. The 5 HPD device has the highest achieved PoLL of 0.78 mW and 0.76 mW at 40 and 50°C. The 2.5 and 5 HPD device has similar performance in this metric, which shows that the 2.5 HPD sample was mainly hampered by low free-space WPE, which was caused by a slightly higher threshold.

Lastly, it is important to consider the effective range of efficient operation in the MLLs used in this study, and how this changes with temperature. Figure 5.13a shows both the number of states that have channel efficiency that is less than 1 dB below the maximum WPE/C found at that given temperature for that device. This trend is noisy because the optimum SA bias can lie between two values, which will cause states at both SA values

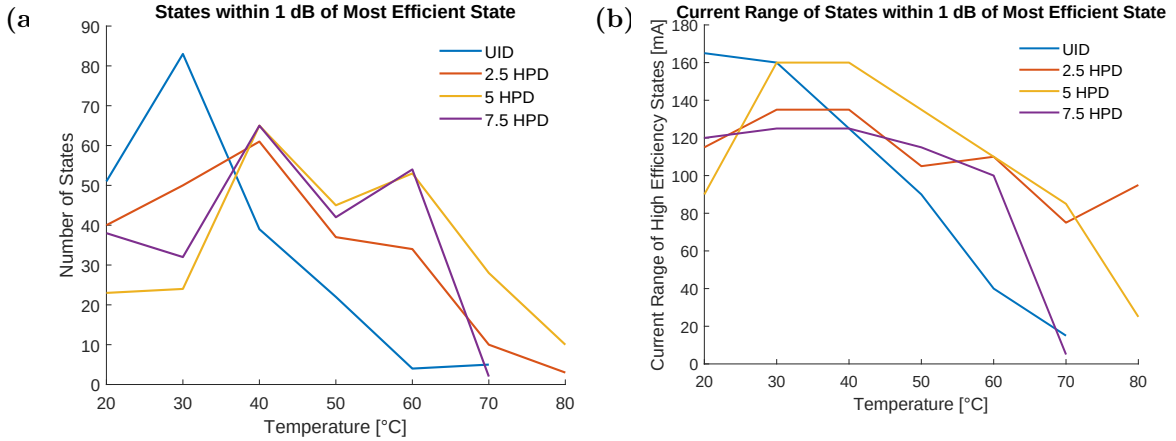

Figure 5.13: (a) The number of states recorded with WPE/C within 1 dB of the max WPE/C measured for that device and stage temperature for MLLs with 0 (UID), 2.5, 5, and 7.5 HPD. (b) displays the range of gain-current that the states in (a) occur throughout for each device.

to have high efficiency. However, it is useful for showing the decrease in area in a scan with increasing temperature. There is a clear trend for the highest doped samples to have the largest area of efficient operation at elevated temperatures, which is attributed to the increased saturated gain from the pMD giving delayed ES ASE and lasing onset (in both SA bias and temperature). This extends area of operation to higher injection currents, which also improves PoLL.

5.6 Presence of a Higher Order Mode in 5 HPD Sample

As was discussed earlier, the performance of the 5 HPD sample preforms poorly at 20 and 30°C. This is not due to poor LI performance, as was shown in Figure 5.4. Instead the comb performance is not ideal, as is shown in the selection of OSA traces in Figure 5.14. The * mark the 20 highest contiguous comb lines, following the same notation as Subsection 3.5.1. In 5.14a, the spectrum appears normal, however, tuning

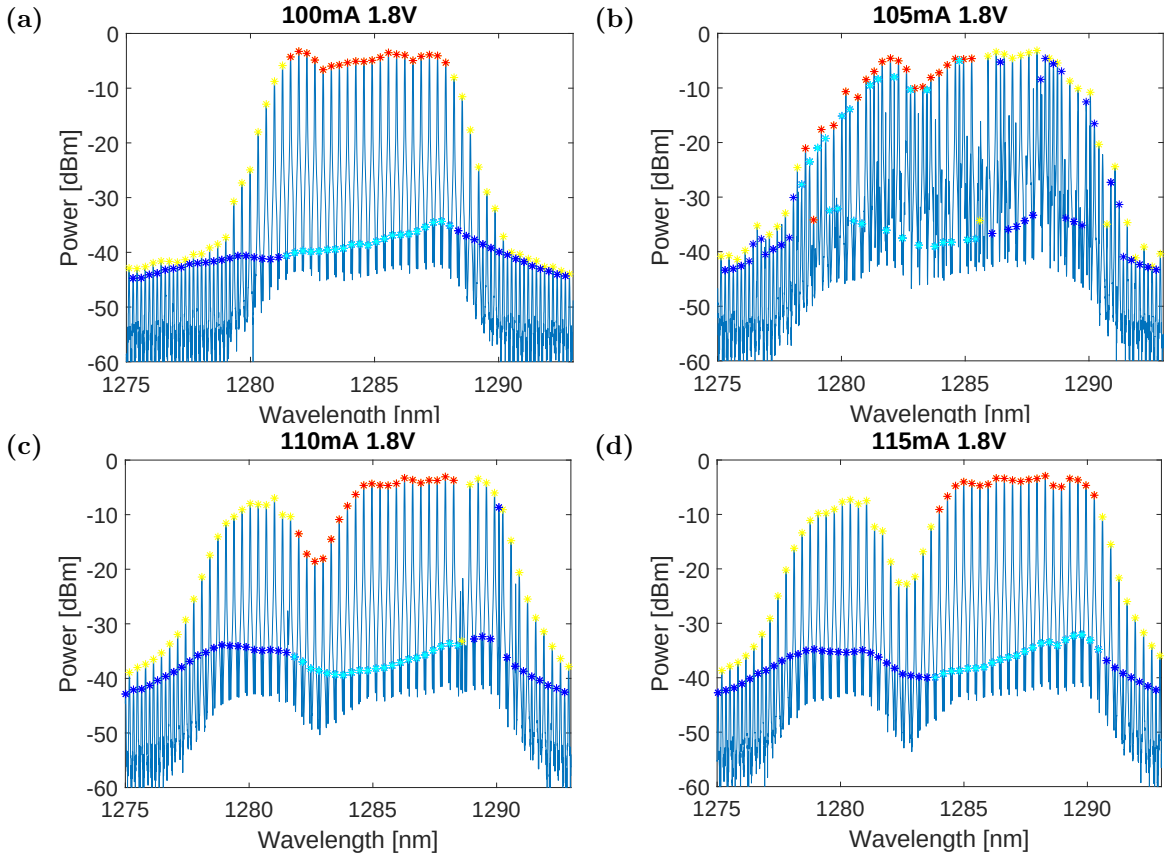

Figure 5.14: (a)-(d) shows the evolution of the optical spectrum over a short range of current at a constant SA bias at 20°C.

the gain current 5 mA causes the spectrum to be chaotic, as is shown in 5.14b, which is caused by the slight red-shifted from self heating. The presence of a higher order mode, which has a different effective index, can cause this behavior, by injecting noise that has a different periodicity than the repetition rate of the comb. This forces the comb into an unlocked state, which causes the comb to have a higher bandwidth than the locked state[124]. As the gain current increases, the device forms this double-humped profile, suppressing power by as much as 20 dB in the middle. There is a hysteresis effect around this area, and sweeping from higher to lower current will cause the spectrum to latch to the longer wavelength side before forming a double hump spectrum.

The broad ESA trace data is shown in Figure 5.15 for the four states in Figure 5.14

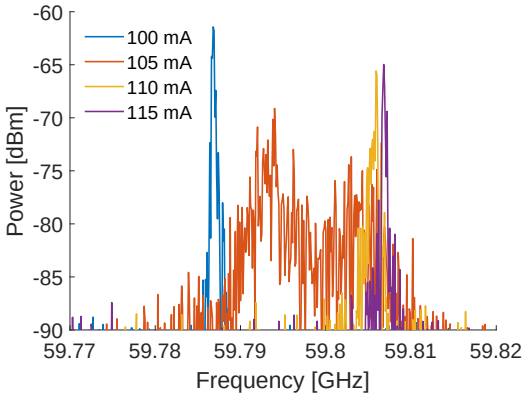

Figure 5.15: Low-resolution ESA trace of the the states plotted in Figure 5.14

(narrow ESA trace could not capture all of 5.14b). This shows that the unstable state processes two broad beat notes, which is causing this unstable behavior. The stable states at 95 and 115 mA both have narrow beat notes, but separated by 20 MHz. This behavior of skipping over a specific frequency or wavelength is characteristic of higher order modes interfering with mode locking. Figure 5.16 compares the 20 and 50 °C performance of the 5 HPD device. There is a clear segmentation of domains of high SMSR in Figure 5.16a, accompanied a frequency jump in Figure 5.16b. This behavior is not present at 50°C, which shows why the performance improves with increasing temperature, instead of degrading. All devices in the study were screened at 50°C, and other devices showed similar higher order mode problems, but at 50 °C instead of 20 °C. It was not possible to find a device that did not suffer from this issue through the entire temperature range in the 5 HPD samples.

5.7 Conclusion

This study analyzed the efficiency of generating a 20-λ comb with four MLLs with different levels of pMD. The lasers were designed to be as identical as possible, with the exception of the pMD in the active region, except for the UID device having five QD

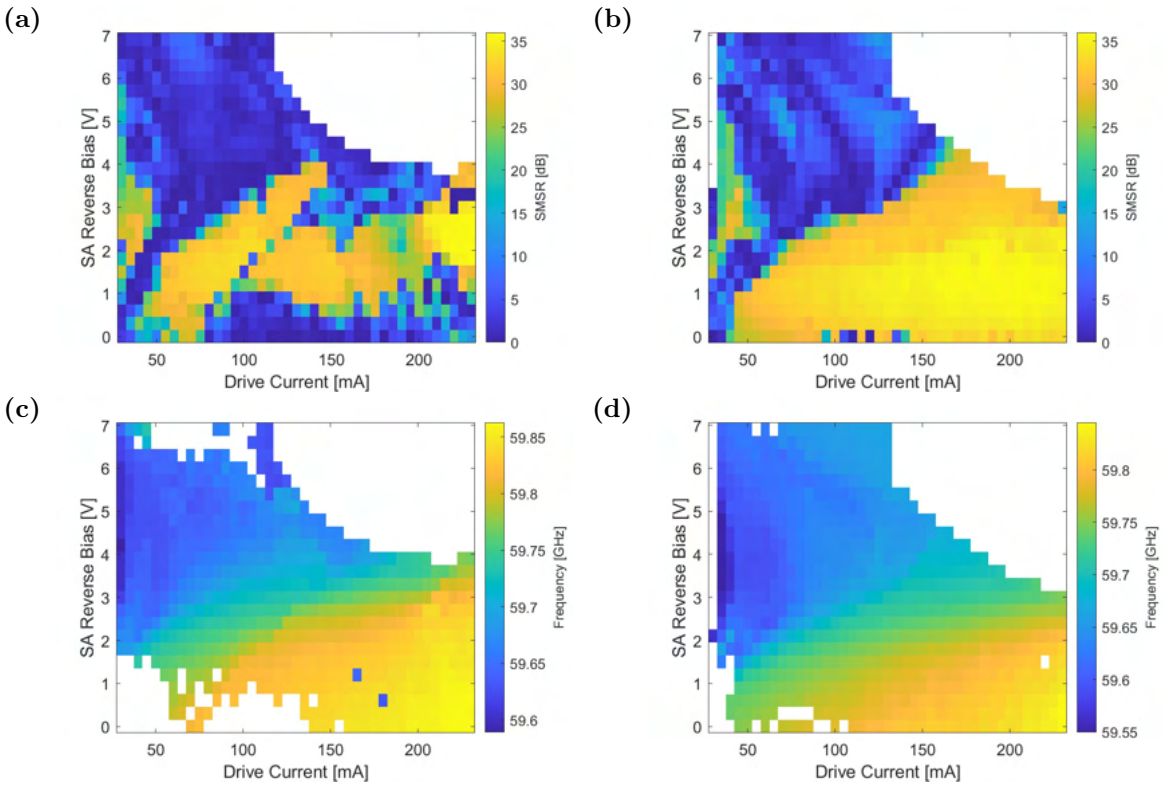

Figure 5.16: 2-D color coded plots from the 5 HPD device. (a) SMSR at 20°C. (b) SMSR at 50°C. (c) Beat Note Frequency at 20°C. (d) Beat Note Frequency at 50°C.

layers instead of six. The devices were analyzed both by their free-space output and their optical spectra, which were collected by an OSA. The 5 HPD sample was shown to have the best free space LI and WPE performance at elevated temperatures. An in-depth analysis of the optical spectra collected was conducted to analyze how the devices' free space performance translated to comb-line efficiency. To highlight the differences between the samples, five key parameters were identified. The performance between devices were compared, and the 5 HPD sample was shown to have the best performance between the four samples at 50°C and above. The 5 HPD MLL achieved a WPE/C of 9% and a PoLL of 0.77 mW. The 2.5 and 7.5 HPD devices have similar performance, which indicates that the optimum doping for MLLs is 5, which is considerably lower than what is used in FP and DFB lasers.

Chapter 6

Conclusion and Future Outlook

6.1 Highlighted Results

The investigation of OFCs generated by QD-MLLs was undertaken to understand, improve, and achieve the optimum performance. The framework for analyzing combs was discussed in Section 3.4, and the analysis of the data collected from an OSA, ESA, and AC were discussed. The device chosen as the example device shows remarkable performance, particularly when it comes to the peak WPE/C, which was 9.7% at 40°C. This device produces 58 states with WPE/C within 1 dB of the maximum achieved WPE/C, which spans 140 mA of the 200 mA current range. The PoLL achieved in this range varies from -3.7 tp -0.8 dBm. This performance can be seen in Figure 6.1a, reproduced from 3.7b.

The dynamics inside responsible for producing flat-topped combs with tunable bandwidth was discussed in Chapter 4. The dynamics that govern comb formation were found to be tunable from AM to FM in the same device. The phase relationship was directly measured through the stepped heterodyne technique, and the intermodal phase was indeed found to be equally spread across the range of 2π, which is shown in Figure 6.1b. This experimentally demonstrated that the combs used for data transmission are FM in

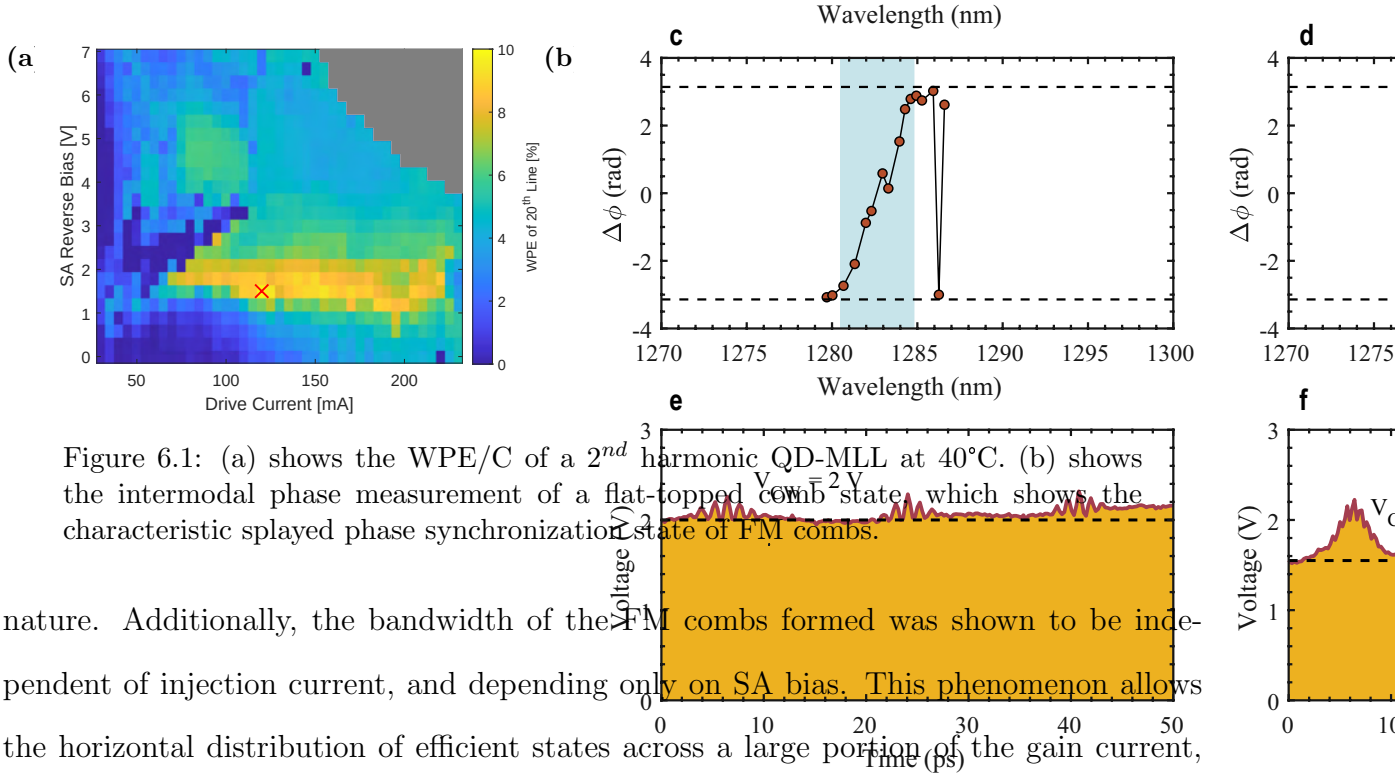

Figure 6.1: (a) shows the WPE/C of a 2^{nd} harmonic QD-MLL at 40°C. (b) shows the intermodal phase measurement of a flat-topped comb state, which shows the characteristic splayed phase synchronization state of FM combs.

nature. Additionally, the bandwidth of the FM combs formed was shown to be independent of injection current, and depending only on SA bias. This phenomenon allows the horizontal distribution of efficient states across a large portion of the gain current, because the bandwidth remains fixed despite increasing injection current, which is in stark contrast to the behavior of FP-QD lasers.

In the last chapter, the roll of pMD was investigated, particularly in how it affects the comb line efficiency at elevated temperatures. There has been a considerable amount of studies that examine the effects of pMD in FP lasers, however an analysis of the efficiency is often neglected, because the high doping levels used to maximize T_0 considerably reduces the efficiency. Additionally, no studies have been done on comparing the different doping levels in MLLs. The study presented in this dissertation was a comprehensive comparison of the doping level in QD-MLLs. The optimum doping for the 6 QD layer geometry was found to be 5 HPD. The maximum WPE/C achieved for the samples versus temperature is shown in Figure 6.2. The 5 HPD device achieves close to the same efficiency of the UID device, without considerable degradation until 70°C.

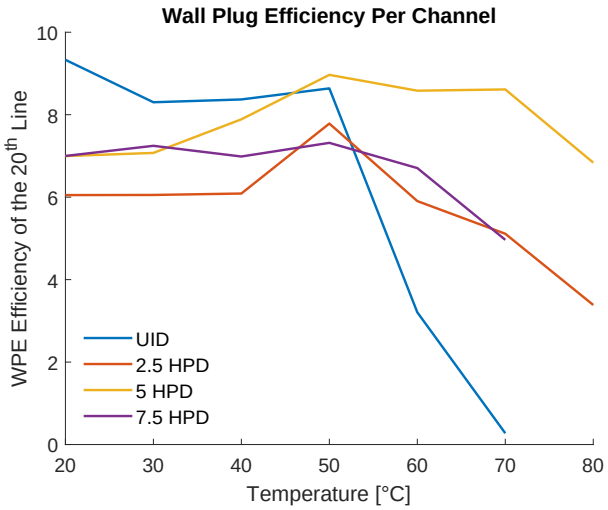

Figure 6.2: The WPE/C versus temperature for MLLs with 0 (UID), 2.5, 5, and 7.5 HPD.

6.2 Data Transmission

The overarching goal of the investigation into QD-MLLs was to study their ability to be DWDM light sources. For data transmission experiments, several QD-MLLs were packaged to improve their temperature and thus wavelength stability. In Section 1.2, a MRM-based system architecture was discussed which the entire efficiency analysis was built on. This system had an extremely dense architecture, to meet the needs of future datacenter photonic architectures. This extremely dense layout and the 36 μm pad pitch required the PIC to be copackaged with both a control integrated circuit (IC) and an RFIC. The copackaging process did not unfortunately have a high enough bond yield to test the full system architecture. Instead, standalone MRM and high speed silicon photonics PD where used to text the link architecture. Without the the full PIC available for system testing, individual standalone devices were tested. The setup and eye diagram are shown in Figure 6.3. The main limitation in this setup is the lack of a deinterleaver, which caused the channel spacing seen by the MRM to be 60 GHz instead of 120 GHz. This causes the Lorentzian lineshape of the MRM to overlap with two adjacent comb lines when it is electrically tuned for data modulation. This leads to light from one comb

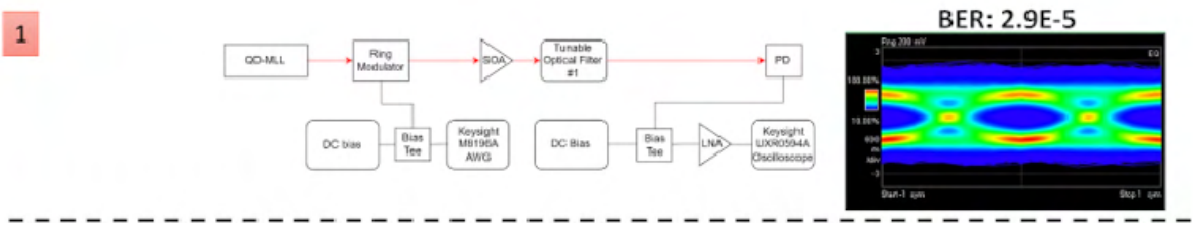

Figure 6.3: schematic of the different link experiments. Reproduced from [32]

line being close to on-resonance at all times, which causes excessive heating in the ring, which leads to nonlinear response and unstable resonance position. Additionally, the locking circuit designed for locking the ring resonance to the comb line is not present in this experiment and would only be in the fully packaged unit. These factors led to a degraded BER of 2.9×10^{-5}, which is close to the FEC decision threshold of the 1.3×10^{-5}.

Additionally, Section 1.2 discussed a DWDM transmission experiment using coherent data encoding. 26 comb lines were used for dual polarization 56 GBaud data transmission over 10 km of standard single mode fiber (SSMF). The experimental setup was shown in Figure 1.3, which contains two packaged QD-MLLs. In the testing configuration five lines are bulk modulated simultaneously, giving two aggressor channels on each side. More channels were not chosen to avoid saturation of the PDFA. Because this is coherent data transmission, bulk modulating represents the worst scenario for crosstalk interference. An example OSA trace of the modulated comb lines is shown in Figure 6.4a, with the filtered LO shown superimposed.

The BER data is shown in Figure 6.4b. Using 26 lines at 56 Gbaud DP-16QAM, an aggregate data rate of 10.2 Tb/s is achieved assuming 14.8% O-FEC overhead. Additionally, 26 lines are encoded with 56 Gbaud DP-32QAM to achieve a record setting 12.1 Tb/s for a single comb laser, assuming 20% overhead with SD-FEC. The low frequency drift of the lasers allowed the LO to be aligned to the carrier at the beginning, and not adjusted for the duration of the transmission capacity testing.

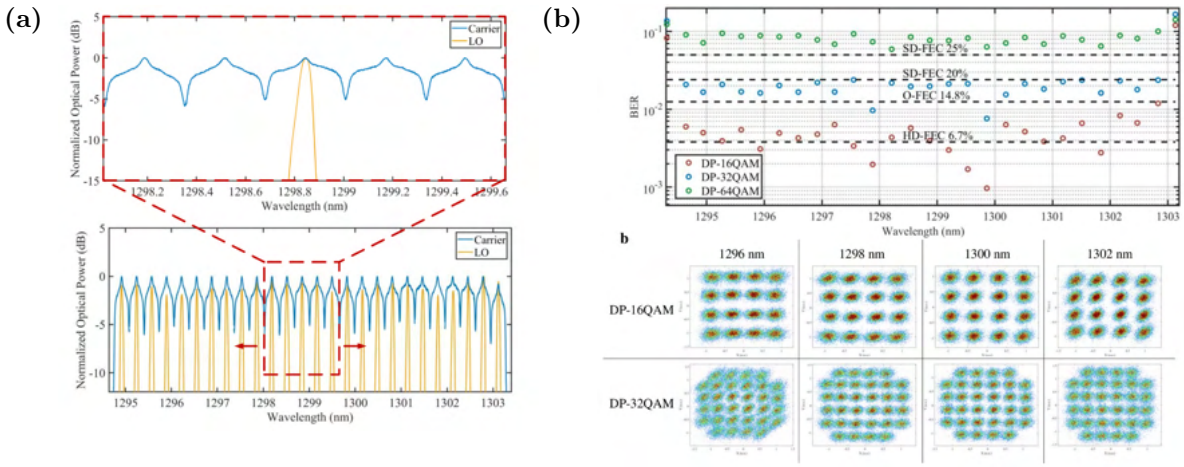

Figure 6.4: (a) shows the OSA spectrum of multiple comb lines modulated, with the LO superimposed. (b) shows the BER for the 28 channels considered under the three modulation formats considered, with example IQ diagrams for certain channels and modulation formats. Figures taken from [36]

6.3 Perspective Improvements for QD-MLLs

In this dissertation, a body of work was presented to prove that the QD-MLLs have demonstrated the ability to be the next generation of light sources for novel photonic interconnect architectures. As it currently stands, the device performance of 60 GHz lasers have reached a very mature level. There are small gains that could be made in performance of the laser itself, but large gains could not be made.

However, increasing the channel spacing was never investigated. If this could be substantially increased, it would make the architecture specifications more relaxed and system implementations more realizable. The device structure could easily accommodate increasing the repetition rate to 100 GHz. However going beyond becomes challenging. Higher harmonics can be used to alleviate the short cavity lengths. Rather, increasing the bandwidth would be the most challenging part, in order to maintain the same number of comb lines with similar power, while scaling up the channel spacing. If the waveguide dispersion can be effectively engineered, it could be used to increase the comb bandwidth

of the FM comb to try to accommodate a larger bandwidth. This could be used along with a chirped gain medium, to increase its gain bandwidth. These ideals would need to be perused in order to attempt achieving large spanning high repetition rate devices.

Bibliography

[1] C. V. Networking, "The zettabyte era–trends and analysis." Cisco white paper `https://www.cisco.com/c/en/us/solutions/collateral/service-provider/visualnetworking-index-vni/vni-hyperconnectivity-wp.html`, 2018. Accessed: 2021-11-04.

[2] N. Margalit, C. Xiang, S. M. Bowers, A. Bjorlin, R. Blum, and J. E. Bowers, *Perspective on the future of silicon photonics and electronics*, *Applied Physics Letters* **118** (2021), no. 22.

[3] C. Rakesh, "Looking beyond 400g - a syetem vendor perspective." `https://www.ieee802.org/3/B400G/public/21_02/chopra_b400g_01_210208.pdf`, 2020.

[4] A. Ghiasi, *Large data centers interconnect bottlenecks*, *Optics Express* **23** (Feb., 2015) 2085.

[5] Q. Cheng, M. Bahadori, M. Glick, S. Rumley, and K. Bergman, *Recent advances in optical technologies for data centers: a review*, *Optica* **5** (Nov., 2018) 1354.

[6] T. Komljenovic, D. Huang, P. Pintus, M. A. Tran, M. L. Davenport, and J. E. Bowers, *Photonic Integrated Circuits Using Heterogeneous Integration on Silicon*, *Proceedings of the IEEE* **106** (Dec., 2018) 2246–2257.

[7] A. Malik, S. Liu, E. Timurdogan, M. Harrington, A. Netherton, M. Saeidi, D. J. Blumenthal, L. Theogarajan, M. Watts, and J. E. Bowers, *Low power consumption silicon photonics datacenter interconnects enabled by a parallel architecture*, in *Optical Fiber Communication Conference*, pp. W6A–3, Optical Society of America, 2021.

[8] X. Zheng, E. Chang, I. Shubin, G. Li, Y. Luo, J. Yao, H. Thacker, J.-H. Lee, J. Lexau, F. Liu, *et. al.*, *A 33mw 100gbps cmos silicon photonic wdm transmitter using off-chip laser sources*, in *2013 Optical Fiber Communication Conference and Exposition and the National Fiber Optic Engineers Conference (OFC/NFOEC)*, pp. 1–3, IEEE, 2013.

[9] L. Chang, S. Liu, and J. E. Bowers, *Integrated optical frequency comb technologies*, *Nature Photonics* (Dec., 2021).

[10] L. Galdino, A. Edwards, W. Yi, E. Sillekens, Y. Wakayama, T. Gerard, W. S. Pelouch, S. Barnes, T. Tsuritani, R. I. Killey, D. Lavery, and P. Bayvel, *Optical Fibre Capacity Optimisation via Continuous Bandwidth Amplification and Geometric Shaping*, *IEEE Photonics Technology Letters* **32** (Sept., 2020) 1021–1024.

[11] "Distributed feedback lasers." `https://nanoplus.com/en/dfb-lasers/`. Accessed: 2024-05-04.

[12] X. Zheng, S. Lin, Y. Luo, J. Yao, G. Li, S. S. Djordjevic, J.-H. Lee, H. D. Thacker, I. Shubin, K. Raj, J. E. Cunningham, and A. V. Krishnamoorthy, *Efficient WDM Laser Sources Towards Terabyte/s Silicon Photonic Interconnects*, *Journal of Lightwave Technology* **31** (Dec., 2013) 4142–4154.

[13] P. Marin-Palomo, J. N. Kemal, M. Karpov, A. Kordts, J. Pfeifle, M. H. P. Pfeiffer, P. Trocha, S. Wolf, V. Brasch, M. H. Anderson, R. Rosenberger, K. Vijayan, W. Freude, T. J. Kippenberg, and C. Koos, *Microresonator-based solitons for massively parallel coherent optical communications*, *Nature* **546** (June, 2017) 274–279.

[14] N. G. Pavlov, S. Koptyaev, G. V. Lihachev, A. S. Voloshin, A. S. Gorodnitskiy, M. V. Ryabko, S. V. Polonsky, and M. L. Gorodetsky, *Narrow-linewidth lasing and soliton Kerr microcombs with ordinary laser diodes*, *Nature Photonics* **12** (Nov., 2018) 694–698.

[15] M. H. P. Pfeiffer, C. Herkommer, J. Liu, H. Guo, M. Karpov, E. Lucas, M. Zervas, and T. J. Kippenberg, *Octave-spanning dissipative Kerr soliton frequency combs in Si_3n_4 microresonators*, *Optica* **4** (July, 2017) 684.

[16] M. W. Harrington, G. M. Brodnik, T. C. Briles, J. R. Stone, R. H. Streater, S. B. Papp, and D. J. Blumenthal, *Kerr Soliton Microcomb Pumped by an Integrated SBS Laser for Ultra-Low Linewidth WDM Sources*, in *Optical Fiber Communication Conference (OFC) 2020*, (San Diego, California), p. T4G.6, OSA, 2020.

[17] C. Bao, L. Zhang, A. Matsko, Y. Yan, Z. Zhao, G. Xie, A. M. Agarwal, L. C. Kimerling, J. Michel, L. Maleki, and A. E. Willner, *Nonlinear conversion efficiency in Kerr frequency comb generation*, *Optics Letters* **39** (Nov., 2014) 6126.

[18] B. Y. Kim, Y. Okawachi, J. K. Jang, M. Yu, X. Ji, Y. Zhao, C. Joshi, M. Lipson, and A. L. Gaeta, *Turn-key, high-efficiency Kerr comb source*, *Optics Letters* **44** (Sept., 2019) 4475.

[19] C. Xiang, J. Liu, J. Guo, L. Chang, R. N. Wang, W. Weng, J. Peters, W. Xie, Z. Zhang, J. Riemensberger, *et. al.*, *Laser soliton microcombs heterogeneously integrated on silicon*, *Science* **373** (2021), no. 6550 99–103.

[20] H. Hu, F. Da Ros, M. Pu, F. Ye, K. Ingerslev, E. Porto da Silva, M. Nooruzzaman, Y. Amma, Y. Sasaki, T. Mizuno, Y. Miyamoto, L. Ottaviano, E. Semenova, P. Guan, D. Zibar, M. Galili, K. Yvind, T. Morioka, and L. K. Oxenløwe, *Single-source chip-based frequency comb enabling extreme parallel data transmission*, *Nature Photonics* **12** (Aug., 2018) 469–473.

[21] P. Delfyett, D. Hartman, and S. Ahmad, *Optical clock distribution using a mode-locked semiconductor laser diode system*, *Journal of Lightwave Technology* **9** (Dec., 1991) 1646–1649.

[22] O. Wada, *Femtosecond all-optical devices for ultrafast communication and signal processing*, *New Journal of Physics* **6** (Nov., 2004) 183–183.

[23] S. Liu, X. Wu, D. Jung, J. C. Norman, M. Kennedy, H. K. Tsang, A. C. Gossard, and J. E. Bowers, *High-channel-count 20 ghz passively mode-locked quantum dot laser directly grown on si with 4.1 tbit/s transmission capacity*, *Optica* **6** (2019), no. 2 128–134.

[24] G. Liu, A. Stintz, H. Li, K. Malloy, and L. Lester, *Extremely low room-temperature threshold current density diode lasers using InAs dots in In0.15Ga0.85As quantum well*, *Electronics Letters* **35** (1999), no. 14 1163.

[25] W. W. Chow, Z. Zhang, J. C. Norman, S. Liu, and J. E. Bowers, *On quantum-dot lasing at gain peak with linewidth enhancement factor $\alpha_h = 0$*, *APL Photonics* **5** (Feb., 2020) 026101.

[26] T. Akiyama, M. Ekawa, M. Sugawara, K. Kawaguchi, Hisao Sudo, A. Kuramata, H. Ebe, and Y. Arakawa, *An ultrawide-band semiconductor optical amplifier having an extremely high penalty-free output power of 23 dBm achieved with quantum dots*, *IEEE Photonics Technology Letters* **17** (Aug., 2005) 1614–1616.

[27] Y. Arakawa and H. Sakaki, *Multidimensional quantum well laser and temperature dependence of its threshold current*, *Applied physics letters* **40** (1982), no. 11 939–941.

[28] T. Vallaitis, C. Koos, R. Bonk, W. Freude, M. Laemmlin, C. Meuer, D. Bimberg, and J. Leuthold, *Slow and fast dynamics of gain and phase in a quantum dot semiconductor optical amplifier*, *Optics express* **16** (2008), no. 1 170–178.

[29] M. Dumont, S. Liu, M. Kennedy, and J. Bowers, *High-efficiency quantum dot lasers as comb sources for dwdm applications*, *Applied Sciences* **12** (2022), no. 4 1836.

[30] A. Kovsh, A. Gubenko, I. Krestnikov, D. Livshits, S. Mikhrin, J. Weimert, L. West, G. Wojcik, D. Yin, C. Bornholdt, *et. al.*, *Quantum dot comb-laser as efficient light source for silicon photonics*, in *Silicon Photonics and Photonic Integrated Circuits*, vol. 6996, pp. 214–225, SPIE, 2008.

[31] D. Livshits, D. Yin, A. Gubenko, I. Krestnikov, S. Mikhrin, A. Kovsh, and G. Wojcik, *Cost-effective wdm optical interconnects enabled by quantum dot comb lasers*, in *Optoelectronic Interconnects and Component Integration IX*, vol. 7607, pp. 255–263, SPIE, 2010.

[32] A. Netherton, M. Dumont, Z. Nelson, J. Koo, J. Jhonsa, A. Mo, D. McCarthy, S. Deckoff-Jones, Y. Gao, N. Pestana, J. Goldstein, R.-J. Shiue, C. Poulton, M. Kennedy, M. Harrington, B. Dong, J. Bovington, M. Frankel, L. Theogarajan, M. Watts, D. Blumenthal, and J. E. Bowers, *High capacity, low power, short reach integrated silicon photonic interconnects*, *Photonics Research (Submitted)* (2024).

[33] K. Padmaraju, X. Zhu, L. Chen, M. Lipson, and K. Bergman, *Intermodulation crosstalk characteristics of wdm silicon microring modulators*, *IEEE Photonics Technology Letters* **26** (2014), no. 14 1478–1481.

[34] M. Georgas, J. Leu, B. Moss, C. Sun, and V. Stojanović, *Addressing link-level design tradeoffs for integrated photonic interconnects*, in *2011 IEEE Custom Integrated Circuits Conference (CICC)*, pp. 1–8, IEEE, 2011.

[35] A. Razumov, H. R. Heebøll, M. Dummont, O. Terra, B. Dong, J. Riebesehl, P. Varming, J. E. Pedersen, F. D. Ros, J. E. Bowers, *et. al.*, *Subspace tracking for phase noise source separation in frequency combs*, *Optics Express* **31** (2023), no. 21 34325–34347.

[36] S. Bernal, M. Dumont, E. Berikaa, C. St-Arnault, Y. Hu, R. Gutierrez Castrejon, W. Li, Z. Wei, B. Krueger, F. Pittalà, J. Bowers, and D. V. Plant, *12.1 terabit/second data center interconnects using o-band coherent transmission with frequency combs*, *Nature Communications (Submitted)* (2024).

[37] M. J. Heck, E. A. Bente, B. Smalbrugge, Y.-S. Oei, M. K. Smit, S. Anantathanasarn, and R. Nötzel, *Observation of q-switching and mode-locking in two-section inas/inp (100) quantum dot lasers around 1.55 μm*, *Optics Express* **15** (2007), no. 25 16292–16301.

[38] R. Rosales, K. Merghem, C. Calo, G. Bouwmans, I. Krestnikov, A. Martinez, and A. Ramdane, *Optical pulse generation in single section inas/gaas quantum dot edge emitting lasers under continuous wave operation*, *Applied Physics Letters* **101** (2012), no. 22.

[39] P. Marin-Palomo, J. N. Kemal, P. Trocha, S. Wolf, K. Merghem, F. Lelarge, A. Ramdane, W. Freude, S. Randel, and C. Koos, *Comb-based wdm transmission at 10 tbit/s using a dc-driven quantum-dash mode-locked laser diode*, *Optics Express* **27** (2019), no. 22 31110–31129.

[40] J. N. Kemal, P. Marin-Palomo, K. Merghem, G. Aubin, F. Lelarge, A. Ramdane, S. Randel, W. Freude, and C. Koos, *32qam wdm transmission at 12 tbit/s using a quantum-dash mode-locked laser diode (qd-mlld) with external-cavity feedback*, *Optics Express* **28** (2020), no. 16 23594–23608.

[41] Z. Lu, J. Liu, L. Mao, C.-Y. Song, J. Weber, and P. Poole, *12.032 tbit/s coherent transmission using an ultra-narrow linewidth qantum dot 34.46-ghz c-band coherent comb laser*, in *Next-Generation Optical Communication: Components, Sub-Systems, and Systems VIII*, vol. 10947, pp. 116–122, SPIE, 2019.

[42] Y. Mao, G. Liu, K. Zeb, Z. Lu, J. Liu, P. J. Poole, C.-Y. Song, and P. Barrios, *Ultralow noise and timing jitter semiconductor quantum-dot passively mode-locked laser for terabit/s optical networks*, in *Photonics*, vol. 9, p. 695, MDPI, 2022.

[43] G. Liu, P. J. Poole, Z. Lu, J. Liu, C.-Y. Song, Y. Mao, and P. Barrios, *Mode-locking and noise characteristics of inas/inp quantum dash/dot lasers*, *Journal of Lightwave Technology* **41** (2023), no. 13 4262–4270.

[44] R. Mirin, J. Ibbetson, K. Nishi, A. Gossard, and J. Bowers, *1.3 μm photoluminescence from ingaas quantum dots on gaas*, *Applied physics letters* **67** (1995), no. 25 3795–3797.

[45] V. Shchukin, N. N. Ledentsov, and D. Bimberg, *Epitaxy of nanostructures*. Springer Science & Business Media, 2004.

[46] K. Y. K. Yamaguchi, K. Y. K. Yujobo, and T. K. T. Kaizu, *Stranski-krastanov growth of inas quantum dots with narrow size distribution*, *Japanese journal of applied physics* **39** (2000), no. 12A L1245.

[47] F. Ferdos, M. Sadeghi, Q. X. Zhao, S. Wang, and A. Larsson, *Optimisation of mbe growth conditions for inas quantum dots on (0 0 1) gaas for 1.3 μm luminescence*, *Journal of crystal growth* **227** (2001) 1140–1145.

[48] P. Joyce, T. Krzyzewski, G. Bell, T. Jones, S. Malik, D. Childs, and R. Murray, *Growth rate effects on the size, composition and optical properties of inas/gaas quantum dots grown by molecular beam epitaxy*, *Journal of crystal growth* **227** (2001) 1000–1004.

[49] A. Balzarotti, *The evolution of self-assembled inas/gaas (001) quantum dots grown by growth-interrupted molecular beam epitaxy*, *Nanotechnology* **19** (2008), no. 50 505701.

[50] T. Amano, T. Sugaya, and K. Komori, *Highest density 1.3 μm inas quantum dots covered with gradient composition ingaas strain reduced layer grown with an as2 source using molecular beam epitaxy*, *Japanese journal of applied physics* **44** (2005), no. 3L L432.

[51] C. Chia, Y. Zhang, S. Wong, A. Yong, S. Chow, S. Chua, and J. Guo, *Saturated dot density of inas/ gaas self-assembled quantum dots grown at high growth rate*, *Applied Physics Letters* **90** (2007), no. 16.

[52] Z. Wasilewski, S. Fafard, and J. McCaffrey, *Size and shape engineering of vertically stacked self-assembled quantum dots*, *Journal of crystal growth* **201** (1999) 1131–1135.

[53] K. Nishi, H. Saito, S. Sugou, and J.-S. Lee, *A narrow photoluminescence linewidth of 21 mev at 1.35 μm from strain-reduced inas quantum dots covered by in 0.2 ga 0.8 as grown on gaas substrates*, *Applied Physics Letters* **74** (1999), no. 8 1111–1113.

[54] V. Ustinov, N. Maleev, A. Zhukov, A. Kovsh, A. Y. Egorov, A. Lunev, B. Volovik, I. Krestnikov, Y. G. Musikhin, N. Bert, *et. al.*, *Inas/ingaas quantum dot structures on gaas substrates emitting at 1.3 μm*, *Applied physics letters* **74** (1999), no. 19 2815–2817.

[55] J. C. Norman, S. Liu, Y. Wan, Z. Zhang, C. Shang, J. G. Selvidge, M. Dumont, M. Kennedy, D. Jung, J. Duan, *et. al.*, *Epitaxial integration of high-performance quantum-dot lasers on silicon*, in *Silicon Photonics XV*, vol. 11285, pp. 20–27, SPIE, 2020.

[56] B. Dong, M. Dumont, O. Terra, H. Wang, A. Netherton, and J. E. Bowers, *Broadband quantum-dot frequency-modulated comb laser*, *Light: Science & Applications* **12** (2023), no. 1 182.

[57] M. Heiblum, W. Wang, L. Osterling, and V. Deline, *Heavy doping of gaas and algaas with silicon by molecular beam epitaxy*, *Journal of applied physics* **54** (1983), no. 11 6751–6753.

[58] N. Chand, T. Henderson, J. Klem, W. T. Masselink, R. Fischer, Y.-C. Chang, and H. Morkoĉ, *Comprehensive analysis of si-doped al x ga 1- x as (x= 0 to 1): Theory and experiments*, *Physical Review B* **30** (1984), no. 8 4481.

[59] P. Mooney, *Deep donor levels (dx centers) in iii-v semiconductors*, *Journal of Applied Physics* **67** (1990), no. 3 R1–R26.

[60] B. Wu, Y. Mii, M. Chen, and K. Wang, *Effect of arsenic dimer species to silicon doping of gaas layers prepared by molecular beam epitaxy*, *Applied physics letters* **58** (1991), no. 4 391–393.

[61] K. Feng, C. Shang, E. Hughes, A. Clark, R. Koscica, P. Ludewig, D. Harame, and J. Bowers, *Quantum dot lasers directly grown on 300 mm si wafers: Planar and in-pocket*, in *Photonics*, vol. 10, p. 534, MDPI, 2023.

[62] C. Shang, E. Hughes, Y. Wan, M. Dumont, R. Koscica, J. Selvidge, R. Herrick, A. C. Gossard, K. Mukherjee, and J. E. Bowers, *High-temperature reliable quantum-dot lasers on si with misfit and threading dislocation filters*, *Optica* **8** (2021), no. 5 749–754.

[63] Y. Wan, D. Jung, J. Norman, K. Feng, A. Dagli, A. C. Gossard, and J. E. Bowers, *Quadruple reduction of threshold current density for micro-ring quantum dot lasers epitaxially grown on (001) Si*, in *Conference on Lasers and Electro-Optics*, (San Jose, California), p. SW3Q.3, OSA, 2018.

[64] T. Udem, R. Holzwarth, and T. W. Hänsch, *Optical frequency metrology*, *Nature* **416** (2002), no. 6877 233–237.

[65] P.-T. Ho, *Coherent pulse generation with a gaalas laser by active modelocking*, *Electronics Letters* **15** (1979), no. 17 526–527.

[66] A. Morimoto, T. Kobayashi, and T. Sueta, *Active mode locking of lasers using an electrooptic deflector*, *IEEE journal of quantum electronics* **24** (1988), no. 1 94–98.

[67] D. Kuizenga and A. Siegman, *Fm and am mode locking of the homogeneous laser-part i: Theory*, *IEEE Journal of Quantum Electronics* **6** (1970), no. 11 694–708.

[68] J. E. Bowers, P. A. Morton, A. Mar, and S. W. Corzine, *Actively mode-locked semiconductor lasers*, *IEEE Journal of Quantum Electronics* **25** (1989), no. 6 1426–1439.

[69] K. Sato, H. Ishii, I. Kotaka, Y. Kondo, and M. Yamamoto, *Frequency range extension of actively mode-locked lasers integrated with electroabsorption modulators using chirped gratings*, *IEEE Journal Of Selected Topics In Quantum Electronics* **3** (1997), no. 2 250–255.

[70] E. Avrutin and J. Javaloyes, *Mode-locked semiconductor lasers*, in *Handbook of Optoelectronic Device Modeling and Simulation*, pp. 183–234. CRC Press, 2017.

[71] G. Cerullo, S. De Silvestri, and V. Magni, *Self-starting kerr-lens mode locking of a ti: sapphire laser*, *Optics letters* **19** (1994), no. 14 1040–1042.

[72] H. A. Haus, J. G. Fujimoto, and E. P. Ippen, *Analytic theory of additive pulse and kerr lens mode locking*, *IEEE Journal of quantum electronics* **28** (1992), no. 10 2086–2096.

[73] T. Brabec, C. Spielmann, P. Curley, and F. Krausz, *Kerr lens mode locking*, *Optics letters* **17** (1992), no. 18 1292–1294.

[74] H. A. Haus, *Theory of mode locking with a fast saturable absorber*, *Journal of Applied Physics* **46** (1975), no. 7 3049–3058.

[75] H. Haus, *Theory of mode locking with a slow saturable absorber*, *IEEE Journal of Quantum Electronics* **11** (1975), no. 9 736–746.

[76] E. P. Ippen, *Principles of passive mode locking*, *Applied Physics B* **58** (1994) 159–170.

[77] I. Jung, F. Kärtner, N. Matuschek, D. Sutter, F. Morier-Genoud, Z. Shi, V. Scheuer, M. Tilsch, T. Tschudi, and U. Keller, *Semiconductor saturable absorber mirrors supporting sub-10-fs pulses.*, *Applied Physics B: Lasers & Optics* **65** (1997), no. 2.

[78] U. Keller, K. J. Weingarten, F. X. Kartner, D. Kopf, B. Braun, I. D. Jung, R. Fluck, C. Honninger, N. Matuschek, and J. A. Der Au, *Semiconductor saturable absorber mirrors (sesam's) for femtosecond to nanosecond pulse generation in solid-state lasers*, *IEEE Journal of selected topics in QUANTUM ELECTRONICS* **2** (1996), no. 3 435–453.

[79] E. Ippen, D. Eilenberger, and R. Dixon, *Picosecond pulse generation by passive mode locking of diode lasers*, *Applied Physics Letters* **37** (1980), no. 3 267–269.

[80] Y. Silberberg, P. Smith, D. Eilenberger, D. Miller, A. Gossard, and W. Wiegmann, *Passive mode locking of a semiconductor diode laser*, *Optics letters* **9** (1984), no. 11 507–509.

[81] D. J. Derickson, R. J. Helkey, A. Mar, J. R. Karin, J. G. Wasserbauer, and J. E. Bowers, *Short pulse generation using multisegment mode-locked semiconductor lasers*, *IEEE Journal of Quantum Electronics* **28** (1992), no. 10 2186–2202.

[82] S. Hunsche, H. Heesel, A. Ewertz, H. Kurz, and J. Collet, *Spectral-hole burning and carrier thermalization in gaas at room temperature*, *Physical Review B* **48** (1993), no. 24 17818.

[83] D. Malins, A. Gomez-Iglesias, S. White, W. Sibbett, A. Miller, and E. Rafailov, *Ultrafast electroabsorption dynamics in an inas quantum dot saturable absorber at 1.3 μm*, *Applied Physics Letters* **89** (2006), no. 17.

[84] M. Singleton, P. Jouy, M. Beck, and J. Faist, *Evidence of linear chirp in mid-infrared quantum cascade lasers*, *Optica* **5** (2018), no. 8 948–953.

[85] B. Schwarz, J. Hillbrand, M. Beiser, A. M. Andrews, G. Strasser, H. Detz, A. Schade, R. Weih, and S. Höfling, *Monolithic frequency comb platform based on interband cascade lasers and detectors*, *Optica* **6** (2019), no. 7 890–895.

[86] J. Hillbrand, D. Auth, M. Piccardo, N. Opačak, E. Gornik, G. Strasser, F. Capasso, S. Breuer, and B. Schwarz, *In-phase and anti-phase synchronization in a laser frequency comb*, *Physical review letters* **124** (2020), no. 2 023901.

[87] S. G. Murdoch, R. T. Watts, Y. Xu, R. Maldonado-Basilio, J. Parra-Cetina, S. Latkowski, P. Landais, and L. P. Barry, *Spectral amplitude and phase measurement of a 40 ghz free-running quantum-dash modelocked laser diode*, *Optics Express* **19** (2011), no. 14 13628–13635.

[88] C. Calò, V. Vujicic, R. Watts, C. Browning, K. Merghem, V. Panapakkam, F. Lelarge, A. Martinez, B.-E. Benkelfat, A. Ramdane, *et. al.*, *Single-section quantum well mode-locked laser for 400 gb/s ssb-ofdm transmission*, *Optics Express* **23** (2015), no. 20 26442–26449.

[89] M. Dong, S. T. Cundiff, and H. G. Winful, *Physics of frequency-modulated comb generation in quantum-well diode lasers*, *Physical Review A* **97** (2018), no. 5 053822.

[90] K. Sato, *100 ghz optical pulse generation using fabry-perot laser under continuous wave operation*, *Electronics Letters* **37** (2001), no. 12 1.

[91] Y. Nomura, S. Ochi, N. Tomita, K. Akiyama, T. Isu, T. Takiguchi, and H. Higuchi, *Mode locking in fabry-perot semiconductor lasers*, *Physical Review A* **65** (2002), no. 4 043807.

[92] R. Paiella, F. Capasso, C. Gmachl, D. L. Sivco, J. N. Baillargeon, A. L. Hutchinson, A. Y. Cho, and H. Liu, *Self-mode-locking of quantum cascade lasers with giant ultrafast optical nonlinearities*, *Science* **290** (2000), no. 5497 1739–1742.

[93] S. Liu, D. Jung, J. Norman, M. Kennedy, A. Gossard, and J. Bowers, *490 fs pulse generation from passively mode-locked single section quantum dot laser directly grown on on-axis gap/si*, *Electronics Letters* **54** (2018), no. 7 432–433.

[94] C. Weber, L. L. Columbo, M. Gioannini, S. Breuer, and P. Bardella, *Threshold behavior of optical frequency comb self-generation in an inas/ingaas quantum dot laser*, *Optics letters* **44** (2019), no. 14 3478–3481.

[95] J. Renaudier, R. Brenot, B. Dagens, F. Lelarge, B. Rousseau, F. Poingt, O. Legouezigou, F. Pommereau, A. Accard, P. Gallion, *et. al.*, *45 ghz self-pulsation with narrow linewidth in quantum dot fabry-perot semiconductor lasers at 1.5 μm*, *Electronics Letters* **41** (2005), no. 18 1.

[96] S. Harris and O. McDuff, *Theory of fm laser oscillation*, *IEEE Journal of Quantum Electronics* **1** (1965), no. 6 245–262.

[97] D. Kuizenga and A. Siegman, *Fm-laser operation of the nd: Yag laser*, *IEEE Journal of Quantum Electronics* **6** (1970), no. 11 673–677.

[98] M. Thompson, C. Marinelli, X. Zhao, R. Sellin, R. Penty, I. White, I. Kaiander, D. Bimberg, D.-J. Kang, and M. Blamire, *Colliding-pulse modelocked quantum dot lasers*, *Electronics Letters* **41** (2005), no. 5 248.

[99] P. J. Winzer and W. R. Leeb, *Coherent lidar at low signal powers: basic considerations on optical heterodyning*, *Journal of modern Optics* **45** (1998), no. 8 1549–1555.

[100] L. Drzewietzki, S. Breuer, and W. Elsäßer, *Timing jitter reduction of passively mode-locked semiconductor lasers by self-and external-injection: Numerical description and experiments*, *Optics Express* **21** (2013), no. 13 16142–16161.

[101] E. Ippen, C. Shank, and S. L. Shapiro, *Ultrashort light pulses: Picosecond techniques and applications*. Springer-Verlag, New York, 1977.

[102] A. M. Weiner, *Ultrafast optics*. John Wiley & Sons, 2011.

[103] P. Bardella, L. L. Columbo, and M. Gioannini, *Self-generation of optical frequency comb in single section quantum dot fabry-perot lasers: a theoretical study*, *Optics express* **25** (2017), no. 21 26234–26252.

[104] X. Huang, A. Stintz, H. Li, L. Lester, J. Cheng, and K. Malloy, *Passive mode-locking in 1.3 μm two-section inas quantum dot lasers*, *Applied Physics Letters* **78** (2001), no. 19 2825–2827.

[105] M. Thompson, K. Tan, C. Marinelli, K. Williams, R. Penty, I. White, M. Kuntz, D. Ouyang, D. Bimberg, V. Ustinov, *et. al.*, *Transform-limited optical pulses from 18 ghz monolithic modelocked quantum dot lasers operating at˜ 1.3 μm*, *Electronics Letters* **40** (2004), no. 5 1.

[106] E. U. Rafailov, M. A. Cataluna, W. Sibbett, N. Il'Inskaya, Y. M. Zadiranov, A. Zhukov, V. Ustinov, D. A. Livshits, A. Kovsh, and N. Ledentsov, *High-power picosecond and femtosecond pulse generation from a two-section mode-locked quantum-dot laser*, *Applied Physics Letters* **87** (2005), no. 8 081107.

[107] J.-C. Diels and W. Rudolph, *Ultrashort laser pulse phenomena*. Elsevier, 2006.

[108] Z. Zhang, J. C. Norman, S. Liu, A. Malik, and J. E. Bowers, *Integrated dispersion compensated mode-locked quantum dot laser*, *Photonics Research* **8** (2020), no. 9 1428–1434.

[109] C. L. Tang, H. Statz, and G. deMars, *Spectral output and spiking behavior of solid-state lasers*, *Journal of Applied Physics* **34** (1963), no. 8 2289–2295.

[110] G. P. Agrawal, *Population pulsations and nondegenerate four-wave mixing in semiconductor lasers and amplifiers*, *JOSA B* **5** (1988), no. 1 147–159.

[111] M. Homar, J. Moloney, and M. San Miguel, *Travelling wave model of a multimode fabry-perot laser in free running and external cavity configurations*, *IEEE Journal of Quantum Electronics* **32** (1996), no. 3 553–566.

[112] L. Tiemeijer, *Effects of nonlinear gain on four-wave mixing and asymmetric gain saturation in a semiconductor laser amplifier*, *Applied physics letters* **59** (1991), no. 5 499–501.

[113] A. Mecozzi, *Cavity standing-wave and gain compression coefficient in semiconductor lasers*, *Optics letters* **19** (1994), no. 9 640–642.

[114] J. Duan, B. Dong, W. W. Chow, H. Huang, S. Ding, S. Liu, J. C. Norman, J. E. Bowers, and F. Grillot, *Four-wave mixing in 1.3 μm epitaxial quantum dot lasers directly grown on silicon*, *Photonics Research* **10** (2022), no. 5 1264–1270.

[115] D. Reid, S. Murdoch, and L. Barry, *Stepped-heterodyne optical complex spectrum analyzer.*, *Optics express* **18** (2010), no. 19 19724–19731.

[116] X. Tang, A. S. Karar, J. C. Cartledge, A. Shen, and G.-H. Duan, *Characterization of a mode-locked quantum-dash fabry-perot laser based on measurement of the complex optical spectrum*, in *2009 35th European Conference on Optical Communication*, pp. 1–2, IEEE, 2009.

[117] M. Kwakernaak, R. Schreieck, A. Neiger, H. Jackel, E. Gini, and W. Vogt, *Spectral phase measurement of mode-locked diode laser pulses by beating sidebands generated by electrooptical mixing*, *IEEE Photonics Technology Letters* **12** (2000), no. 12 1677–1679.

[118] K. Y. Tsang, R. E. Mirollo, S. H. Strogatz, and K. Wiesenfeld, *Dynamics of a globally coupled oscillator array*, *Physica D: Nonlinear Phenomena* **48** (1991), no. 1 102–112.

[119] E. U. Rafailov, M. A. Cataluna, and W. Sibbett, *Mode-locked quantum-dot lasers*, *Nature photonics* **1** (2007), no. 7 395–401.

[120] M. G. Thompson, A. R. Rae, M. Xia, R. V. Penty, and I. H. White, *Ingaas quantum-dot mode-locked laser diodes*, *IEEE Journal of Selected Topics in Quantum Electronics* **15** (2009), no. 3 661–672.

[121] T. Akiyama, M. Ekawa, M. Sugawara, H. Sudo, K. Kawaguchi, A. Kuramata, H. Ebe, K. Morito, H. Imai, and Y. Arakawa, *An ultrawide-band (120 nm) semiconductor optical amplifier having an extremely-high penalty-free output power of 23 dbm realized with quantum-dot active layers*, in *Optical Fiber Communication Conference*, p. PD12, Optica Publishing Group, 2004.

[122] J. R. Marciante and G. P. Agrawal, *Nonlinear mechanisms of filamentation in broad-area semiconductor lasers*, *IEEE Journal of Quantum Electronics* **32** (1996), no. 4 590–596.

[123] N. Opačak and B. Schwarz, *Theory of frequency-modulated combs in lasers with spatial hole burning, dispersion, and kerr nonlinearity*, *Physical review letters* **123** (2019), no. 24 243902.

[124] M. Beiser, N. Opačak, J. Hillbrand, G. Strasser, and B. Schwarz, *Engineering the spectral bandwidth of quantum cascade laser frequency combs*, *Optics Letters* **46** (2021), no. 14 3416–3419.

[125] M. Gioannini, P. Bardella, and I. Montrosset, *Time-domain traveling-wave analysis of the multimode dynamics of quantum dot fabry–perot lasers*, *IEEE journal of selected topics in quantum electronics* **21** (2015), no. 6 698–708.

[126] M. Dong, N. M. Mangan, J. N. Kutz, S. T. Cundiff, and H. G. Winful, *Traveling wave model for frequency comb generation in single-section quantum well diode lasers*, *IEEE Journal of Quantum Electronics* **53** (2017), no. 6 1–11.

[127] S. Fujii and T. Tanabe, *Dispersion engineering and measurement of whispering gallery mode microresonator for kerr frequency comb generation*, *Nanophotonics* **9** (2020), no. 5 1087–1104.

[128] M. Osinski and J. Buus, *Linewidth broadening factor in semiconductor lasers–an overview*, *IEEE Journal of Quantum Electronics* **23** (1987), no. 1 9–29.

[129] A. Gordon, C. Y. Wang, L. Diehl, F. X. Kärtner, A. Belyanin, D. Bour, S. Corzine, G. Höfler, H. Liu, H. Schneider, *et. al.*, *Multimode regimes in quantum cascade lasers: From coherent instabilities to spatial hole burning*, *Physical Review A* **77** (2008), no. 5 053804.

[130] J. Duan, H. Huang, D. Jung, Z. Zhang, J. Norman, J. Bowers, and F. Grillot, *Semiconductor quantum dot lasers epitaxially grown on silicon with low linewidth enhancement factor*, *Applied Physics Letters* **112** (2018), no. 25.

[131] J. Duan, H. Huang, B. Dong, D. Jung, J. C. Norman, J. E. Bowers, and F. Grillot, *1.3-μ m reflection insensitive inas/gaas quantum dot lasers directly grown on silicon*, *IEEE Photonics Technology Letters* **31** (2019), no. 5 345–348.

[132] D. Huang, S. Yerkes, G.-L. Su, K. Mehta, M. Cramer, W. O'Brien, R. Dehghannasiri, S. Dobek, C. Mackos, T. Ward, *et. al.*, *Feedback tolerant quantum dot lasers integrated with 300mm silicon photonics*, in *2024 Optical Fiber Communications Conference and Exhibition (OFC)*, pp. 1–3, IEEE, 2024.

[133] B. Dong, H. Huang, J. Duan, G. Kurczveil, D. Liang, R. G. Beausoleil, and F. Grillot, *Frequency comb dynamics of a 1.3 μm hybrid-silicon quantum dot semiconductor laser with optical injection*, *Optics letters* **44** (2019), no. 23 5755–5758.

[134] B. Dong, X. C. de Labriolle, S. Liu, M. Dumont, H. Huang, J. Duan, J. C. Norman, J. E. Bowers, and F. Grillot, *1.3-μm passively mode-locked quantum dot lasers epitaxially grown on silicon: gain properties and optical feedback stabilization*, *Journal of Physics: Photonics* **2** (2020), no. 4 045006.

[135] I. Henning and J. Collins, *Measurements of the semiconductor laser linewidth broadening factor*, *Electronics Letters* **22** (1983), no. 19 927–929.

[136] N. Opačak, F. Pilat, D. Kazakov, S. Dal Cin, G. Ramer, B. Lendl, F. Capasso, and B. Schwarz, *Spectrally resolved linewidth enhancement factor of a semiconductor frequency comb*, *Optica* **8** (2021), no. 9 1227–1230.

[137] D. G. Deppe, H. Huang, and O. B. Shchekin, *Modulation characteristics of quantum-dot lasers: The influence of p-type doping and the electronic density of states on obtaining high speed*, *IEEE Journal of Quantum Electronics* **38** (2002), no. 12 1587–1593.

[138] P. M. Smowton, I. C. Sandall, H. Liu, and M. Hopkinson, *Gain in p-doped quantum dot lasers*, *Journal of applied physics* **101** (2007), no. 1.

[139] Z. Zhang, D. Jung, J. C. Norman, P. Patel, W. W. Chow, and J. E. Bowers, *Effects of modulation p doping in inas quantum dot lasers on silicon*, *Applied Physics Letters* **113** (2018), no. 6.

[140] B. Maglio, L. Jarvis, M. Tang, H. Liu, and P. M. Smowton, *Modelling the effects of p-modulation doping in inas/ingaas quantum dot devices*, *Optical and Quantum Electronics* **56** (2024), no. 4 687.

[141] J. C. Norman, Z. Zhang, D. Jung, C. Shang, M. Kennedy, M. Dumont, R. W. Herrick, A. C. Gossard, and J. E. Bowers, *The importance of p-doping for quantum dot laser on silicon performance*, *IEEE Journal of Quantum Electronics* **55** (2019), no. 6 1–11.

[142] O. Shchekin, J. Ahn, and D. Deppe, *High temperature performance of self-organised quantum dot laser with stacked p-doped active region*, *Electronics Letters* **38** (2002), no. 14 712–713.

[143] O. Shchekin and D. Deppe, *Low-threshold high-t_0 1.3-μm inas quantum-dot lasers due to p-type modulation doping of the active region*, *IEEE Photonics Technology Letters* **14** (2002), no. 9 1231–1233.

[144] R. R. Alexander, D. T. Childs, H. Agarwal, K. M. Groom, H.-Y. Liu, M. Hopkinson, R. A. Hogg, M. Ishida, T. Yamamoto, M. Sugawara, *et. al.*, *Systematic study of the effects of modulation p-doping on 1.3-μm quantum-dot lasers*, *IEEE Journal of Quantum Electronics* **43** (2007), no. 12 1129–1139.

[145] T. Kageyama, K. Nishi, M. Yamaguchi, R. Mochida, Y. Maeda, K. Takemasa, Y. Tanaka, T. Yamamoto, M. Sugawara, and Y. Arakawa, *Extremely high temperature (220 c) continuous-wave operation of 1300-nm-range quantum-dot lasers*, in *The European Conference on Lasers and Electro-Optics*, p. PDA_1, Optica Publishing Group, 2011.

[146] P. M. Smowton, I. C. Sandall, D. J. Mowbray, H. Y. Liu, and M. Hopkinson, *Temperature-dependent gain and threshold in p-doped quantum dot lasers*, *IEEE Journal of Selected Topics in Quantum Electronics* **13** (2007), no. 5 1261–1266.

[147] J. C. Norman, D. Jung, Z. Zhang, Y. Wan, S. Liu, C. Shang, R. W. Herrick, W. W. Chow, A. C. Gossard, and J. E. Bowers, *A review of high-performance quantum dot lasers on silicon*, *IEEE Journal of Quantum Electronics* **55** (2019), no. 2 1–11.

[148] S. Fathpour, Z. Mi, P. Bhattacharya, A. Kovsh, S. Mikhrin, I. Krestnikov, A. Kozhukhov, and N. Ledentsov, *The role of auger recombination in the temperature-dependent output characteristics ($t=\infty$) of p-doped 1.3 μm quantum dot lasers*, *Applied Physics Letters* **85** (2004), no. 22 5164–5166.

[149] J. Kim and S. L. Chuang, *Theoretical and experimental study of optical gain, refractive index change, and linewidth enhancement factor of p-doped quantum-dot lasers*, *IEEE journal of quantum electronics* **42** (2006), no. 9 942–952.

[150] V. Korenev, A. Savelyev, M. Maximov, F. Zubov, Y. M. Shernyakov, M. Kulagina, and A. Zhukov, *Effect of modulation p-doping level on multi-state lasing in inas/ingaas quantum dot lasers having different external loss*, *Applied Physics Letters* **111** (2017), no. 13.

[151] M. Saldutti, A. Tibaldi, F. Cappelluti, and M. Gioannini, *Impact of carrier transport on the performance of qd lasers on silicon: a drift-diffusion approach*, *Photonics Research* **8** (2020), no. 8 1388–1397.

[152] M. T. Crowley, N. A. Naderi, H. Su, F. Grillot, and L. F. Lester, *Gaas-based quantum dot lasers*, in *Semiconductors and Semimetals*, vol. 86, pp. 371–417. Elsevier, 2012.

[153] T. Amano, S. Aoki, T. Sugaya, K. Komori, and Y. Okada, *Laser characteristics of 1.3-μm quantum dots laser with high-density quantum dots*, *IEEE Journal of Selected Topics in Quantum Electronics* **13** (2007), no. 5 1273–1278.

[154] S. Liu, J. C. Norman, D. Jung, M. Kennedy, A. C. Gossard, and J. E. Bowers, *Monolithic 9 ghz passively mode locked quantum dot lasers directly grown on on-axis (001) si*, *Applied Physics Letters* **113** (2018), no. 4.